QUANTUM LIQUID DROPLETS IN A MIXTURE OF BOSE-EINSTEIN CONDENSATES

by

CESAR RAYMUNDO CABRERA CÓRDOVA

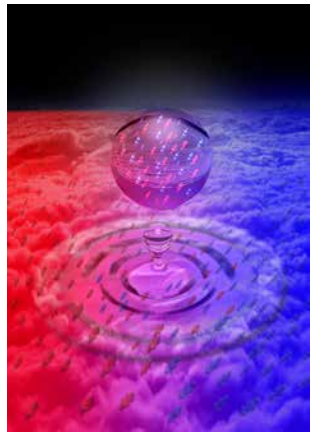

Ph.D. Thesis

Thesis supervisor: Prof. Dr. Leticia Tarruell

ICFO – The Institute of Photonic Sciences
Universidad Politécnica de Cataluña (UPC)

2018

UNIVERSITAT POLITÈCNICA DE CATALUNYA BARCELONATECH

ICFO Institut de Ciències Fotòniques

BIST Barcelona Institute of Science and Technology

Thesis jury
Prof. Dr. Robert Smith
Prof. Dr. Dmitry Petrov
Prof. Dr. Maciej Lewenstein

La familia lo es todo.

Dedicada a mis padres

ABSTRACT

In this thesis, we report on the design and construction of a quantum simulator experiment using quantum gases in Spain. This experiment exploits mixtures of the three isotopes of potassium, which give access in an original approach to the study of Bose-Bose or Bose-Fermi mixtures using the same experimental setup.

We validate our experimental setup with the observation of a Bose-Einstein condensate (BEC) of ^{41}K and ^{39}K. Moreover we observe the dual Bose-Einstein condensation of ^{39}K–^{41}K. These results represents the first observation of BECs in Spain and give access to a novel quantum degenerate mixture in the field. Since the control of interactions in our experiment are crucial, we characterize the scattering properties of the ^{39}K–^{41}K mixture, and spin mixtures of ^{39}K and ^{41}K.

In addition, using a spin mixture of ^{39}K BEC, we report on the observation of a novel state of matter: a composite quantum liquid droplet. This dilute quantum droplet is a liquid-like cluster of ultra-cold atoms self-trapped by attractive mean-field forces and stabilized against collapse by repulsive beyond mean-field many-body effects. This system follows the original proposal of D. Petrov, who predicted the formation of self-bound liquid droplets in mixtures of Bose-Einstein condensates.

In the first series of experiments, we have observed the formation of quantum droplets in a regime where the Bose-Bose mixture should collapse from the mean-field perspective. We directly measure the droplet size and ultra-low density via high-resolution *in situ* imaging, and experimentally confirm their self-bound nature. We demonstrate that the existence of these droplets is a striking manifestation of quantum fluctuations. These droplets do not exist in

single-component condensates characterized by short-range contact interactions. Finally, we observe that for small atom numbers, quantum pressure dissociates the droplets and drives a liquid-to-gas transition, which we map out as a function of interaction strength.

These measurements open an intriguing line of investigation: the difference existing between droplets and bright solitons. In the second series of experiments, we address it by placing the mixture in an optical waveguide, realizing a system that contains both composite bright solitons and quantum liquid droplets. In analogy to non-linear optics, the former can be seen as one-dimensional matter-wave solitons stabilized by dispersion, whereas the latter corresponds to high-dimensional solitons stabilized by a higher order non-linearity. We find that depending on atom number, interaction strength and confinement, solitons and droplets can be smoothly connected or remain distinct states coexisting only in a bi-stable region. We measure their spin composition, extract their density for a broad range of parameters, and map out the boundary of the region separating solitons from droplets.

Our experiments demonstrate a novel type of ultra-dilute quantum liquid, stabilized by contact interactions. They provide an ideal platform for benchmarking complex quantum many-body theories beyond the mean-field approximation in a quantum simulation approach. Furthermore, they constitute a novel playground to explore experimentally self-bound states stabilized by unconventional higher order non-linearities, similar to those relevant in non-linear optics.

RESUMEN

En este trabajo de tesis se reporta el diseño y la construcción de uno de los experimentos pioneros en España que permite realizar simulaciones cuánticas usando átomos ultra fríos. En este experimento se enfrían hasta alcanzar la degeneración cuántica los tres diferentes isotopos de potasio los cuales permiten, de manera particular y original, el estudio de mezclas cuánticas degeneradas de tipo Bose-Bose o Bose-Fermi.

El funcionamiento del experimento es validado por medio de la producción de condensados de Bose-Einstein de ^{41}K y ^{39}K. Además, se reporta la condensación de la mezcla degenerada ^{41}K - ^{39}K, la cual no había sido previamente reportada en la literatura. Estos resultados son los primeros de su tipo en España y por lo tanto abren un amplio panorama en el estudio de fenómenos cuánticos en el país. La mezcla cuántica reportada en esta tesis permite acceder a sistemas cuánticos novedosos en el campo de átomos fríos. El control de las interacciones atómicas es una herramienta ampliamente usada en el campo, por lo cual se han caracterizado las propiedades de dispersión en esta nueva mezcla, así como en diferentes mezclas de espín entre los isotopos ^{41}K y ^{39}K.

El resultado más importante de esta tesis reside en la creación de un nuevo estado de la materia: una gota liquida cuántica ultra-diluida. Esta gota cuántica se compone de una mezcla de dos estados diferentes de espín de ^{39}K. Este líquido se encuentra ligado por sí mismo debido a la compensación de las fuerzas atractivas de campo con el carácter repulsivo de efectos cuánticos que van más allá de la aproximación de campo medio. Este sistema sigue la idea original de D. Petrov, esta propone la formación de líquidos cuánticos usando mezclas de condensados de Bose-Einstein.

En la primera serie de experimentos, hemos observado la formación de gotas cuánticas en un régimen donde una mezcla de Bose debería de colapsar de acuerdo con teorías de campo medio. Se ha medido su tamaño y ultra-baja densidad por medio de imágenes in situ. De esta manera confirma cómo este líquido permanece ligado por si mismo en la ausencia de confinamiento externo. Hemos demostrado que la existencia de estas gotas cuánticas se debe a una manifestación sorprendente de las fluctuaciones cuánticas. Finalmente hemos observado cómo debido a la presencia de la presión cuántica, debajo de un numero critico de átomos el sistema se disocia en gas dando lugar a una transición cuántica liquido-gas. Esta transición se ha medido experimentalmente como función de las interacciones atómicas entre los átomos.

Estas mediciones traen consigo una pregunta intrigante: ¿Cuál es la diferencia entre nuestras gotas cuánticas y los ya conocidos solitones de materia? En una segunda serie de experimentos, hemos dado respuesta a esta interrogante al estudiar las propiedades de una mezcla de Bose confinada en una guía óptica. En este tipo de geometría ambos estados pueden existir. En analogía a sistemas ópticos no-lineales, solitones son sistemas estabilizados por efectos de dispersión, mientras las gotas cuánticas corresponden a solitones de más alta dimensión estabilizadas por efectos no lineales de alto orden. Hemos encontrado que, dependiendo del número de átomos, fuerza de interacción y confinamiento, solitones y gotas cuánticas son dos estados cuánticos que pueden estar conectados, permanecer como dos estados distintos, o coexistir en una región de bi-estabilidad. Se ha medido su composición de espín, densidad del sistema y encontrado experimentalmente la frontera que separa ambos sistemas.

En conclusión, los experimentos mostrados en esta tesis demuestran la existencia de un nuevo liquido cuántico ultra-diluido estabilizado únicamente por interacciones de contacto. Su existencia es puramente debida a las fluctuaciones cuánticas presentes en el sistema. Este sistema provee una plataforma ideal para el estudio y la comprensión de

teorías cuánticas más complejas las cuales van más allá de la aproximación de campo medio.

PUBLICATIONS

- C. R. Cabrera, L. Tanzi, J. Sanz, B. Naylor, P. Thomas, P. Cheiney, and L. Tarruell. Quantum liquid droplets in a mixture of Bose-Einstein condensates. Science **359**, 301 (2018).
- P. Cheiney, C. R. Cabrera, J. Sanz, B. Naylor, L. Tanzi, and L. Tarruell. Bright soliton to quantum droplet transition in a mixture of Bose-Einstein condensates.Phys. Rev.Lett. **120**, 135301 (2018).
- L. Tanzi, C. R. Cabrera, P. Cheiney, J. Sanz, M. Tomza, and L. Tarruell. Feshbach spectroscopy of potassium Bose-Bose mixtures. *In preparation.*
- C. R. Cabrera, L. Tanzi, J. Sanz, P. Cheiney, and L. Tarruell. Dual Bose-Einstein condensation of ^{39}K–^{41}K. *In preparation.*

I have no special talents. I am only passionately curious.

— A. Einstein (attributed).

Not everything that can be counted counts
and not everything that counts can be counted.

— A. Einstein (attributed).

ACKNOWLEDGMENTS

De las tantas formas que existen para empezar una tesis he elegido la "vieja confiable", recordando como hace años, para ser exactos 1735 días, empecé mi locura en esta ciudad conocida como Barcelona: Comencé subiendo a un taxi pidiendo ir a la calle Lluca… la cual después el taxista me contestaría diciendo que esa calle no existía… tal vez la calle Lluça… así es, la famosa Ç trancada ya estaba causando problemas en mi primer día en Cataluña.

No todo lo que empieza mal termina mal, y ese es el caso de mi doctorado, en todo este tiempo he vivido tantas cosas que jamás pensé pasar, para bien o para mal estas me formaron a lo largo de estos años, para que, en este momento frente a ustedes pueda concluir esta tesis con éxito. Los que me conocen saben que he tenido mis altas y bajas, los que me conocen a medias me recuerdan con una sonrisa y una Xibeca en mano, los que no me conocen me ven como el que se la vivía trabajando en el laboratorio 2 del ICFO. Sin embargo, a cada una de esas personas estoy totalmente agradecido ya que tomaron parte un papel muy importante durante esta historia que ahora acaba. Sin el afán de ponerme sentimental, y tampoco esperando que me tachen de romántico al beber de mi caguama y cerrar los ojos mientras me inspiro en estas líneas, me gustaría empezar esta lista de tan valiosa gente.

En la parte profesional no me queda más que agradecerle infinitamente a mi supervisora, colega y amiga de trabajo Dra. Leticia Tarruell. Ella sin conocerme mucho se arriesgó a darme la oportunidad de empezar un doctorado en un laboratorio vacío. Así es, me contrato cuando a mi punto de vista mi mayor carta de presentación era solamente un "mexicano con muchas ganas de trabajar". Ella vió algo que mucha gente no había visto, y que ni yo había visto: me dio la oportunidad de explotar plenamente mis habilidades experimentales. Los primeros años de mi doctorado se dedicó día con día a enseñarme con toda la paciencia cada uno de los trucos necesarios para hacer funcionar estos experimentos en átomos ultra-fríos. Hasta la fecha me ha apoyado de distintas maneras para que pueda seguir con mi vocación de investigación. Mi mejor elección del doctorado sin duda alguna fue trabajar con ella. Leticia, eres una supervisora genial y totalmente entregada a tu trabajo. Simplemente estaré siempre infinitamente agradecido por darme la oportunidad de construir tu primer laboratorio en ICFO. En este aspecto también quisiera agradecer explícitamente a los dos Post-docs con los cuales construí el experimento: Pierrick Cheiney y Luca Tanzi. P. Cheiney es una de las personas más inteligentes con los cuales he trabajado, sin duda alguna él fue fundamental en que esta tesis fuera un éxito. El para mi es el prospecto de post-doc que me gustaría ser en los próximos años. De L. Tanzi (el doctore) aprendí que en esta vida se tiene que ser listo dentro del lab, pero también fuera de él. Tardes llenas de discusiones sin o con mucho sentido pero que permitían en un ambiente totalmente relajado hablar de física. Como olvidar aquella noche en la Sureña, después de unos tragos y unas lágrimas de pollo tuvimos la idea de lo que sería el segundo paper del grupo (un PRL).

En esta lista profesional incluyo una larga lista de personas con las cuales he convivido en el laboratorio por corta o larga duración. Cada uno de ellos ha sido una pieza fundamental en la construcción del experimento y estoy en deuda con ellos: Vincent Lienhard, Manel

Bosch, Lisa Saemisch, Jordi Sastre, Vincent Brunaud, Iñigo Urtiaga, Alberto Muñoz de las Heras, Philip Thomas, Manon Ballu, Craig Chisholm, Anika Frölian y Julio Sanz. En particular también con un colega y amigo Bruno Naylor el cual se leyó toda mi tesis y me dio correcciones sin ser su trabajo, simplemente por el gusto de hacer ciencia. Aprovecho estas líneas para agradecer a cada uno de las personas que laboran en ICFO y con los cuales tuve contacto directo e indirecto. El taller de mecánica encabezado con Xavi, una disculpa por la cantidad de trabajo que siempre les dábamos. El taller de electrónica con José Carlos y Alberto, siempre tuvieron tiempo para explicarme cada circuito y enseñarme la forma de correcta de hacer un trabajo profesional. El departamento de compras (Santi y Magda), ustedes son magníficos sin palabras. Departamento de Mantenimiento (Carlos y Luis) un gusto enorme trabajar día a día con ustedes. Cada uno de los estudiantes de doctorado del ICFO, de los cuales aprendí o robé algo de su laboratorio para construir el nuestro. La lista sería larga, pero gracias a la gente que trabaja en ICFO que me facilito la existencia estos últimos años.

Mi vida fuera del lab me enseñó que durante un doctorado gente viene y por desgracia gente se va. Por lo cual para los que están por aquí cerca de mí, el aplauso es para ustedes que toleran el carácter que suelo tener. Primero que nada, esta tesis se la dedico completamente a mi familia. Concluyo ahora un ciclo el cual comenzó un dos de octubre de ya hace muchos años diciéndoles adiós en la central de Querétaro. Mi papá don Ray y mi mamá doña Tere, la verdad sin ellos simplemente no hubiera sido posible conseguir y cumplir cada una de mis metas y sueños. Ellos me han apoyado día a día, han creído en mí y en los momentos más difíciles han estado para darme el empujón que necesitaba para seguir adelante. Cada día los he extrañado, pero sé que ellos desde la distancia me dan su apoyo y la estabilidad de saber que siempre puedo regresar a un hogar. Padres los quiero mucho y este logro es dedicado totalmente a ustedes. De mi padre aprendí que en esta vida

si se quiere conseguir algo se tiene que luchar y trabajar por ello. De mi madre aprendí que la humildad y los buenos valores son la clave para una vida integra. Ustedes simplemente son el por qué estoy en estos momentos aquí.

A los hermanos Pou (Memo y Arturo), que no se acabe la buena onda que tenemos de hermanos. Como siempre les digo: "más que ser mis hermanos son como mis brothers". Perdón por perderme sus mejores momentos, no acompañarlos en sus triunfos y logros. Más importante aún, perdón por no crecer a su lado, espero alguna vez recobrar ese tiempo perdido. A mis dos únicos familiares cerca de BCN, Jovita y Pacheco. Me han tratado como hijo, me han hecho sentir que tengo un hogar, aunque este lejos de casa. Gracias por recordarme lo que es tener el apoyo de la familia por estos rumbos.

A toda la familia Cabrera Córdova que por ambos lados se han mantenido en contacto conmigo, aunque nunca contesto los correos o mensajes. Gracias por no olvidarse de mí. Aquí no pondré nombres para evitar polémica, pero los que lean este párrafo saben claramente quienes son.

Amigos en BCN, amigos en Alemania, amigos en México. Son los que más cerca he tenido y con los que he vivido esta etapa. En Alemania un saludo para los mimosos (Edgar, Manu, Pepe, Damian y Roberto), quedan muchas estrellas en el universo por conquistar. Roberto, gracias por las veces que me hiciste ver que siempre tomaba las peores decisiones, esperemos que esta mentira no se salga de control. Paulina y Rocío, siempre pendientes que la estuviera pasando bien por aquí y por allá. Ramsés, tu eres medio raro, pero ya sabes que te tengo aprecio. Los primeros dos años de la tesis debido a problemas personales sin duda alguna fueron los más difíciles en mi vida hasta el momento. Estoy en infinita deuda con alguien que, aunque tal vez nunca lea esta tesis, siempre también le estaré agradecido por apoyarme en esos momentos.

Amigos en BCN, la lista sería enorme ya que esta ciudad no permite cultivar tan fácilmente amistades duraderas. A pesar de ello

gracias a cada uno de los integrantes de la "banda dominguera", esa comunidad de mexicanos que me recordaba cada finde lo bonito de nuestra cultura. Dr. Ramon que con agua y paracetamol se curaba todo, gracias por ser mi médico de cabecera en BCN. Ayari y Gaby, puras risas con ustedes minions. "Fantastic five", sin duda alguna una suerte conocerlos, las cosas hubiesen sido muy difíciles sin su ayuda: "Los babes" (Tania y Toño) por darme asilo cada finde que estaba con mis rollos mentales y escuchaban mis historias. Buenas tardes de Netflix con mi manta favorita. Linnete y el Shaky Shaky (la Fira y el Bombon al 100). Josué y aquí incluyo a Albertito, si me voy al MPQ es porque ustedes me convencieron, así que espero que haya valido la pena escucharlos, un abrazo y estoy agradecido por los buenos consejos de amigos y de profesionales que son. A mis dos compas Potosinos: Jairo y Miguel. Jairo pues te toco ser mi compañero de piso cuando escribía la tesis, lo siento cuando me ponía intenso con la tesis, pero pues aguantaste y ya ahora estamos festejando. Miguel, pues mi compañero y amigo de tesis. Me sacaste de un montón de problemas a lo largo del doctorado, compartimos el estrés de la tesis y pues ahora ya acabamos, a disfrutar ya sea aquí o en SLP. Cuando estaba más hundido con la tesis, ahí estabas, gracias man estoy en deuda.

Fuera del grupo de mexicanos, como olvidar a los salseros del RAI. Cada buen baile que hicimos juntos se recuerda con cariño en las salas del mágico DioBar. La Marina y la Bruna "adictos a la fiesta", que esto no termine. Salsa bien bailada, noche jamás olvidada.

Amigos en México, pues aquí la lista se encogió desafortunadamente. Tantos años en Europa cobran factura, pero gracias por lo que aún quedan: Armando (Master integrator), Arturo, Jorge, Elisa, Miguel (el negrin), JoseJo, Elisa, Edgar, Pamela, Vivian, Victor, Pasco y Esteban. Es difícil tener una amistad que dure por años, aunque no compartamos muchas actividades juntos. Les aprecio el tiempo que se han tomado para seguir cultivando esta relación. Concluyo esta lista con un abrazo con mucho afecto para la

Maestra Araceli Nieto, simplemente por ella le encontré un gusto particular a la física y ahora estoy aquí terminado un doctorado. Maestros como usted hacen mucha falta en el país.

Sin duda alguna me falta mucha gente por mencionar, espero que me disculpen por mi mala memoria y dejar todo para el ultimo momento. Concluyo esta tesis diciendo a todos:

Gracias totales.

Finalmente estoy en deuda total con el Consejo Nacional de Ciencia y Tecnología (CONACYT) con CVU: 402242 y a la Secretaría de Educación Pública (SEP) por los apoyos económicos para realizar mis estudios en el extranjero. Sin este apoyo no hubiese posible desarrollarme profesionalmente en Europa.

Gracias México por apostar que la ciencia puede hacer un cambio en nuestra sociedad.

CONTENTS

LIST OF FIGURES

LIST OF TABLES

1 INTRODUCTION

1.1 LIQUIDS BEYOND THE VAN DER WAALS PARADIGM [1]

Gases and **liquids** are ordinary states of matter which are connected to each other as a function of the interaction strength between the atoms. These phases, also called **fluids**, have the same internal symmetry (isotropy and translational invariance), however, the liquid phase appears only when a sensitive balance between attractive and repulsive energy terms takes place.

In the van der Waals picture, two neutral atoms do not interact if they are far apart from each other. However, when they become closer, they attract each other through the so-called van der Waals forces. At even shorter distances, a strong repulsion appears that stems from the Pauli exclusion principle of the electrons. This pair potential in such situations has the generic shape shown in Fig. 1.1 (a). The liquid phase appears when the distance between the atoms is on the order of the van der Waals radius, this is the length scale where the attractive intermolecular interactions compensate the repulsive energy term. This is why, liquids are normally dense and incompressible systems.

Even though it is possible to describe the properties of fluids (liquids or gases) through the well know van der Waals theory (see [2] and references therein), the details of the two-body potential that fully define the properties of the system must be included. Unfortunately, in many cases this potential may be complex or even unknown, which makes the description of "conventional" liquids *non-universal*. Here we refer to universality when in a given limit the system simplifies and can be described with a small set of parameters.

In this thesis we demonstrate that ultra-cold quantum gases can be used to create liquids that differ completely from the van der Waals picture. These liquids are ultra-dilute (with densities eight orders of magnitude lower than water) and can be described in a more general frame. The liquids presented are made of a mixture of two atomic Bose-Einstein condensates. The advantage of ultra-cold atoms is that at ultra-low temperatures and ultra-low densities the interactions in the system can be described in a simple picture using a single parameter: the scattering length.

The stabilization mechanism of our dilute quantum liquid droplets arises from the competition of the attractive mean field energy and repulsive beyond mean-field effects that stem from quantum fluctuations. In this situation, the characteristic length scale is not given any more by the details of the potential but instead by the scattering length parameter. Therefore, this dilute droplet makes possible the study of a liquid state in a *universal* frame. A pictorial representation of the difference between a dense "conventional" liquid and our ultra-dilute liquid is sketched in Fig. 1.1. In this schematic representation, the dense liquid (see Fig. 1.1 (a)) interacts through the two body potential given by the van der Waals theory. The range of the attractive part is represented in light blue, and the range of the repulsion, given by the hardcore part of the potential, is represented in red.

Fig. 1.1 (b) represents our quantum liquid stabilized by quantum fluctuations. In contrast to the van der Waals liquids, the system is so dilute that the atoms do not observe the details of the potential. However, they remain self-bound due to the compensation of attractive mean field forces and the repulsive effect of quantum fluctuations.

In ref. [1], D. Petrov presents more information about these exotic liquids that goes beyond the van der Waals paradigm.

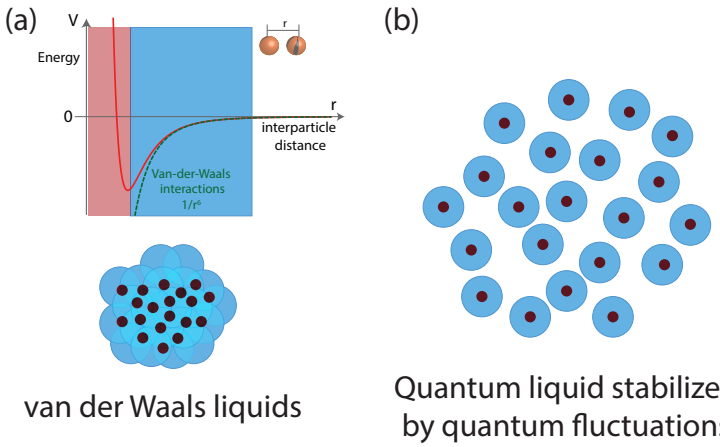

Figure 1.1: Schematic representation of a "conventional" liquid. (a) Particles are bound together at an inter-particle distance where the repulsive core of the potential (red) is compensated by the attraction between particles given by the van der Waals interaction (blue). (b) Ultra-dilute liquid stabilized by quantum fluctuations. The particles are bound at a length scale where the details of the two body potential are negligible. This liquid is a direct consequence of pure quantum mechanical effects. Image inspired by ref. [1].

1.2 OVERVIEW OF THIS THESIS

The place where we have performed all the experiments presented in this thesis is located in the LAB002 at ICFO – The Institute of Photonic Sciences in Barcelona, Spain. In particular, I started my Ph.D. officially in January 2014 and one month later we received our empty lab. From then on we have focused on the design and construction of a new ultracold quantum gas experiment in Spain and recently in the observation of quantum liquid droplets in a mixture of Bose-Einstein condensates. Along the next chapters we will explain the main results obtained during the last years.

In the first part of the thesis, we focus on the production of the first dual BEC of ^{39}K-^{41}K and the characterization of its inter and intraspecies interactions. The second part of the thesis explores some properties of these exotic liquid droplets and the connection with the well-known bright solitons. Each chapter contains an introduction to it to motivate the main ideas. The thesis is organized as follows:

The **first chapter** introduces in a general context the concept of Bose-Einstein condensation in ultracold atoms. We discuss the derivation of the Gross-Pitaevskii equation, the excitation spectrum of a BEC and the modification of the thermodynamic properties of the condensate in the presence of interactions. We extend this formalism to the two-component condensate and discuss as well the properties of the mixture. We discuss the first correction to the mean field energy of a BEC, the so-called Lee-Huang-Yang energy. We introduce this term for both the single and two component case. The existence of quantum droplets is a striking manifestation of this beyond mean-field correction. We show why this contribution can be easily revealed in two-component condensates in comparison to the single component case.

The **second chapter** and **third chapter** go hand in hand. We explain there the design and construction of an ultra-cold quantum gas experiment together with the route to achieve quantum degeneracy. The **second chapter** is devoted to the experimental details of our potassium

machine. We discuss the laser system required to manipulate the three different isotopes of potassium (laser cooling and evaporative cooling in conservative traps), we present in detail the vacuum system employed and we introduce the high numerical aperture objective used to image the atomic cloud. Among other technical details presented in this chapter, we include for completeness the reference of every single device introduced. We are convinced this is useful information for the future generations of people working in the experiment.

The **third chapter** explains how we have set the different experimental tools together to obtain a degenerate quantum gas. Here we introduce the experimental sequence used to condense ^{41}K. We characterize in detail the different cooling stages (laser cooling and evaporative cooling), and we introduce the idea of sympathetic cooling of ^{39}K using ^{41}K as a coolant. This technique turns out to be as efficient as ^{39}K-^{87}Rb experiments but with a faster production cycle. Moreover, we have simplified the experimental setup using the same atom. We finally report on the production of, to the best of our knowledge, the first dual BEC of ^{39}K-^{41}K.

The **fourth chapter** presents a detailed characterization of the interaction between the mixture ^{39}K-^{41}K and some spin mixtures of ^{39}K and ^{41}K. We report on the observation of 20 unobserved resonances in the mixture ^{39}K–^{41}K. We located the resonances using Feshbach loss spectroscopy. In addition, we develop an asymptotic bound-state model (ABM) for potassium mixtures. Finally, we compare our experimental results with our ABM model and coupled-channel calculations based on the model potentials reported in the literature.

The **fifth** and **sixth chapter** are devoted to the study of composite quantum droplets. The **fifth chapter** is split in two: the theory behind quantum droplets and the experimental observation of this self-bound state. In the theory section, we introduce the main ideas behind the stabilization mechanism of the Bose-Bose mixture with effective attractive interactions. We present the theoretical model introduced by D. Petrov [3] which is based on an extended Gross-Pitaevskii equation where

the effect of quantum fluctuations is included as an additional term. We introduce the phase diagram of the system as a function of atom number and interaction strength. Finally, we discuss the liquid-to-gas transition induced by the quantum pressure of the system. We summarize the main properties of the droplet, as discussed by D. Petrov in its original proposal. In addition, we include the state-of-the-art of dipolar droplet experiments and comparisons between dipolar and composite droplets.

In the experimental section, we reveal the effect of beyond mean-field effects by presenting the absence of collapse in a Bose-Bose mixture. The system becomes self-bound for a given atom number and interaction strength. Taking advantage of the three-body recombination present in the system, we reveal the presence of the liquid-to-gas phase transition as a function of atom number. Below a critical atom number, the droplet dissociates into a gas. We map out experimentally for different parameters the phase transition. We conclude this chapter by comparing our results with the ones published recently at LENS.

The **sixth chapter** presents how Bose-Einstein condensates with attractive mean-field interactions allow us to explore in the same setting different self-bound states like bright solitons and quantum droplets. We compare both systems where the former is stabilized due to the interplay with quantum pressure while the latter is due to beyond mean-field effects. In this chapter we show the spin composition of the system and its dependence with interaction strength. We discuss how solitons and droplets are different solutions that appear when an effective change of the dimensionality takes place in the system.

This thesis concludes by explaining our current and future research directions.

2 THEORETICAL FRAME

2.1 INTRODUCTION

In this chapter, we introduce the fundamental concepts and theoretical background on Bose-Einstein condensates (BECs) in ultra-cold alkali atoms. In the first part of this chapter we give a brief introduction about the thermodynamic and dynamic properties of a BEC, the interactions between atoms and the mean-field theory used to describe the system. We describe the elementary excitations of a single component Bose-Einstein condensate and the first beyond mean-field correction to the energy of the gas.

The second part of the chapter is dedicated to the study of the fundamental properties of degenerate Bose-Bose mixtures. Combining two Bose-Einstein condensates increases the complexity of the many-body problem and enriches the physical properties of the ground state phase diagram. We present the condition for the miscible-immiscible scenario where strong repulsive interactions between condensates lead to the phase separation of the system. If the intra-species interactions are instead attractive, the Bose-Bose mixture is predicted to collapse. These two scenarios are expected in the frame of the mean-field formalism.

We then introduce the generalization of the Gross-Pitaevskii equation for a multicomponent BEC. Finally, we present an effective description of a Bose-Bose mixture with beyond mean-field corrections.

2.2 ULTRA-COLD BOSE GASES: FROM THERMAL GASES TO BOSE-EINSTEIN CONDENSATION

2.2.1 *Non-interacting Bose-Einstein condensate*

Bose-Einstein condensation is a pure effect of quantum statistics. It corresponds to the macroscopic population of the ground state of the system in a gas of bosonic atoms. For a homogeneous and non-interacting Bose gas, the occupancy of states in the system follows the Bose-Einstein distribution

$$n_i(\varepsilon_i) = \frac{1}{e^{(\varepsilon_i - \mu)/k_B T} - 1}, \tag{2.1}$$

where k_B is the Boltzmann constant, μ defines the chemical potential, ε_i the energy of the i state and T the temperature of the system. Following the normalization condition with the total atom number $N = \Sigma_i n_i(\varepsilon_i)$, for a given temperature T there is a maximum number of particles N_c that can occupy excited states ($i > 0$). If the total atom number N is superior to N_c, all the "extra" atoms occupy the ground state ($i = 0$) which can become macroscopically populated.

Using the thermal de-Broglie wavelength associated with the particles

$$\lambda_{\text{th}} = \frac{h}{\sqrt{2\pi m k_B T}}, \tag{2.2}$$

with h representing the Planck constant and m the mass of the particles, we can recast the differences between a thermal gas and Bose-Einstein condensation in terms of the phase-space density

$$\text{PSD} = n\lambda_{\text{th}}^3, \tag{2.3}$$

where $n = N/\mathcal{V}$ represents the density for a given particle number N in a volume $\mathcal{V}$. For thermal gases, the PSD is much lower than one, while close to the BEC transition it becomes on the order of unity. The

latter indicates that when the inter-particle distance $\left(d \propto n^{-1/3}\right)$ is on the order of the thermal de-Broglie wavelength, the wave functions associated to each particle will overlap and give rise to a single macroscopic quantum matter wave.

For the homogeneous case, the critical temperature T_c^0 where the system begins to occupy the ground state macroscopically is given by

$$k_B T_c^0 = \frac{2\pi}{\zeta(3/2)^{2/3}} \frac{\hbar^2 n^{2/3}}{m} \approx 3.31 \frac{\hbar^2 n^{2/3}}{m}, \tag{2.4}$$

with $\hbar = h/2\pi$ the reduced Planck constant and $\zeta(s)$ defined as the Riemann zeta function [4]. Here the phase space density is equal to PSD $= \zeta(3/2)$. At fixed atom number N_{total}, the amount of atoms in the condensate N_0 increases by reducing the temperature T below T_c^0. Here the condensed fraction scales as a function of temperature as

$$\frac{N_0}{N_{\text{total}}} = 1 - \left(\frac{T}{T_c^0}\right)^{3/2}. \tag{2.5}$$

Trapped Bose-Einstein condensates

In cold atoms experiments, the atomic cloud is usually confined with a harmonic potential V_{ext}. The presence of this potential modifies the critical temperature and atom number at which the macroscopic occupation of the lowest state energy appears. For a three-dimensional harmonic oscillator potential, the transition temperature is given by [4]

$$k_B T_c^0 = \hbar\overline{\omega} \left(\frac{N}{\zeta(3)}\right)^{1/3} \approx 0.94\, \hbar\overline{\omega} N^{1/3}, \tag{2.6}$$

where $\overline{\omega} = (\omega_x \omega_y \omega_z)^{1/3}$ represents the geometrical mean of the harmonic oscillator trap frequencies. The condensed fraction in this situation is given by

$$\frac{N_0}{N_{\text{total}}} = 1 - \left(\frac{T}{T_c^0}\right)^3 . \tag{2.7}$$

For typical parameters in our experiment, the critical temperatures are in the order of hundreds of nK.

All the expressions presented above are derived by assuming a non-interacting system. In section 2.4, we will see how these properties are modified due to the interactions between the particles and finite size effects.

2.3 ULTRA-COLD INTERACTIONS

2.3.1 *Introduction*

In the experiments, the collisional properties of the atoms are essential. In fact, the re-thermalization of the gas during evaporative cooling is only possible due to the presence of scattering events between the atoms. Moreover, the interactions in the system define the ground state energy and the different properties of the condensate (superfluidity, collective excitations and shape, among others) [5].

The collisional properties of ultra-cold gases have been studied extensively in the literature [4–8]. Therefore, in this section we only review the most important concepts.

2.3.2 *Interactions between pairs of neutral atoms*

The scattering properties in a collision of two neutral atoms with mass m_1 and m_2 depend on the central potential $V(r)$ and the inter-particle distance r. At long distance, the inter-particle forces between atoms

are mainly governed by the instantaneous induced dipole-dipole interactions. This results in an attractive van der Waals force that scales as $-1/r^6$. The characteristic length scale associated is the so-called van der Waals range

$$r_0 = \frac{1}{2}\left(\frac{2m_r C_6}{\hbar^2}\right)^{1/4}, \tag{2.8}$$

with C_6 being the dipole-dipole dispersion coefficient and m_r the reduced mass

$$m_r = \frac{m_1 m_2}{m_1 + m_2}. \tag{2.9}$$

For potassium atoms $r_0 \approx 65\, a_0\, (3.5\,\mathrm{nm})$, where a_0 is the Bohr radius [9].

As the particles approach each other, a short-range repulsion becomes dominant. This is a consequence of the overlap of the wave functions associated to the electrons of the atom pair (Pauli exclusion principle). Taking into account the total electronic spin configuration of the atom pair, the central potential $V(r)$ can be decomposed into singlet $V_s(r)$ and triplet $V_t(r)$ terms:

$$V(r) = V_s(r)P_s + V_t(r)P_t. \tag{2.10}$$

Here P_s and P_t represents the probability of the atom pair to be either on the singlet or triplet spin state. In Fig. 2.1 we sketch an example of the singlet and triplet potentials.

2.3.3 *Ultra-cold collisions*

In ultra-cold scattering theory it is well-known that van der Waals potentials similar to the one shown in Fig. 2.1 can be described and parametrized in terms of a single paramater a so called the *the s-wave* scattering length. This is valid in the low energy limit where the particles have extremely low temperature that they scatter only through

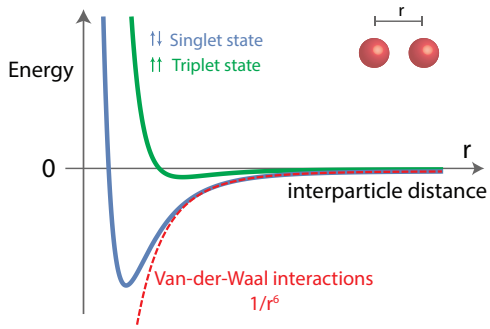

Figure 2.1: Neutral atoms interact through a van der Waals type potential. Here the attractive part of the potential (red dashed line) is due to dipole-dipole interactions and scales as $V_{\mathrm{vdW}}(r) \approx C_6/r^6$. The repulsive part of the potential, is given by Pauli exclusion principle between the electrons (see text). The depth of the potential will be defined by whether the two valence electrons are in the symmetric (singlet) or antisymmetric (triplet) configuration.

the lowest partial wave ($l = 0$). Here, higher partial waves do not contribute to the scattering problem. In this limit the corresponding cross-sections can be written as:

$$\begin{aligned} \sigma_{l=0} &= 8\pi a^2 \quad \text{identical bosons.} \\ \sigma_{l=0} &= 4\pi a^2 \quad \text{non-identical atoms.} \\ \sigma_{l=0} &= 0 \quad \text{identical fermions.} \end{aligned} \tag{2.11}$$

One major implication of Eq. 2.11 is that identical fermions have a vanishing cross-section at low temperatures. This implies that evaporative cooling is not possible and therefore other means to cool down polarized fermions are required. The usual solution is a mixture of two distinguishable fermions [10] or sympathetic cooling with a different atomic species [11].

In addition to the low energy limit, the system is so dilute that the average distance between particles $d = n^{-1/3}$ is larger than the van der Waals range r_0. To give an example, in potassium experiments $r_0 \approx 3.5$ nm while for our typical densities $d \approx 8\,\mu$m . The latter implies that

- It is possible to consider only two-body collisions in the system and neglect higher order ones. The cloud is so dilute that the probability to find more than two particles colliding at the same point is very low.
- The particles on average are not affected by the details of the two-body potential $r_0 \ll d$.

In this situation, it is not required to know the details of the potential, and instead, we can use a simple model potential to describe the same scattering properties of the system. The simplest way to parametrize the scattering of two neutral particles is using contact interactions. This sort of interaction can be represented using a delta function potential

$$V(\mathbf{r}) = g\,\delta(\mathbf{r})\frac{\partial}{\partial r}r; \quad g = \frac{4\pi\hbar^2 a}{m}. \tag{2.12}$$

Here g is known as the coupling constant. We use this potential in further derivations where the interactions of the particles are taken into account.

Finally, we can parametrize the diluteness of the system by comparing the inter-particle distance d and the scattering length a by introducing the concept of *gas parameter* defined as

$$n|a|^3. \tag{2.13}$$

This quantifies as well whether the system is in the weakly ($n|a|^3 \ll 1$) or strongly interacting regime ($n|a|^3 \approx 1$).

2.3.4 *Feshbach resonances*

Due to the internal atomic structure, the collision between two atoms depends on the electronic spin configuration (singlet and triplet) but also on the internal state of the atom pair. Therefore there are several scattering channels similar to the ones presented in Fig. 2.1. The energy difference on each available potential depends on the internal states of the atom pair (hyperfine or Zeeman states). When two of these channels conserve the same total momentum M they can couple to each other and modify the scattering properties of the collision. This effect was studied a long time ago in nuclear physics [12] and then in atomic physics [13] and is known as Feshbach or Fano-Feshbach resonance.

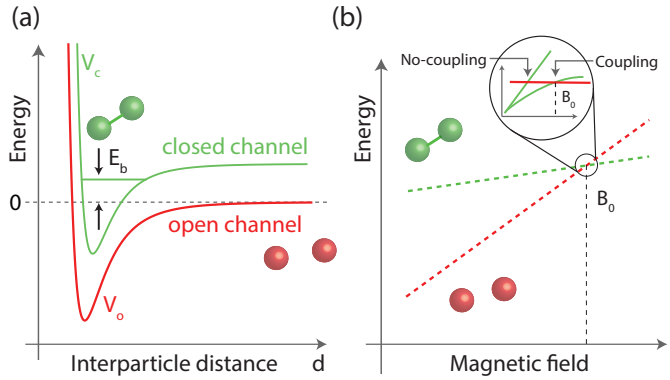

Figure 2.2: (a) Feshbach resonance mechanism. If the energy of any bound state E_b approaches the energy E of the free particle threshold the amplitude of the scattering length a is modified. (b) When the energy becomes degenerate between the molecular bound state and a pair of two free atoms, a resonance takes place. The position of the crossing can be adjusted using magnetic fields because the two states have different magnetic moments.

The main idea behind a Feshbach resonance is the following. Let us consider for simplicity the existence of the two-body potentials presented in Fig. 2.2 (a). These potentials represent the interaction of a

pair of atoms with a distinct internal degree of freedom. One (red potential) we call the *open channel* $V_O(r)$ in which we consider the collision of a pair of free atoms. The other one (green potential) is the *closed channel* which has overall a higher energy, but a bound state with energy E_b similar to the energy of two free atoms.

By tuning the magnetic field, we modify the energy of the free atom pair as sketched with the red dashed line on Fig. 2.2 (b), and also the energy of the bound state in the closed channel. Due to the difference in magnetic moments of the free atom pair and the bound state, for a given magnetic field B_0 the energy of the two states crosses (degenerated energies), and a resonance event occurs. This crossing between two channels gives as a consequence a modification in the scattering length a.

The scattering length close to a Feshbach resonance follows the relation [14]

$$a(B) = a_{bg}\left(1 - \frac{\Delta}{B - B_0}\right), \tag{2.14}$$

where the background scattering length (a_{bg}) denotes the scattering length away from the resonance condition. The width of the resonance is represented with Δ and B_0 the resonant magnetic field.

An example of the tunability of the scattering length as a function of the magnetic field is shown in Fig. 2.3. Such tunability of the *s-wave* interactions, from repulsive to attractive character, is one of the main tools exploited in our experiments.

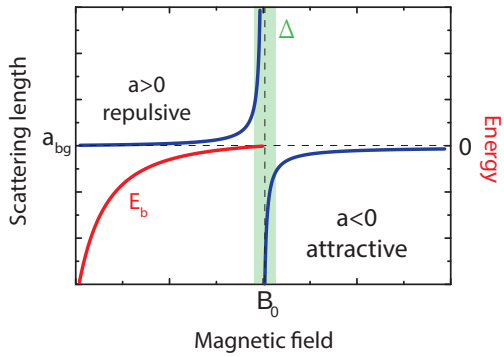

Figure 2.3: Scattering length vs. magnetic field. The scattering amplitude diverges at $B = B_0$. The red line represents the energy of the molecular state. This state exists only for positive values of the scattering length.

Feshbach molecules

At the limit of large and positive scattering length, close to the Feshbach resonance, there is a two-body bound state with energy E_b that can be described in terms of the scattering length a as

$$E_b = -\frac{\hbar^2}{2m_r a^2}. \tag{2.15}$$

This is known as *Feshbach molecule* (see Fig. 2.3 red line). Eq. 2.15 is valid in the *universal regime* where the scattering length a associated to the potential is larger than the range of the two-body potential [5]. For resonances where the range of the potential is important, deviations of this binding energy are observed [15, 16].

These sort of molecules are the key ingredient in experiments in the study of the BEC-BCS crossover [17] in ultra-cold fermion systems or in the formation of ultra-cold polar molecules [18].

2.4 BOSE-EINSTEIN CONDENSATES IN THE PRESENCE OF INTERACTIONS

In this section, we discuss the mean-field description of a single component BEC. We start by introducing the Hamiltonian that describes the many-body problem using the second quantization formalism. Using this formalism we derive the well-known Gross-Pitaevskii equation (GPE).

2.4.1 *The time-dependent Gross-Pitaevskii equation*

Consider N interacting bosons confined with an external potential $V_{\text{ext}}(\mathbf{r})$. In such situation the Hamiltonian of the system reads

$$\hat{H} = \hat{H}_0 + \hat{H}_I, \tag{2.16}$$

$$\hat{H}_0 = \int d\mathbf{r}\, \hat{\Phi}^\dagger(\mathbf{r},t)\left(-\frac{\hbar^2}{2m}\nabla^2 + V_{\text{ext}}(\mathbf{r})\right)\hat{\Phi}(\mathbf{r},t), \tag{2.17}$$

$$\hat{H}_I = \frac{1}{2}\int d\mathbf{r}\, d\mathbf{r}'\, \hat{\Phi}^\dagger(\mathbf{r},t)\hat{\Phi}^\dagger(\mathbf{r}',t)V(\mathbf{r}-\mathbf{r}')\hat{\Phi}(\mathbf{r}',t)\hat{\Phi}(\mathbf{r},t), \tag{2.18}$$

where $\hat{\Phi}^\dagger(\mathbf{r},t)$ and $\hat{\Phi}(\mathbf{r},t)$ are the creation and annihilation bosonic field operators which satisfy the usual commutation relations. The interaction term of the Hamiltonian $\hat{H}_I$ describes the two-body collisions where the term $V(\mathbf{r}-\mathbf{r}')$ is the two-body potential introduced in Eq. 2.12.

The time evolution of $\hat{\Phi}(\mathbf{r},t)$ can be derived in the Heisenberg picture [4]

$$i\hbar\frac{\partial\hat{\Phi}}{\partial t} = \left[\hat{\Phi},\hat{H}\right]. \tag{2.19}$$

By substituting Eq. 2.16 into Eq. 2.19 we obtain as a result the equation of motion of the field operator $\hat{\Phi}(\mathbf{r},t)$.

Bogoliubov decomposition

Let us now introduce the *mean-field approximation* (MF) for dilute bosonic gases formulated by N. Bogoliubov [19]. We decompose the field operator $\hat{\Phi}(\mathbf{r}, t)$ as

$$\hat{\Phi}(\mathbf{r}, t) = \psi(\mathbf{r}, t) + \delta\hat{\psi}(\mathbf{r}, t). \tag{2.20}$$

The first term represents the macroscopic population of a single quantum state (the condensate wave-function) defined as $\psi(\mathbf{r}, t) \equiv \left\langle \hat{\Phi}(\mathbf{r}, t) \right\rangle$ the mean-value of the field operator. The second term $\delta\hat{\psi}(\mathbf{r}, t)$ corresponds to the non-condensed fraction of atoms promoted to higher energy states due to internal interactions of the atoms in the condensate or thermal excitations. At $T = 0$ this contribution is only due to *quantum fluctuations*. The main result of this thesis is the existence of a self-bound liquid droplet in BEC mixtures, based on this beyond mean-field correction. Its main consequences are explained in detail in chapter 6 and chapter 7.

Zero temperature

The mean-field picture allows to simplify the description of the condensate and neglect the contributions of $\delta\hat{\psi}(\mathbf{r}, t)$. This is a very good assumption for weakly interacting systems (quantum fluctuations are negligible) and well below T_c where we can assume that all the atoms are in the lowest state of energy (thermal excitations are not important). By inserting Eq. 2.20 into Eq. 2.19 we obtain the *time-dependent Gross-Pitaevskii equation (GPE)* [4]

$$i\hbar\frac{\partial\psi(\mathbf{r}, t)}{\partial t} = \left(-\frac{\hbar^2}{2m}\nabla^2 + V_{\text{ext}}(\mathbf{r}) + g|\psi(\mathbf{r}, t)|^2\right)\psi(\mathbf{r}, t). \tag{2.21}$$

This equation is similar to a Schrödinger equation but with an additional non-linear term $\left(g|\psi(\mathbf{r},t)|^2\right)$ which accounts for the energy associated with the inter-particle interactions.

In Eq.2.21, it is necessary to ensure that the wave function is normalized, therefore we require that

$$\int d^3\mathbf{r}|\psi(\mathbf{r},t)|^2 = N, \tag{2.22}$$

which as a consequence implies that the density of the system is equal to $n(\mathbf{r},t) = |\psi(\mathbf{r},t)|^2$.

2.4.2 *The time-independent Gross-Pitaevskii equation*

The static properties of the condensate can be studied by substituting $\psi(\mathbf{r},t) = \phi(\mathbf{r})\exp(-i\mu t/\hbar)$ into Eq.2.21:

$$\mu\phi(\mathbf{r}) = \left(-\frac{\hbar^2}{2m}\nabla^2 + V_{\text{ext}}(\mathbf{r}) + g|\phi(\mathbf{r})|^2\right)\phi(\mathbf{r}), \tag{2.23}$$

where here μ represents the chemical potential of the condensate. The stationary solutions of the condensate $\phi(r)$ can be found by minimizing the energy functional $E[\phi] = \int d^3\mathbf{r}\,\mathcal{E}$ which reads

$$\begin{aligned}
E[\phi] &= \int d^3\mathbf{r}\left[\mathcal{E}_{\text{kin}} + \mathcal{E}_{\text{trap}} + \mathcal{E}_{\text{MF}}\right] \\
E[\phi] &= \int d^3\mathbf{r}\left[\frac{\hbar^2}{2m}|\nabla\phi(\mathbf{r})|^2 + V_{\text{ext}}(\mathbf{r})|\phi(\mathbf{r})|^2 + \frac{g}{2}|\phi(\mathbf{r})|^4\right] \\
\mathcal{E}_{\text{kin}} &: \text{quantum pressure.} \\
\mathcal{E}_{\text{trap}} &: \text{trapping potential energy.} \\
\mathcal{E}_{\text{MF}} &: \text{mean-field energy.}
\end{aligned} \tag{2.24}$$

In the next chapters, we will show how by choosing the right trial wave function it is possible to obtain the fundamental properties of the system.

Remarks. The GPE is the main theoretical tool used to describe BECs. This equation can be extended to describe more complex scenarios with additional degrees of freedom (multicomponent BEC, coherent coupling between internal states of the condensate, etc). Nevertheless, this equation is valid if the following criteria are satisfied:

- The system is in the thermodynamic limit ($N \Rightarrow \infty, \mathcal{V} \Rightarrow \infty, N/\mathcal{V} = \text{const}$).
- The system is in the weakly interacting regime ($n|a|^3 \ll 1$) and at low temperatures. Quantum and thermal depletion of the condensate can be neglected.
- The size of the system is much larger than the characteristic length scale given by the scattering length a.

2.4.3 *Bose-Einstein condensate in a harmonic trap*

In typical experiments, the BECs are trapped either in a magnetic trap or in a far-off resonance optical dipole trap. As a first approximation they experience a harmonic potential of the form:

$$V_{\text{ext}} = \frac{1}{2} m(\omega_x x^2 + \omega_y y^2 + \omega_z z^2). \tag{2.25}$$

It is well known that the ground state energy of a non-interacting BEC has a Gaussian form with a width given by the harmonic oscillator length imposed by the trap [4]. For the isotropic confinement case ($\omega_x = \omega_y = \omega_z = \omega_0$) this length scale is given by the harmonic oscillator length $a_{\text{ho}} = (\hbar/m\omega_0)^{1/2}$.

In a weakly interacting BEC, the characteristic size of the condensate wave function increases with respect to an ideal Bose gas, however its

shape remains approximately Gaussian [4]. Therefore we can study some elemental properties of trapped BECs using a Gaussian ansatz. The idea is to employ a trial wave function with free parameters that can be minimized to find an upper bound of the energy of the system. The trial wavefunction we employ is given by

$$\phi(x,y,z) = \frac{\sqrt{N}}{\pi^{3/4}(\sigma_x\sigma_y\sigma_z)^{1/2}}\exp\left(-\frac{x^2}{2\sigma_x^2}-\frac{y^2}{2\sigma_y^2}-\frac{z^2}{2\sigma_z^2}\right). \tag{2.26}$$

Introducing this function in Eq. 2.24 and assuming for simplicity the isotropic confinement case we find the width of the condensate that minimizes the total energy of the system. This yields

$$\begin{aligned}\frac{E(\sigma)}{N\hbar\omega} &= \frac{1}{N\hbar\omega}\left(E_{\text{kin}}+E_{\text{trap}}+E_{\text{MF}}\right)\\ &= \frac{1}{4}\left(\frac{3a_{\text{ho}}^2}{\sigma^2}\right)+\frac{1}{4}\left(\frac{3\sigma^2}{a_{\text{ho}}^2}\right)+\frac{1}{\sqrt{2\pi}}\frac{Na_{\text{ho}}^3}{\sigma^3}\left(\frac{a}{a_{\text{ho}}}\right),\end{aligned} \tag{2.27}$$

where E_{kin}, E_{trap} and E_{MF} represents the kinetic, trapping and potential energy respectively. Here $\sigma = \sigma_x = \sigma_y = \sigma_z$. In the non-interacting case ($a = 0$) the mean-field energy does not contribute and the minimum of Eq. 2.27 is obtained as expected when $\sigma = a_{\text{ho}}$.

We can associate to Eq. 2.27 the dimensionless parameter

$$\zeta = \frac{N|a|}{a_{\text{ho}}}, \tag{2.28}$$

which defines when the trapping and kinetic term are of the same order of magnitude compared to the interaction term. Here there are two important limits: on one side for $\zeta \ll 1$, we can neglect the interaction term in the condensate while on the other side for $\zeta \gg 1$ the ground state of the system is dominated by the interactions. This last regime is known as the Thomas-Fermi limit [4].

The result obtained from the minimization of Eq. 2.27 depends strongly on the interaction character of the scattering length. For positive scattering length ($a > 0$) the width σ of the condensate scales with atom number as $N^{1/5}$. For attractive case ($a < 0$), a stable solution does not exist unless certain requirements are fulfilled. In this thesis we study in detail the regime where the system is dominated by attractive interactions, therefore we will particularly focus on this aspect in the following section.

2.4.3.1 *Bose-Einstein condensate with attractive interactions*

A homogeneous BEC in the presence of attractive interactions is an unstable system that collapses due to its negative compressibility [4]. However, in the presence of a trap, the collapse point can be circumvented if the number of atoms in the condensate is low. In an intuitive picture this is due to compensation of the attractive interacting term E_{MF} with the quantum pressure (kinetic energy term E_{kin}) that results from the position-momentum uncertainty of the atoms given by the presence of the trap [20].

Solving Eq. 2.27 for the isotropic harmonic confinement case, we observe in Fig. 2.4 the local minimum of the total energy as a function of the condensate width σ for different values of interaction strength and atom number. Each plot represents a different parameter $\zeta = \frac{N|a|}{a_{\mathrm{ho}}}$. For a critical value of $\zeta = \zeta_c$, the local minimum disappears. This indicates that there is a maximum value of N beyond which the energy terms cannot compensate each other. This critical atom number N_c is given by

$$N_c = \zeta_c \frac{a_{\mathrm{ho}}}{|a|}. \tag{2.29}$$

Here ζ_c is a coefficient that can be found numerically. This value could change depending of the hypothesis made about the shape of wavefunction . For the isotropic case, where a variational Gaussian ansatz technique is used, $\zeta_c = 0.671$. Numerical calculations of the

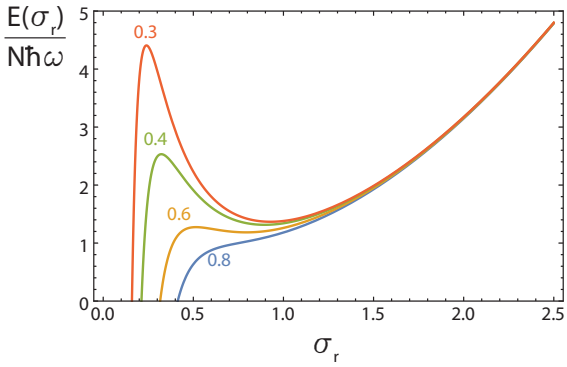

Figure 2.4: Energy of a Bose gas with attractive interactions determined with a variational Gaussian ansatz. Each curve represents a different value of ζ. For a critical value ζ_c the minimum in energy dissapears and the system collapses.

complete GPE give as a result ~ 0.575 [21]. This last value is closer to what it has been reported in the literature experimentally [22, 23]. Thus, the variational technique overestimates the critical atom number N_c.

2.4.4 *The bright soliton solution*

Constraining spatially the condensate allows us to explore dimensional crossovers or physics of Bose gases in lower dimensions. The effective change in dimensionality of a Bose gas is obtained when the mean-field energy is below the energy level spacing provided by the harmonic trap. In the experiments, the presence of a strong external confinement limits the excitations of the condensate along the trapping direction.

In particular, the Gross-Pitaevskii equation presented in Eq. 2.23 has a self-bound solution in **one dimension** for attractive interactions ($g < 0$). This is called *bright* soliton [24, 25]. Solitons are non-linear wavepackets that can propagate without dispersion. Bright solitons in this context are matter-wave analogues of optical solitons.

The condensate wavefunction that describes a 1D-soliton is given by [4]

$$\psi(z,t) = \left(\frac{2\mu}{g}\right)^{1/2} \frac{1}{\cosh[(2m|\mu|/\hbar^2)^{1/2}z]} \exp(-i\mu t/\hbar). \tag{2.30}$$

We observe the peculiar density profile which differs from Bose-Einstein condensates in a trap.

Bose-Einstein condensates confined in cigar-shaped potentials (optical waveguide) allows to explore situations where bright solitons exist. This has been shown in ^{7}Li [26–28], ^{85}Rb [29–31] and ^{39}K [32]. Here the systems are confined transversally but the condensates are allowed to evolve in either weak or zero longitudinal confinement. The potential in such situation reads

$$V(r) = \frac{1}{2} m\omega_{\perp} r^2, \tag{2.31}$$

where $\omega_{\perp}$ represents the transverse trapping frequency. Here the interaction energy of the condensate is smaller than the energy level spacing provided by the radial trap, so the condensate wavefunction in the radial direction has essentially a Gaussian shape with a size given by the transverse harmonic oscillator length. In fact, one can show that in such situation the condensate wavefunction can be written as the product of the longitudinal $f(z,t)$ and transversal contribution [33]

$$\psi(\mathbf{r},t) = f(z,t) \frac{1}{\pi^{1/2} a_{\perp}} \exp\left(\frac{x^2+y^2}{2a_{\perp}^2}\right). \tag{2.32}$$

The axial wavefunction $f(z,t)$ satisfies the 1D GPE equation with the solitonic solution given by Eq. 2.30 [33]. Throughout this thesis, when we recall to quasi 1D systems, we restrict our discussion to situations where the propagation in one direction is free while the other two are constrained.

Finally one can show, by introducing the proper Gaussian ansatz in Eq. 2.27, that in quasi-1D systems the interaction term scales with $1/\sigma_z$ while the kinetic term goes as $1/\sigma_z^2$. At small values of σ_z the interaction term is not able to overcome the repulsion of quantum pressure, but instead they equilibrate and form a bright soliton.

2.4.5 *Collapse of a condensate with attractive interactions*

At the mean-field level, we have discussed that attractive interactions of the condensate lead to the collapse of the system. Even for quasi 1-D systems, where bright solitons partially overcome the collapse and create this self-bound state, for a critical atom number and interaction strength, the mean-field energy overcomes the repulsive character of the quantum pressure. Solitons also collapse following the same argument given in Eq. 2.29. Here the value of ζ_c changes due to the geometry of the trapping potential.

The collapse of the system is due to the striking increase of density. This density change brings a significant rise of inelastic collisions in the system (mainly two- and three-body) which induce atomic losses.

The collapse of a condensate has been studied extensively in refs. [22, 23, 34–36].

2.4.6 *Thermodynamics of an interacting Bose gas*

Using the GPE equation it is possible to compute some of the thermodynamic properties of the condensate and how they are modified in the presence of interactions and trapping potential [37]. Here we present how interactions modify the critical temperature T_c^0 in order to explain our results in chapter 4.

In a trapped interacting Bose gas, the two main contributions to the shift in the critical temperature with respect to an ideal Bose gas (T_c^0) are given by

$$\delta T_c = \delta T_c^{\text{size}} + \delta T_c^{\text{int}}, \tag{2.33}$$

where the first term is due to finite size corrections and the second one comes from the interactions in the system. In a harmonic trap, the finite size term follows the relation

$$\frac{\delta T_c^{\text{size}}}{T_c^0} = -0.73 \frac{\omega_a}{\overline{\omega}} N^{-1/3}, \tag{2.34}$$

with $\omega_a = (\omega_x + \omega_y + \omega_z)/3$ representing the mean trap frequency and $\overline{\omega}$ the geometrical average.

The second term scales as

$$\frac{\delta T_c^{\text{int}}}{T_c^0} = -1.33 \frac{a}{a_{\text{ho}}} N^{1/6}, \tag{2.35}$$

with $a_{\text{ho}} = (\hbar/m\overline{\omega})^{1/2}$ defined as the characteristics length scale of the harmonic oscillator. In general, the contribution of these two terms is usually negative; therefore the measured critical temperature is always below T_c^0 of the ideal case presented in section 2.2.1.

2.4.7 *Elementary excitations*

Other interesting results extracted from the GPE are the elementary excitations of the condensate. These can be found by the linearisation of Eq. 2.21 around the ground state solution. To this end we have included in our total wave-function $\psi(\mathbf{r})$ a deviation $\delta\phi_0(\mathbf{r})$ in the ground state wave function as following:

$$\psi(\mathbf{r}, \mathbf{t}) = \phi_0(\mathbf{r}, t) + \delta\phi_0(\mathbf{r}, t). \tag{2.36}$$

By introducing Eq. 2.36 onto Eq. 2.21, the elementary excitations will be given by the periodic solutions in time and space of the system. If we restrict to the homogeneous case, the perturbations $\delta\phi_0(\mathbf{r})$ can be described as a set of plane waves of the form $\delta\phi_0(\mathbf{r}) \propto (u_q, v_q)e^{i(\mathbf{q}\cdot\mathbf{r}-\omega t)}$. This set of plane waves are also known as: *Bogoliubov modes*. Here $\mathbf{q}$ is the wavector and ω the frequency of the perturbation. The energy of an excitation in the condensate ϵ_q is given by

$$\epsilon_q = \sqrt{2ng\epsilon_q^0 + (\epsilon_q^0)^2} \tag{2.37}$$

with

$$\epsilon_q^0 = \frac{\hbar^2 q^2}{2m}. \tag{2.38}$$

This dispersion relation was first derived by N. Bogoliubov and is known as the Bogoliubov spectrum. In Fig. 2.5 (a) we show the excitation spectrum of a homogeneous BEC. For small values of $\mathbf{q}$, we observe a linear behavior in resemblance to the propagation of sound in materials. In this phonon-like regime, we could define a velocity c associated with the propagation of the excitations in the condensate. This will be given by

$$c = \sqrt{ng/m}. \tag{2.39}$$

This defines the critical velocity in which the condensate could propagate without dissipation. Below this velocity the system is in the superfluidity regime.

The spectrum remains linear up to the point where the kinetic energy of the excitations is comparable to the interaction energy of the quasi particle ($\frac{\hbar^2 q^2}{2m} \approx 2ng$). The wave vector magnitude q_c where this occurs is

$$q_c = \frac{\sqrt{2mng}}{\hbar}. \tag{2.40}$$

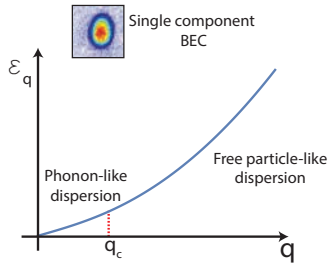

Figure 2.5: Bogoliuvov spectrum for a single component BEC. For low values of q, the quasiparticles follow a phonon-like dispersion while for large q they follow a free particle-like dispersion. The healing length gives the point where the quasi-particles go from acting collectively to behave as free particles in the BEC. This is defined as $\xi = 1/q_c$. The red dashed line represents this characteristic length scale.

This value is the inverse of the healing length of the BEC

$$\xi = 1/q_c. \tag{2.41}$$

If the wavelength of a perturbation is longer than ξ, the quasi-particles act collectively. If it is shorter, then the excitations behave as free particles in the condensate.

Remarks:

- The Bogoliubov approximation is valid in the dilute limit ($na^3 \ll 1$). In fact, when the gas parameter is close to one, it deviates from the spectrum presented in Eq. 2.37, as observed experimentally in [38].
- Here we have restricted this formalism to positive values of the scattering length a. The energy of the Bogoliubov modes is real for the full range of $\mathbf{q}$.

Attractive interactions revisited

In the formalism presented before, we have assumed that the scattering length is positive. Therefore the energy of the excitations is positive. However, we have shown in section 2.3 that we can control the interaction strength *via* Feshbach resonance. For attractive interactions we have shown in section 2.4.3 that a trapped condensate collapses when the repulsive character of quantum pressure is overwhelmed. We can revisit the collapse of the condensate in the frame of Bogoliubov excitations.

A system with attractive interactions implies that the speed of sound defined in Eq. 2.40 becomes imaginary. This leads to an exponential growth of the Bogoliubov modes that make the atoms clump together [4]. For a sufficiently large atom number this mechanical instability leads to the collapse of the system.

As we will see in the next chapters, if this mechanical instability is counterbalanced, it could lead to the formation of self-bound solutions. If the attraction between the atoms is compensated through the repulsive character of the quantum pressure a bright soliton will be formed [39]. If a higher order non-linear term prevents the collapse, it could lead to the formation of quantum droplets [3].

2.5 BEYOND MEAN-FIELD CORRECTION: THE LEE-HUANG-YANG ENERGY

The main result of this thesis is the experimental study of quantum liquid droplets stabilized by quantum fluctuations. In this section, we summarize the most important concepts behind this beyond mean-field (BMF) correction together with state of the art and previous experimental observations.

Up to now we have assumed that all N bosons occupy the same quantum state described by the macroscopic wave function $\phi(r)$ and the system is well described in terms of the Gross-Pitaevskii equation.

As remarked before, the mean-field approximation is valid for dilute systems at low temperatures satisfying the condition $na^3 \ll 1$. However, once the interactions or the temperature of the system increase either quantum or thermal fluctuations become important since they modify the equation of state due to the depletion of the ground state [38].

At zero temperature, the ground state energy density of a homogeneous Bose gas is given by

$$\mathcal{E} = \frac{gn^2}{2}\left(1 + \frac{128}{15\sqrt{\pi}}\sqrt{na^3} + \cdots\right), \tag{2.42}$$

the first term represents the usual mean-field energy while the second term is the first beyond mean-field (BMF) correction to the ground state energy, the so-called Lee-Huang-Yang (LHY) energy derived by Lee T. D., Huang K. and Yang C.N. in the 50´s [40, 41]. Similar to the zero-point motion of particles in the lowest ground state of a quantum mechanical system, the origin of the LHY correction is the zero point motion of the Bogoliubov excitations in the BEC. In that sense, this correction is intrinsically quantum [3].

State of the art

In typical experiments, the gas parameter (na^3) is usually small; therefore the LHY correction in front of the MF term is negligible. Usually large values of the scattering length are required to observe these beyond mean-field contributions.

With the help of Feshbach resonances, the contribution of this LHY term has been revealed experimentally. The first demonstration of this additional term was done by using composite bosons (molecules made of two fermionic atoms). Here, deviations of the equation of state and collective oscillations in the BEC-BCS crossover[1] were observed [17].

1 Here the scattering length needs to be replaced by the dimer-dimer scattering length [42, 43]

In bosonic atomic systems, the zero-temperature equation of state of a homogeneous Bose gas was measured in ref. [44] where it was shown that by increasing the interaction strength, the equation of state departs from the expected mean-field result. Moreover, the correction of the two-body contact parameter C_2 due to the presence of the LHY correction was measured using RF spectroscopy [45]. Finally, using two-photon Bragg spectroscopy the energy of particle-like excitations was measured in a weakly interacting BEC together with the quantum depletion of the condensate [46, 47].

In general, these experiments have explored the properties of strongly correlated Bose gases. A review of this topic can be found in ref. [38] and the references therein.

Recently, the observation of quantum droplets in dipolar gases and Bose-Bose mixtures have revealed the contribution of beyond mean-field terms in weakly interacting systems. This topic is presented in detail in chapter 6.

2.6 ULTRA-COLD BOSE-BOSE MIXTURES

2.6.1 *Introduction*

Multicomponent Bose-Einstein condensates offer the possibility to study different rich phenomena not achievable in single component BECs. This thesis explores the physics of ultra-cold Bose-Bose mixtures, therefore in this section we introduce the notation together with the theoretical formalism used to describe a binary mixture.

2.6.2 *Mean-field Gross-Pitaevskii equation for multicomponent BEC*

Let us assume a ground state Bose-Bose mixture at $T = 0$ composed by two wave functions associated to each component: $(\psi_\uparrow, \psi_\downarrow)$ [48]. We assume that both functions are independent and therefore there is

no phase relation between them. The system can be described by the coupled time-dependent Gross-Pitaevskii equations given by

$$i\hbar\frac{\partial}{\partial t}\psi_\uparrow(\mathbf{r},t) = \left(-\frac{\hbar^2\nabla^2}{2m_\uparrow} + V_\uparrow^{ext}(\mathbf{r}) + g_{\uparrow\uparrow}\left|\psi_\uparrow(\mathbf{r},t)\right|^2 + g_{\uparrow\downarrow}\left|\psi_\downarrow(\mathbf{r},t)\right|^2\right)\psi_\uparrow(\mathbf{r},t)$$

$$i\hbar\frac{\partial}{\partial t}\psi_\downarrow(\mathbf{r},t) = \left(-\frac{\hbar^2\nabla^2}{2m_\downarrow} + V_\downarrow^{ext}(\mathbf{r}) + g_{\downarrow\downarrow}\left|\psi_\downarrow(\mathbf{r},t)\right|^2 + g_{\uparrow\downarrow}\left|\psi_\uparrow(\mathbf{r},t)\right|^2\right)\psi_\downarrow(\mathbf{r},t) \tag{2.43}$$

where the masses (m_j) and trapping potential ($V_j^{\text{ext}}(\mathbf{r})$) are defined for each component using the label indexes $j = (\uparrow,\downarrow)$. The non-linear term here is proportional to the coupling constants $g_{\uparrow\uparrow}$ and $g_{\downarrow\downarrow}$ which describe the *intra-species interaction* of each condensate. Finally the set of equations are coupled through the *inter-species interaction* $g_{\uparrow\downarrow} = 2\pi\hbar^2 a_{\uparrow\downarrow}/m_r$, with m_r representing the reduced mass of the mixture.

Similar to section 2, both wave functions are normalized through the condition.

$$\int d^3\mathbf{r}|\psi_j(\mathbf{r},t)|^2 = N_j \tag{2.44}$$

$$\int d^3\mathbf{r}\left[|\psi_\uparrow(\mathbf{r},t)|^2 + |\psi_\downarrow(\mathbf{r},t)|^2\right] = N_{\text{total}} \tag{2.45}$$

with $N_{\text{total}} = N_\uparrow + N_\downarrow$ representing the total atom number.

The stationary coupled Gross-Pitaevskii equations are:

$$\begin{aligned}
\mu_\uparrow\phi_\uparrow(\mathbf{r}) &= \left(-\frac{\hbar^2\nabla^2}{2m_\uparrow} + V_\uparrow^{\text{ext}}(\mathbf{r}) + g_{\uparrow\uparrow}\left|\phi_\uparrow(\mathbf{r})\right|^2 + g_{\uparrow\downarrow}\left|\phi_\downarrow(\mathbf{r})\right|^2\right)\phi_\uparrow(\mathbf{r}) \\
\mu_\downarrow\phi_\downarrow(\mathbf{r}) &= \left(-\frac{\hbar^2\nabla^2}{2m_\uparrow} + V_\downarrow^{\text{ext}}(\mathbf{r}) + g_{\downarrow\downarrow}\left|\phi_\uparrow(\mathbf{r})\right|^2 + g_{\uparrow\downarrow}\left|\phi_\downarrow(\mathbf{r})\right|^2\right)\phi_\downarrow(\mathbf{r})
\end{aligned} \tag{2.46}$$

The energy functional $E[\phi] = \int d^3\mathbf{r}\,\mathcal{E}$ associated to them is given by

$$\begin{aligned} E[\phi_\uparrow, \phi_\downarrow] = & \int d^3\mathbf{r}\left[\frac{\hbar^2}{2m_\uparrow}|\nabla\phi_\uparrow(\mathbf{r})|^2 + V_\uparrow^{\text{ext}}(\mathbf{r})|\phi_\uparrow(\mathbf{r})|^2 + \frac{1}{2}g_{\uparrow\uparrow}|\phi_\uparrow(\mathbf{r})|^4\right] \\ & + \int d^3\mathbf{r}\left[\frac{\hbar^2}{2m_\downarrow}|\nabla\phi_\downarrow(\mathbf{r})|^2 + V_\downarrow^{\text{ext}}(\mathbf{r})|\phi_\downarrow(\mathbf{r})|^2 + \frac{1}{2}g_{\downarrow\downarrow}|\phi_\downarrow(\mathbf{r})|^4\right] \\ & + \int d^3\mathbf{r}\left[g_{\uparrow\downarrow}\left|\phi_\downarrow(\mathbf{r})\right|^2\left|\phi_\downarrow(\mathbf{r})\right|^2\right]. \end{aligned} \tag{2.47}$$

2.6.3 *Miscible, immiscible and collapse of a Bose-Bose mixture*

Using Eq. 2.47, we can predict the different ground states of a binary mixture. In the repulsive regime ($g_{\uparrow\uparrow}, g_{\downarrow\downarrow}, g_{\uparrow\downarrow} > 0$), one expects a transition between the miscible and the immiscible phase [49]. In such situations, the repulsive inter-species energy between the condensates can be so large that for a given range the system minimizes the energy by spatially separating the two components. This transition has been extensively studied theoretically and experimentally in ref. [50–56].

Another expected result is the collapse of the mixture. In this case, even if each condensate has repulsive intra-species interactions ($g_{\uparrow\uparrow}, g_{\downarrow\downarrow} > 0$), if the inter-species interaction is negative enough, the system cannot overcome the attraction and collapses. Similar collapse of a degenerate Bose-Fermi mixture has been studied in refs. [57–61].

For the homogeneus case the criterion that divides the regimes of miscibility, immiscibility and collapse depends only on the different interaction strengths. This condition is given by [52]

$$|g_{\uparrow\downarrow}| = \sqrt{g_{\uparrow\uparrow}g_{\downarrow\downarrow}}. \tag{2.48}$$

This is shown Fig. 2.6. For $g_{\uparrow\downarrow} > \sqrt{g_{\uparrow\uparrow}g_{\downarrow\downarrow}}$ phase separation occurs, here the phase segregated state has lower total energy (the system is

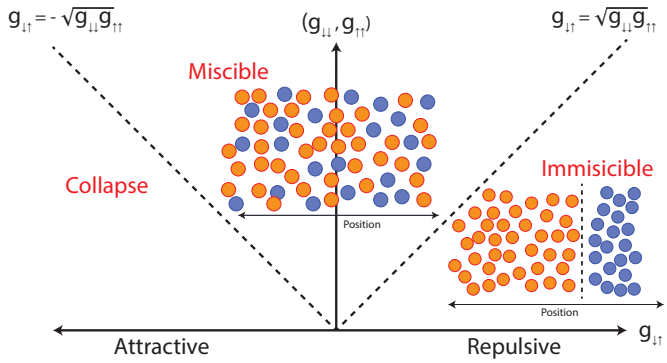

Figure 2.6: Phase diagram of a Bose-Bose mixture. The horizontal axis represents the inter-species scattering length, the vertical axis represents the intra-species interactions on each condensate. Three different regimes are observed: miscibility, immisicbility and collapse. The miscible phase is bounded from the right and the left by the condition $|g_{\uparrow\downarrow}| = \sqrt{g_{\uparrow\uparrow} g_{\downarrow\downarrow}}$.

immiscible). In the intermediate regime $-\sqrt{g_{\uparrow\uparrow} g_{\downarrow\downarrow}} < g_{\uparrow\downarrow} < \sqrt{g_{\uparrow\uparrow} g_{\downarrow\downarrow}}$ the condensates overlap (the system is *miscible*). Finally for $-\sqrt{g_{\uparrow\uparrow} g_{\downarrow\downarrow}} > g_{\uparrow\downarrow}$ the attractive inters-species interactions overwhelms the repulsive ones on each condensate and the system *collapses*.

Here it is useful to introduce the quantity

$$\delta g = g_{\uparrow\downarrow} + \sqrt{g_{\uparrow\uparrow} g_{\downarrow\downarrow}}, \tag{2.49}$$

which is valid close to the collapse regime. This describes the deviations with respect to $g_{\uparrow\downarrow}$. Moreover this quantity is useful to compare the results to the single component BEC. In both cases the unstable regime where the system collapses is when g or δg is lower than zero.

The condition presented in Eq. 2.48 is slighlty modified in the presence of a trapping potential and finite temperature [62, 63].

2.6.4 *Elementary excitations in a two-component BEC*

The calculation of the excitation spectrum in a two-component BEC is more demanding than the single component case. Due to the presence of the two components, there are two different types of excitations: *density* modes and *spin* modes [48]. The *density* modes, similar to the single component case, are density fluctuations of both condensate wave functions (see Eq. 2.36). The *spin* modes instead, are spatial deviations of one component with respect to the other. Following this argument, by comparing the wave function of each condensate, the density modes and spin modes are just in- and out- phase excitations in the system.

Similar to Eq. 2.36, we can write the deviation in the wave functions due to the excitations for each component as

$$\psi_j(\mathbf{r}) = \psi_{0,j}(\mathbf{r}) + \delta_{0,j}\psi(\mathbf{r}). \tag{2.50}$$

Introducing Eq. 2.50 in Eq. 2.6.2, and for simplicity assuming the symmetric case where $g_{\uparrow\uparrow} = g_{\downarrow\downarrow} = \overline{g}$ and $m = m_\uparrow = m_\downarrow$, we obtain the dispersion relation of the system [48, 64]. As expected we obtain two Bogoliubov branches of the form

$$\begin{aligned} \epsilon_q^d &= \sqrt{n(\overline{g} + g_{\uparrow\downarrow})\epsilon_q^0 + (\epsilon_q^0)^2} \\ \epsilon_q^s &= \sqrt{n(\overline{g} - g_{\uparrow\downarrow})\epsilon_q^0 + (\epsilon_q^0)^2}. \end{aligned} \tag{2.51}$$

The indexes d and s refer to density or spin excitations respectively. In Fig. 2.7 both branches are sketched. Similar to the dispersion relation for the single component case (see Fig. 2.5), both branches exhibit a linear regime for small values of $\mathbf{q}$ and free-particle dispersion for larger values. The healing length associated to each Bogoliubov branch is given by

$$\begin{aligned} \xi_d &= \hbar / \left(\sqrt{2} m c_d\right) \\ \xi_s &= \hbar / \left(\sqrt{2} m c_s\right), \end{aligned} \tag{2.52}$$

where c_d and c_s are the sound velocities of the density and spin branches respectively [65]. Approaching the boundaries of the stability condition of Eq. 2.48 (which in the symmetric case reads $|g_{\uparrow\downarrow}| > \overline{g}$), either the density of the spin branch start to soften. In fact, by looking at Eq. 2.51 when crossing the boundary condition the spin ($g_{\uparrow\downarrow} > \overline{g}$) or the density ($g_{\uparrow\downarrow} < -\overline{g}$) branches become imaginary. Both situations are sketched in Fig. 2.7. In the left inset we sketch the $g_{\uparrow\downarrow} > \overline{g}$ regime. For a given value of q the spin branch (green line) becomes imaginary (yellow area). This means when crossing the miscible-immiscible phase transition a mechanical instability occurs and it is given by the spin branch: the system phase separates.

On the right inset of Fig. 2.7, we explore the regime with $g_{\uparrow\downarrow} < -\overline{g}$. In this situation the density branch (blue line) becomes imaginary, and this time the growth of the long wavelength modes make the atoms clump together and collapse.

Remarks

The physics behind the phase separation and the collapse of a Bose-Bose mixture is very similar in the *mean-field picture*. In both situations, one of the modes becomes soft close to the condition of Eq. 2.48. At the transition point, the effective speed of sound defined for each mode is zero and then becomes imaginary. A mechanical instability drives the system to either phase-separation or collapse.

Note. In chapters 6 and 7 we discuss how a Bose-Bose mixture in the

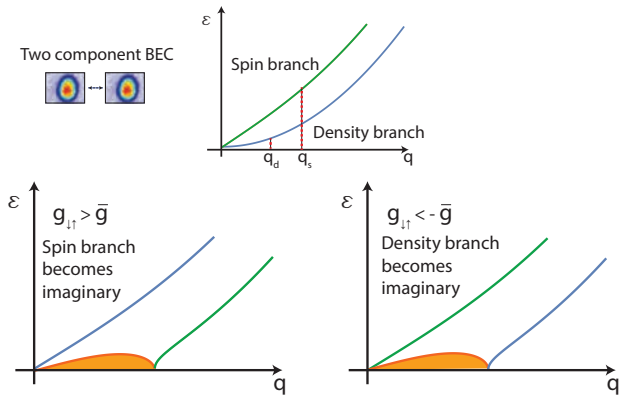

Figure 2.7: The absolute value of the imaginary contribution of the modes is represented in the yellow area. For values $g_{\uparrow\downarrow} > \bar{g}$ the system phase separate (left panel) while for $g_{\uparrow\downarrow} < -\bar{g}$ the mechanical instability leads to the collapse of the Bose-Bose mixture (right panel). In both cases either the spin mode (left panel) or the density mode (right panel) become imaginary at the critical point.

regime $g_{\uparrow\downarrow} < -\bar{g}$ does not collapse, but instead, the mechanical instability given by the density mode is "cured" by quantum fluctuations [3].

2.6.5 *The effective single component GPE*

Up to now we have presented the general description of a Bose-Bose mixture. However, in some regimes, we can describe the properties of the system in a simpler way without using the set of coupled GPE equations. In the miscible phase and close to the collapse point, we can describe the system with an effective low-energy theory: an effective single component Gross-Pitaevskii equation. The idea is to neglect spin excitations (which for this regime are more energetic than density excitations) and treat the mixture as an effective single component

BEC. To fulfill this condition, we assume identical spatial modes for the two components

$$\psi_\uparrow(r) = \sqrt{n_\uparrow}\phi(\mathbf{r}); \quad \psi_\downarrow(r) = \sqrt{n_\downarrow}\phi(\mathbf{r}), \tag{2.53}$$

which implies that the density ratio is locked to the condition

$$n_\uparrow / n_\downarrow = \sqrt{g_{\downarrow\downarrow}/g_{\uparrow\uparrow}} \tag{2.54}$$

in order to minimize the mean-field energy density where the spatial overlap of the two components is maximized.

In the homogeneous case by inserting Eq. 2.53 into Eq. 2.47, the corresponding energy density functional reads

$$\begin{aligned} \mathcal{E} &= \mathcal{E}_{\text{kin}} + \mathcal{E}_{\text{MF}} \\ &= \frac{\hbar^2}{2m} n_0 |\nabla\phi(\mathbf{r})|^2 + \delta g \frac{\sqrt{g_{\downarrow\downarrow}/g_{\uparrow\uparrow}}}{(1+\sqrt{g_{\downarrow\downarrow}/g_{\uparrow\uparrow}})^2} n_0^2 |\phi(\mathbf{r})|^4, \end{aligned} \tag{2.55}$$

where $n_0 = n_\uparrow + n_\downarrow$ and $\mathcal{E}_{\text{kin}}$, $\mathcal{E}_{\text{MF}}$ denote the kinetic and mean-field contributions to the energy density of the mixture respectively. This energy functional results in an extended Gross-Pitaevskii equation given by

$$i\hbar\dot{\phi}(\mathbf{r}) = \left[\left(-\frac{\hbar^2}{2m}\nabla^2\right) + \alpha n_0 |\phi(\mathbf{r})|^2\right]\phi(\mathbf{r}), \tag{2.56}$$

where α is defined as

$$\alpha = \frac{2\sqrt{g_{\downarrow\downarrow}/g_{\uparrow\uparrow}}}{\left(1+\sqrt{g_{\downarrow\downarrow}/g_{\uparrow\uparrow}}\right)^2}\delta g. \tag{2.57}$$

At the mean-field level Eq. 2.56 is equivalent to a single-component Gross-Pitaevskii equation provided one does the replacement

$$\alpha \to g. \tag{2.58}$$

We recall that, at the mean-field level the system becomes unstable for $\delta g = g_{\uparrow\downarrow} + \sqrt{g_{\uparrow\uparrow} g_{\downarrow\downarrow}} < 0$. There the energy of the soft mode (density mode) becomes imaginary and in principle should drive the system to mechanical instability. This effect is equivalent to what happens in the single component BEC case.

2.7 BEYOND MEAN-FIELD CORRECTIONS IN BOSE-BOSE MIXTURES

In section 2.5, we have explained the main features of the LHY correction and how it has been revealed in single component condensates. Recently it has been proposed theoretically and observed experimentally that such correction in two-component Bose-Einstein condensates gives rises to the creation of quantum liquid droplets [3, 66, 67]. Here we introduce the LHY energy for a binary mixture.

2.7.1 *Lee-Huang-Yang energy of a Bose-Bose mixture*

For a three-dimensional homogeneous Bose-Bose mixture, the excitation spectrum consists of two branches which contribute to the quantum fluctuations in the system [68]. Following ref. [3] the energy functional of a Bose-Bose mixture is given by the contribution of the mean-field energy, and the additional repulsive term which includes the effect of quantum fluctuations. This functional reads

$$\begin{aligned}\mathcal{E} &= \mathcal{E}_{\mathrm{MF}} + \mathcal{E}_{\mathrm{LHY}} \\ &= \frac{1}{2}\left(g_{\uparrow\uparrow} n_{\uparrow}^2(\mathbf{r}) + g_{\downarrow\downarrow} n_{\downarrow}^2(\mathbf{r})\right) + g_{\uparrow\downarrow} n_{\uparrow}(\mathbf{r}) n_{\downarrow}(\mathbf{r}) \\ &\quad + \frac{8 m_{\uparrow}^{3/2} g_{\uparrow\uparrow}^{5/2}}{15\pi^2\hbar^3} F\left(\frac{m_{\downarrow}}{m_{\uparrow}}, \frac{g_{\uparrow\downarrow}^2}{g_{\uparrow\uparrow} g_{\downarrow\downarrow}}, \sqrt{\frac{g_{\downarrow\downarrow}}{g_{\uparrow\uparrow}}}\right) \left|\sqrt{n_{\uparrow}(\mathbf{r})}\right|^{5/2} \left|\sqrt{n_{\downarrow}(\mathbf{r})}\right|^{5/2},\end{aligned} \tag{2.59}$$

where for the equal mass case $\overline{m} = m_{\uparrow} = m_{\downarrow}$

$$F(1, x, y) = \sum_{\pm} \left(1 + y \pm \sqrt{(1-y)^2 + 4xy}\right)^{5/2} / 4\sqrt{2}. \tag{2.60}$$

The symmetric case

In order to obtain a deeper insight about the scaling of these contributions, let us examine again the symmetric case where $\overline{g} = g_{\uparrow\uparrow} = g_{\downarrow\downarrow}$. In terms of the δg parameter and $n_0(r)$, we can rewrite Eq. 2.59 as

$$\mathcal{E} = \frac{1}{4} n_0^2(\mathbf{r}) \delta g + \kappa n_0^{5/2}(\mathbf{r}) \overline{g}^{5/2}, \tag{2.61}$$

where $\kappa = \frac{\sqrt{2}\overline{m}^{3/2}}{15\pi^2\hbar^3} F\left(1, \frac{g_{\uparrow\downarrow}^2}{\overline{g}^2}, 1\right)$. Under this form we can clearly appreciate the different scaling of both the MF and BMF term together with its dependence on the interaction strength. The following points are important to remark:

- The LHY term presented in Eq. 2.61 depends only on the contact interaction depicted with the coupling constant $\overline{g}$ while the mean-field depends on δg. This means if we explore the regime close to the collapse point of a Bose-Bose mixture ($\delta g \approx 0$) we can find a situation where the MF energy is small while keeping

the LHY term sizeable. Beyond mean-field effects become significant.

- For $\delta g < 0$, the different density scaling of the LHY $\left(n_0^{5/2}\right)$ and mean-field term $\left(n_0^2\right)$ allows us to find an equilibrium density n_{eq} where the attractive mean-field term $\mathcal{E}_{\mathrm{MF}}$ is compensated by the repulsive LHY energy ($\mathcal{E}_{\mathrm{LHY}}$). This will give rise to a self-bound solution: the so-called quantum liquid droplet.

In conclusion, the presence of quantum fluctuation in a system where the mean-field contribution can be tuned close to zero allows beyond mean-field effects to be revealed. The ground state of the mixture is modified for $\delta g < 0$ and the collapse at the mean-field level can be suppressed. This will be explained in detail in chapter 6.

3 THE POTASSIUM EXPERIMENT AT ICFO

3.1 OVERVIEW

The experimental apparatus described in this chapter is one of the main achievements of my Ph.D. The lab was empty when I started (see Appendix B), therefore I have been involved in the process of designing, building and developing our complete quantum gas experiment. Along this project I have worked together with P. Cheiney, L. Tanzi (post-docs) and J. Sanz (Ph.D. student).

The production of ultra-cold atomic gases uses experimental techniques that are nowadays standard. In particular laser cooling followed by evaporative cooling in conservative traps (magnetic or optical) is the standard path to reach quantum degeneracy [4, 69, 70]. In this chapter, we describe the details of the approach followed in our experimental apparatus to reach quantum degeneracy with potassium.

3.2 DESIGN AND CONSTRUCTION OF AN EXPERIMENTAL APPARATUS

3.2.1 *Choice of the atomic species: why potassium?*

One of the central decisions to make in the design and construction of an ultra-cold quantum gas experiment is the proper selection of the atomic element. The most common atoms employed are alkalis. The reason behind this choice is their simple internal atomic level structure (one valence e^-) that can be described by a hydrogen-like equation [71]. This picture simplifies their manipulation as compared to dipolar atoms or two-electron atoms.

Among the different alkali metals, we have decided to work with **potassium** (**K**). It has three stable natural isotopes (two bosons and one fermion), and degenerate quantum gases of each of them has been achieved [72–74]. Moreover, this atom is well known for the high tunability of its interactions via Feshbach resonances [75–78]: for the three isotopes it is possible to control with high accuracy the scattering length a. In addition, the different possible isotopic mixtures (^{40}K-^{41}K or ^{39}K-^{41}K) show similar tunability (see Ref.[79] and chapter 5).

The control of interactions and the possibility to perform experiments with bosonic or fermionic statistics makes potassium an exciting candidate to study a broad range of phenomena such as Bose (Fermi) gases at unitarity [17, 38], Bose (Fermi) Hubbard models [80, 81], among others. In our case, we chose potassium to study quantum degenerate Bose-Bose or Bose-Fermi mixtures. Compared to quantum mixtures composed of different atoms, here the similar mass of each isotope allows neglecting the gravitational sag between the components of the mixture. Therefore, we could explore different topics such as Bose/Fermi polarons [82, 83] with an extraordinary overlap of the bath with the impurity, unitary Bose-Bose or Bose-Fermi mixtures, miscible-immiscible phase transition, two component quantum liquid droplets (Bose-Bose or Bose-Fermi) to mention a few.

In the next chapters, the relevant properties of potassium will be discussed.

3.2.2 *Potassium properties: summary*

During my thesis, I found highly useful the Appendix A of the Ph.D. thesis of T. Tiecke [9]. There, the most relevant potassium properties needed to perform and understand the different experiments and theoretical elements explained in the following chapters are presented in detail. This section summarizes some of its content in order to make this thesis self-contained.

General properties

The atomic number of potassium is Z=19. Natural potassium is mainly composed of three different stable isotopes: two bosons (^{39}K and ^{41}K), and one radioactively stable fermion (^{40}K). Table 3.1 shows the natural abundance of each isotope.

Mass number A	Neutrons N	Natural abundance (%)	Lifetime	Nuclear Spin I
39	20	93.2581(44)	stable	3/2
40	21	0.0117(1)	1.28×10^9 years	4
41	22	6.7302(44)	stable	3/2

Table 3.1: General properties of potassium isotopes

Optical properties

The optical properties of potassium relevant to quantum optics experiments are summarized in Table 3.2. These values are given for the strongest spectral lines: D1 $\left(^2S_{1/2} \longrightarrow {}^2P_{1/2}\right)$ and D2 $\left(^2S_{1/2} \longrightarrow {}^2P_{3/2}\right)$.

		D2-line	D1-line
Wavelength	λ	766.700921822(24) nm	770.108385049(123) nm
Lifetime	τ	26.37(5) ns	26.72(5) ns
Natural linewidth	$\Gamma/2\pi$	6.035(11) MHz	5.956(11) MHz
Recoil velocity	v_{rec}	1.335736144(7) cm/s	1.329825973(7) cm/s
Doppler Temperature	T_{D}	145 µK	145 µK
Saturation intensity	I_{sat}	1.75 mW/cm2	1.70 mW/cm^2

Table 3.2: Optical properties for ^{39}K

		D2-line	D1-line
Wavelength	λ	766.700674872(173) nm	770.108136507(144) nm
Lifetime	τ	26.37(5) ns	26.72(5) ns
Natural linewidth	$\Gamma/2\Pi$	6.035(11) MHz	5.956(11) MHz
Recoil velocity	v_{rec}	1.302303324(7) cm/s	1.296541083(7) cm/s
Doppler Temperature	T_D	145 µK	145 µK
Saturation intensity	I_{sat}	1.75 mW/cm2	1.70 mW/cm^2

Table 3.3: Optical properties for ^{40}K

		D2-line	D1-line
Wavelength	λ	766.70045870(2) nm	770.107919192(123) nm
Lifetime	τ	26.37(5) ns	26.72(5) ns
Natural linewidth	$\Gamma/2\Pi$	6.035(11) MHz	5.956(11) MHz
Recoil velocity	v_{rec}	1.2070579662(7) cm/s	1.2649577 88(6) cm/s
Doppler Temperature	T_D	145 µK	145 µK
Saturation intensity	I_{sat}	1.75 mW/cm2	1.70 mW/cm^2

Table 3.4: Optical properties for ^{41}K

Scattering properties

The scattering properties of the atoms are important to ensure thermalization during the evaporative cooling and the production of a degenerate quantum gases. In fact, stable BECs require having positive scattering lengths [4]. The *s-wave* scattering length can be estimated from the singlet a_s and triplet a_t scattering length presented in Table 3.5 for different isotopic potassium mixtures.

In the elastic approximation [84] the *s-wave* scattering length is given by

$$a \approx P_s a_s + P_t a_t, \tag{3.1}$$

where P_s and P_t represents the probability of the atom-pair to be either in the singlet or triplet state. The electronic spin configuration of potassium pairs has almost pure triple character, therefore $a \simeq a_t$.

Isotope	a_s **(a_0)**	a_t**(a_0)**
39/39	138.49(12)	-33.48(18)
39/40	-2.84(10)	-1985(69)
39/41	113.07(12)	**177.10(27)**
40/40	104.41(9)	169.67(24)
40/41	-54.28(21)	**97.39(9)**
41/41	85.53(6)	**60.54(6)**

Table 3.5: Scattering length for the different isotopic potassium mixtures.

In the different isotopic combinations presented in Table 3.5 we observe that there are combinations that do not need the use of Feshbach resonances to condense the sample. In particular the combinations ^{39}K-^{41}K, ^{40}K-^{41}K and ^{41}K-^{41}K have in common a positive and large background scattering length (bold values). This is why the central part of our experiment relays in the efficient production of ^{41}K degenerate gas to use it to sympathetically cool ^{39}K and ^{40}K.

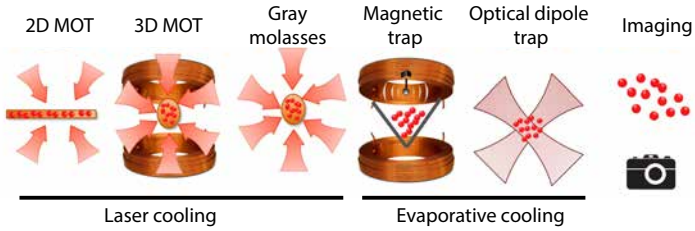

Figure 3.1: Basic scheme of the experimental sequence used to prepare a degenerate quantum gas of ^{41}K. Using a combination of laser cooling (2D MOT-3D MOT-molasses) and evaporative cooling (Quadrupole trap - optical dipole trap) techniques it is possible to prepare ultra-cold atoms every $\sim$ 45 s. At the end of the sequence the system is imaged by either absorption of phase contrast imaging.

3.2.3 *Cooling strategy: ^{41}K as coolant*

The key ingredient in our experimental approach is ^{41}K. On the one hand, the favorable scattering properties of this isotope allow its condensation without using Feshbach resonances, as demonstrated in LENS (Italy) [72], IEI (Tokyo) [78], MIT (US) [79], and HFN (China) [85]. On the other hand, ^{41}K can be used as a coolant for the other two isotopes. In fact, the quantum degeneracy of ^{40}K has been achieved by sympathetic cooling with ^{41}K [79]. In principle, the same technique should apply for the mixture ^{39}K - ^{41}K due to the positive background scattering length.

To provide an overview of our experiment, the cooling sequence used to obtain a degenerate quantum gas of ^{41}K is presented in Fig. 3.1. Minor changes are required to condense any of the additional isotopes. The experimental apparatus is shown in Fig.3.2 and the following list briefly summarizes each of the experimental steps.

- The experiment starts in a chamber with a high vapor pressure of natural potassium. A cold atomic beam is generated from the background pressure using a 2D Magneto-Optical Trap (MOT)

- The atoms are sent from the 2D MOT chamber to a ultra-high vacuum (UHV) science chamber where a 3D MOT captures the atoms. Subsequently, the density of the cloud is increased in a hybrid D1-D2 compressed MOT (CMOT).
- Gray optical molasses on the D1-line are used to obtain efficient sub-Doppler cooling.
- The atoms are prepared in $|F = 2, m_F = 2\rangle$ by optical pumping and captured in a magnetic quadrupole trap.
- Radio-frequency (RF) evaporation on the hyperfine transition leads to a phase-space density (PSD) of $\sim 10^{-4}$.
- The atoms are transferred to a hybrid trap (optical dipole trap beam plus a weak quadrupole field) and subsequently to a crossed optical dipole trap and evaporated to BEC. If required a Feshbach field is used to control the interactions during the final evaporation stage.
- The system is characterized using absorption imaging after time-of flight (ToF) or *in situ* phase contrast imaging.

We will now explain in detail the tools needed to implement each of these steps.

3.3 DESCRIPTION OF THE EXPERIMENTAL SETUP

3.3.1 *Vacuum setup*

The production of a degenerate gas requires an ultra-high vacuum (UHV) to avoid losses due to collisions between the atoms of interest and the background atoms. In this section, the design of our vacuum system is explained in detail.

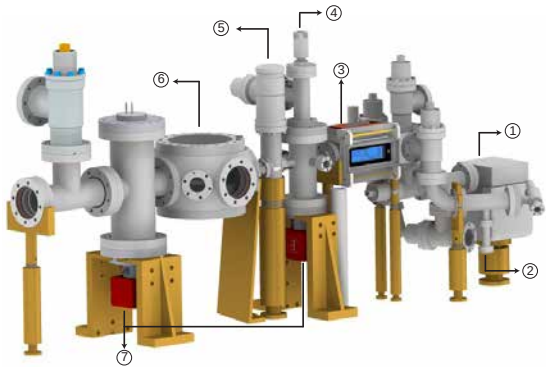

Figure 3.2: Experimental apparatus: 1) Ion pump. 2) Atomic source. 3) 2D MOT. 4) Mechanical shutter. 5) Gate valve. 6) Science Chamber. 7) NEG pumps.

General Features

The main part of the vacuum setup consists of two stainless steel chambers (the *science chamber* and the *2D MOT chamber*) separated by a gate valve and a mechanical shutter as depicted in Fig. 3.2. The vertical gate valve dissociates the two chambers; therefore both vacuum sections can be independent to each other. The mechanical shutter blocks the atomic beam coming from the 2D MOT during the sequence. The rotation of the shutter is induced with a magnetic rotary drive[1].

To obtain high vapor pressures of potassium on the 2D MOT chamber while keeping UHV on the science chamber, both sections are connected through a differential pumping tube (dpt). The differential pumping section is performed in two stages. First, the dpt is designed to keep pressure differences up to a factor of 1000 between the 2D MOT chamber and the first getter pump (see Fig. 3.3). The second stage is given by a CF16 bellow that connects the gate valve with the science chamber and gives an additional factor of 10. The overall differ-

1 MD16RAX000Z-Kurt J Lesker

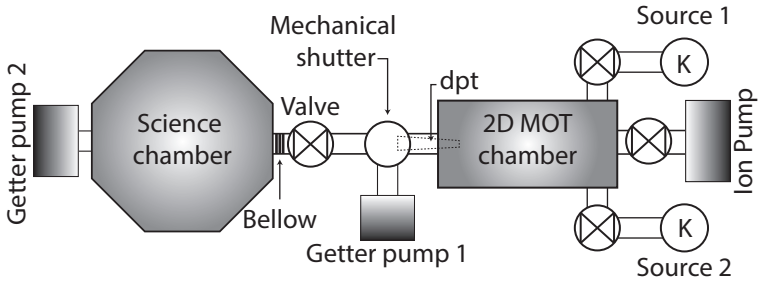

Figure 3.3: Sketch of the vacuum system. The two different vacuum sections are connected through the differential pumping tube (dpt). A gate valve between the science chamber and the 2D MOT chamber dissociates the two sections. The mechanical shutter blocks the atomic beam created in the 2D MOT chamber during the sequence. In addition, we place two more valves on the back of the 2D MOT chamber which allow to install or replace two independent potassium sources. Three different pumps are used to maintain the vacuum.

ential pumping section then offers $\sim 10^4$ pressure difference between the two chambers.

Note. The shutter is currently not used because during rotation the pressure read by the vacuum gauge[2] increases. We attribute it to outgassing of the in-vacuum ball bearings.

Pumping sections

To maintain the desired pressure in the experiment, we exploit three different pumps as shown in Fig. 3.2.

A 20 l/s ion pump[3] maintains the vacuum in the 2D MOT chamber. Initially, we installed a manual plate in front of the pump to control the conductivity of the pumping section; however, we replaced it later by a valve which has the advantage of allowing us to change the pump when it dies due to the presence of potassium. In fact, after two years of operation, the 2D MOT ion pump has stopped working. Allegedly

2 UHV-24p extended range ion gauge, dual-thoria-iridium filaments (9715015)- Agilent
3 TiTanTM 25S Ion Pump - Gamma Vacuum

the high vapor pressure of potassium damage the cathodes of such pumps. We achieve pressures of the order of 2×10^{-10} mbar before placing the potassium source in the chamber. In the presence of potassium the pressure increases by almost two orders of magnitude.

On the other side of the differential pumping tube, the vacuum system is maintained by two Non-Evaporable Getter (NEG) pumps[4] of 200 l/s (pump 1) and 500 l/s (pump 2). The pumping speed leads to pressures limited by the reading of our vacuum gauge[5] (10^{-11} mbar). This relatively new technology offers a very compact and lighter design than any other type of commercial pumps for UHV.

4 NEXTorr D500 and NEXTorr D200 - SAES Getters

5 UHV-24p extended range ion gauge, dual-thoria-iridium filaments (9715015)- Agilent

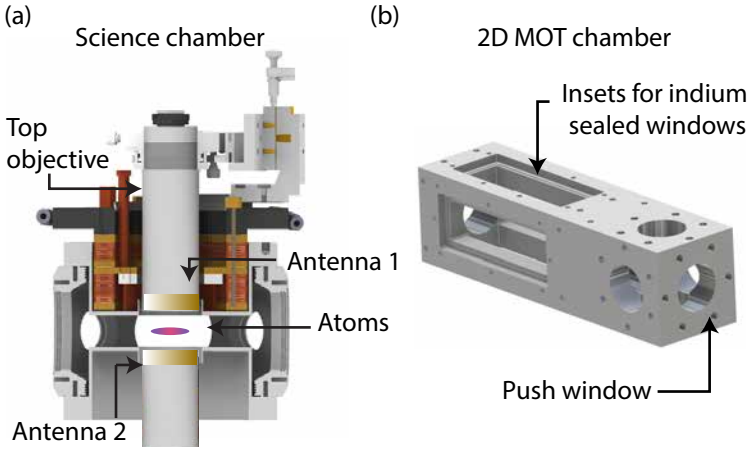

Figure 3.4: Sketch of the two main vacuum chambers. (a) The science chamber provides large optical access in the different directions through its several windows. All of them are anti-reflection (AR) coated from both sides at different wavelengths. (b) The full 2D MOT chamber is made of electro-polished stainless steel. In comparison to the one in [86], the chamber is longer with a size of 255 mm × 70 mm × 70 mm. The large rectangular windows (120 mm × 40 mm) are anti-reflection (AR) coated from both sides at 767 nm.

The science chamber

All the experiments presented in this thesis are performed in the science chamber. The design of our chamber takes into account several requirements:

- Ultra-high vacuum (UHV)
- Large optical access
- Magnetic coils close to the atoms
- RF antennae close to the atoms and in-vacuum antenna

To fulfill these conditions we have chosen the octagonal stainless-steal chamber[6] presented in Fig. 3.4 (a). In the vertical direction two

6 8.0" Spherical Square MCF800-SphSq-G2E4C4 - KIMBALL

CF150 custom re-entrant view-ports[7] allow implementing a high numerical aperture imaging system (see section 3.4). The 6 mm thick re-entrant viewport has a 50 mm clear view. Before welding it to the vacuum flange, the specifications are a transmitted wave-front error (TWE) $\lambda/10$ at 767 nm (imaging transition of potassium). The distance between the inner surfaces of the re-entrant viewports is 30 mm. This allows us to implement large MOT beams[8].

The magnetic coils are placed inside the re-entrant view-ports, this allows to produce large magnetic fields with small power supplies where the atoms are. Finally, we can place the antennae ((1) and (2), see Fig. 3.4 (a)) close to the viewports to manipulate the internal states of the atoms *via* RF and increase the coupling efficiency to the atoms.

In the transverse direction of the chamber the access is provided by two CF-63 and four CF-40 viewports. All view-ports are anti-reflection (AR) coated for several wavelengths[9] (AR 405 + 532 + 767 + 852 + 1064 + 1178nm/0°), see Appendix A.1 for more details. Finally, we install in one of the two CF-16 ports a power feedthrough that connects to an in-vacuum antenna.

The 2D MOT chamber

The 2D MOT chamber shown in Fig. 3.4 (b) is a home-made design similar to [86]. The rectangular shape provides large optical access which is used to implement large elliptical MOT beams that increase the atomic flux of the 2D MOT. Due to the chamber geometry, there are no commercial rectangular view-ports available, instead we use

7 Spectrosil synthetic fused silica - UKAEA special techniques group

8 Potassium has large light assisted collisions during the MOT stage; therefore large beams and large detunings are required to reduce the density of the cloud and increase the atom number in this stage [87, 88].

9 custom made - LaserOptik

indium-sealed[10] AR coated rectangular windows[11] (see coating details Appendix A.1).

In the push window (see Fig. 3.4 (b)), we initially installed a CF40 viewport[12] made of a fused silica window brazed with Kovar[13] onto a 304 stainless steel flange. After only ten months of operation, a considerable leak appeared on this viewport, presumably due to a reaction between Kovar and potassium. Our experience is that glass-to-metal transitions react with alkali atoms in short/long term.

To circumvent this problem, we replaced our CF-40 viewport with a demountable viewport conflat flange[14]. In this sort of viewports, the window is mounted to the flange with the help of a Viton ring that provides the air-tight metal/glass seal. In our case, we have replaced the Viton ring by a 4 mm indium wire. This ensures good vacuum. In addition, indium seals do not react with alkali atoms. To date, we have not observed vacuum problems in this configuration.

The potassium source

The atomic sources (source 1 and source 2 presented in Fig. 3.3) consist of potassium ampoules placed inside of a CF16 vacuum bellow (see Fig 3.2). These are connected to the 2D MOT chamber through two CF16 valves[15] as sketched in Fig 3.3). These valves allow us to switch between the two sources arbitrarily. In our current experiment, we have used only one source where we have placed a 5 g ampoule of natural potassium[16]. In the second source a 30 mg enriched sample[17] of ^{40}K will be installed for future experiments.

10 Indium wire 99.99% ⌀ 4mm (1N522407)-Advent research materials
11 AR 767 nm/0°- LaserOptik
12 CF40 Fused Silica view-port 304L / Kovar - Trinos
13 Kovar is a nickel-cobalt ferrous alloy that allows building glass-to-metal seals.
14 VPCH42-Thorlabs
15 54124-GE02-0001 - VAT
16 244856-SygmaAldrich
17 ^{40}K enrichment 10% - Trace Sciences International

Under vacuum, we broke the potassium ampoule by just twisting the CF16 bellow manually. By implementing a temperature gradient from the source to the 2D MOT chamber (see section 4.1.1), the potassium migrated in approximately one week. Using Doppler spectroscopy, we reveal the presence of potassium in the chamber. The vapor pressure in the chamber is $\sim 5 \times 10^{-8}$ mbar.

Note. During the first days of heating, we have observed a dramatical increase in pressure of both the 2D MOT chamber and science chamber. After one week, these values went down and a signature of the presence of potassium in the 2D MOT chamber was measured. We suspect that the huge increase in pressure could be related to the purity of our potassium ampoule. This pollution could come from the filling and sealing of the ampoules, which needs to be pumped first.

3.3.2 *Laser system*

Laser cooling of potassium isotopes

Here we present the laser system that generates the frequencies required to trap, cool down and detect the three different isotopes of potassium.

In our experimental sequence, we use both the D2-line ($\lambda_{D2} = 766.701$ nm) and D1-line ($\lambda_{D1} = 770.10$ nm) to perform either laser cooling, optical pumping or detection of the cloud. Fig. 3.5 shows the level scheme of the three isotopes of interest. We depict the cooler (red)- repumper (blue) and optical pumping (orange) transitions. The energy spacing between the states is given with respect to the cross-over resonance of ^{39}K (black dashed lines) which is our reference locking point.

For the three different isotopes we use D2 transitions during the 2D MOT and 3D MOT stage. The D1 transitions are used to perform

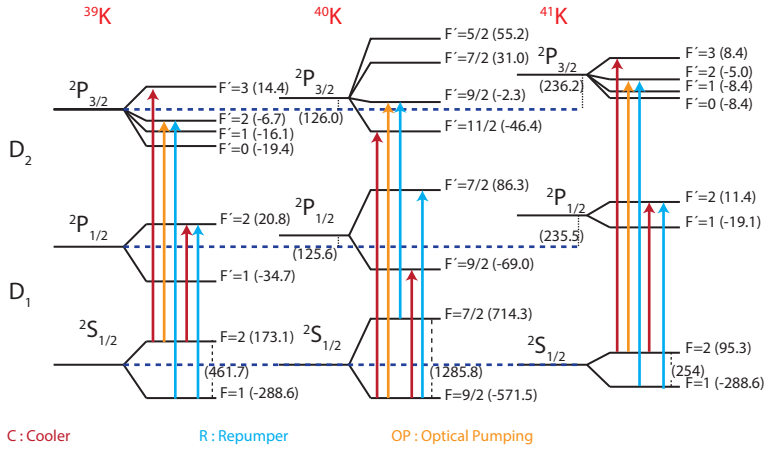

Figure 3.5: Fine and hyperfine states of the three potassium isotopes. In parenthesis we show (in MHz) the energy shift between the states respect to the cross-over resonance of ^{39}K. The cooling, repumping and optical pumping transitions are indicated.

sub-Doppler cooling in optical molasses and optical pumping. On the CMOT stage, we employ both transitions.

Due to the small and similar energy splitting of the relevant transitions (see Fig. 3.5) on each isotope, it is possible to develop a shared-laser system that can easily bridge all the transitions by using either acousto-optical[18] (AOM) or electro-optical (EOM) modulators[19]. Compared to mixture experiments with different atoms, here we do not need to build independent laser systems with different wavelengths. However, in dual-operation (^{41}K-^{39}K or ^{41}K-^{40}K) it is important to ensure that the optical transitions of each of them do not overlap or induce undesired heating. Fig. 3.6 shows the frequency distance of the cooler (C), repumper (R) and optical pumping (OP) transitions respect to the D2 (left panel) and D1 (right panel) cross-over of ^{39}K.

From Fig. 3.6 we can conclude that the laser cooling in dual-operation works since there is no overlap between the light needed on each iso-

18 ATM-A1/A2 series ,Tellurium Dioxide (TeO_2) - IntraAction Corp
19 Electro optic phase modulator (EO-D250/450L3) - Qubig

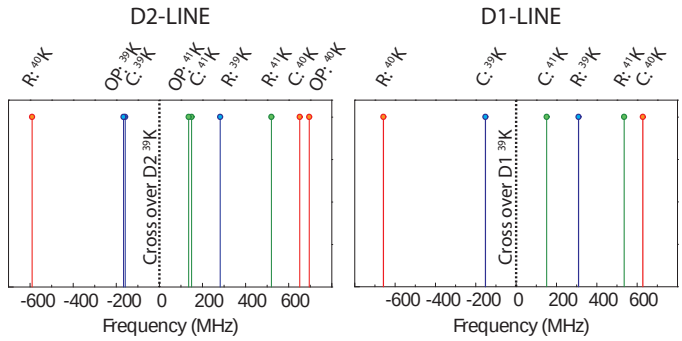

Figure 3.6: Frequeny distance of the different optical transitions required in the experiment. The notation is cooler (C), repumper (R) and optical pumping transition (OP). The different colours denote the frequency for each isotope (^{39}K-blue,^{40}K-red, ^{41}K-green). The values are computed with respect to the D2 (left panel) and D1 (right panel) ^{39}K cross over.

tope. The closest transitions are at around 22 Γ far apart (C:^{40}K with R:^{41}K and R:^{39}K with C:^{41}K). Therefore crosstalk can be neglected during laser cooling.

Laser system: Overview

Given the potassium structure and the optical transitions required, we sketch in Fig. 3.7 the central part of our potassium laser system. This is briefly summarized in the following:

- A **D2-master laser** is stabilized spectroscopically on the crossover of the D2-line of ^{39}K by using a potassium vapor cell heated up to 65 °C. This laser is used as a frequency reference for the D2 transition. Moreover, it is as well used for absorption imaging and 2D MOT push beam of the three isotopes.

- **Slave I** and **slave II** lasers are the cooler and repumper for ^{41}K. Both lasers are offset locked with respect to the D2-master laser with an optical beat-note frequency scheme [89]. Using this

scheme, we can scan the slave lasers in a range of up to 5 GHz with respect to the locking point. The latter is limited only by the bandwidth of the electronic components.

- **Slave III** is used for laser cooling of the additional isotope (either ^{39}K or ^{40}K). The cooler and repumper frequencies correspond to the carrier and a sideband created with an EOM. The laser is offset locked with respect to the D2-master laser.
- **Slave IV** is only used for our phase contrast imaging (Faraday imaging). It is offset locked with respect to the D2-master laser.
- A **D1-master laser** is stabilized spectroscopically on the crossover of the D1-line of ^{39}K by using a potassium vapor cell heated up to 100 °C[20]. The cooler and repumper transitions correspond to the carrier and a sideband of an EOM respectively. After amplification, this laser source is used during the CMOT, optical pumping, gray molasses and (if required) repumper during the absorption imaging.
- **D1-additional isotope laser** is used to implement D1-molasses in any of the additional isotopes in dual-operation (either ^{39}K or ^{40}K). This laser is offset locked with respect to the D1-master laser.

Laser system for ^{41}K

The 2D MOT, 3D MOT, and imaging of ^{41}K are based on a laser system tuned at λ_{D2}. Fig. 3.5 shows the internal structure where the cooler (red) and repumper (blue) transitions are red detuned γ from the corresponding transition. The cooler (slave I) and repumper (slave II) light

20 This cell is heated up more than the one used to lock the D2-master laser due to the difference in coupling strength of the D1 and D2-transition. Here a higher vapor pressure is required to obtain a comparable absorption signal

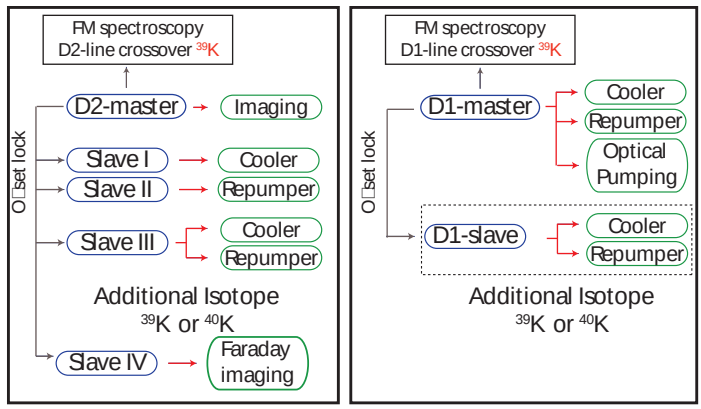

Figure 3.7: Schematic of the laser setup used on the experiment.

comes from a distributed feedback laser[21] (DFB) amplified to 1.5 W using a home-made tapered amplifier[22] (TA). The beams are controlled both in frequency and intensity. Finally, they are split for the 2D MOT and 3D MOT.

The D1-molasses in potassium require a narrower laser source than a DFB (linewidth $\sim$ 1 MHz) [85, 90–92], therefore we employed an external cavity diode laser in Littrow configuration (linewidth $\sim$ 300 kHz)[23] tuned at λ_{D1}. Here the cooler and repumper transitions correspond to the carrier and sideband of an electro-optical modulator (EOM) placed before a 1.5 W home-made TA[20]. The relative frequency between both transitions is fixed and corresponds to the hyperfine splitting of the ground state (for ^{41}K $\sim$ 254 MHz). The inherent second sideband produced by the EOM is more than 40 Γ blue-detuned from the transition. We do not observe additional heating effects in its presence.

21 EYP-DFB-0767-00050-1500-TOC03-0005 - Eagleyard photonics
22 EYP-TPA-0765-01500-3006-CMT03-0000 - Eagleyard photonics
23 SYST DL PRO 780 - TOPTICA

Additional isotope: Laser system for ^{39}K or ^{40}K

The laser system for the additional isotope is composed of two laser sources: a DFB laser tuned on the D2-line (Slave III) and an external cavity diode laser tuned at λ_{D1}. Both laser sources are combined in a single fiber by using an interference filter[24] at 780 nm. Interestingly, by placing this filter at 17°with respect to the incident light, λ_{D2} is reflected while λ_{D1} is transmitted. We combine with more than 95% efficiency two sources with the same polarization and only 3 nm difference.

After combination, both beams pass through an EOM (C-carrier/R-sideband) and then they are subsequently amplified using a single TA[20]. In the experimental sequence, first the λ_{D2} light is used during the MOT. It is then switched to the λ_{D1} light for the molasses stage.

Note. In dual-operation, ^{39}K atoms are cooled down through sympathetic cooling with ^{41}K. Due to the high efficiency of this technique, large MOTs are not needed to obtain a degenerate gas. Therefore, using one single laser source and an EOM is enough to trap the required atom number.

2D MOT and 3D MOT splitting

The laser beams are coupled into polarization maintaining fibers and sent to the "experimental table". For the 2D MOT, 3D MOT and molasses stages, we need to combine beams of very similar frequencies (cooler and repumper of ^{41}K and ^{39}K). As dichroic optics cannot be employed, we use instead a 4→4 fiber cluster[25]. By means of the evanes-

23 SYST DL PRO 780 - TOPTICA

24 B-06650: IF780nm/6° - LaserOptik

25 Spliceless PM Coupler arrays (optimized in between λ_{D1} and λ_{D2}) - Evanescent Optics Inc

cent field in the fiber, the four different inputs are mixed and the four frequencies are delivered at each output.

We have observed that adjusting the input polarization of the beams is critical; otherwise, the splitting ratio on each output could have significant power fluctuations. The latter is solved by placing a high-quality polarization beam splitter aligned with the fast axis of the fiber. Moreover, a proper thermal stability of the splitting box is required.

We use one cluster for the 2D MOT chamber and one for the science chamber.

3.3.3 *Magnetic fields: Overview*

One of the most appealing features of potassium is the tunability of its interactions *via* Feshbach resonances. Therefore, a homogeneous magnetic field along the extent of the cloud is required to control the scattering length a. Depending on the isotope or internal spin state, the Feshbach resonance properties can change dramatically in position and width. Several resonances have been reported in ^{39}K [77] and ^{40}K [75, 76, 93, 94] together with the mixture ^{40}K-^{41}K [79]. These resonances range between 20 and 560 G; therefore a good magnetic coil design is needed to fulfill, at low or high B-field, stability and homogeneity. For this aim and inspired by ref. [95], we designed a Bitter-type electromagnet in our experiment.

The Bitter configuration, traditionally used in high field magnets, allows for parallel cooling of the different coil layers avoiding unwanted coil heating.

The Bitter coil

Principle of operation. The Bitter-type electromagnet is depicted in Fig. 3.9 (a). It is constructed from solid copper arcs (1 mm thickness) in which the current flows in a helical pattern. The arcs are insulated

using silicon[26] layers (0.3 mm thickness) with the same shape as the copper arcs, but with small channels through which the water can flow(blue arrows). The successive copper arcs are rotated one-eight of a turn, and with the help of a copper insert the current can flow from one copper layer to the other.

In total we use 36 copper arcs which are splitted for the Feshbach coil (24 copper arcs) and jump coil (16 copper arcs), see Fig. 3.8 (b). Each assembly is delimited with a thicker copper arc (depicted in yellow in Fig. 3.8 (b)) that is used as an input/output of the current in the coils.

The full assembly is held with eight threaded brass rods which press the copper arcs against each other with a nut and a sealing washer. One rod and one nut are made of copper in order to drive the current in the Feshbach coil, the rest are made of brass. In addition, the rods are teflon-coated in order to avoid electrolisis between the coils.

Water cooling mechanism

In contrast to the hollow copper tubing coils, the advantages of a Bitter type electromagnet is the very efficient water cooling mechanism. The water flows in parallel through each insulating layer maintaining in this way each layer of the coil at the same temperature. Therefore, temperature gradients along the coil are suppressed. This allows to operate the coils at high current (< 400 A) with low heat dissipation.

With only 4 bar of pressure we can operate the Bitter electromagnets at high current at room temperature. The water flow is provided by a chiller[27] filled with commercial drinking water[28]. In between the chiller and the coils, a 7 μm filter[29] is placed to prevent bottlenecks in the small channels due to impurities in the water circuit.

26 Silicone Rubber Sheet - 60 Shore A - Merefsa
27 P205-16968 WW-S - Termotek
28 Sant Hilari
29 7 μm filter (SS-4F-K4-7) - Swagelok

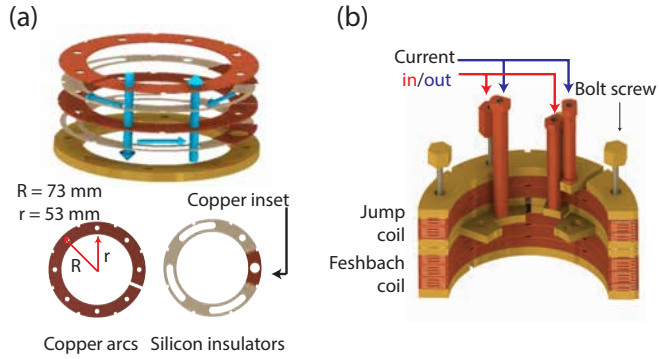

Figure 3.8: a) The Bitter configuration allows efficient parallel cooling of the different copper layers. Several alternated copper arcs allow the flow of current in a helical pattern. The water flows through the small channels on the silicon insulators (grey). (b) Half section view of the Bitter assembly. This consists of a Feshbach coil and a jump coil hold together with threaded bars.

The full Bitter assembly

A breakout of our magnetic coils is displayed in Fig. 3.9. The full assembly is made of two pairs of isolated Bitter coils (Feshbach coils and jump coils), one pair of coils made of enamelled copper wire (optical pumping coils) and also eight elliptic coils in "cloverleaf" configuration. This assembly allows us to produce homogeneous magnetic fields and magnetic gradients in different directions as follows:

- **The Feshbach coils** are the ones closer to the atoms, they produce either a homogeneous field or a quadrupole trap depending if they are in Helmholtz or anti-Helmholtz configuration. During the sequence, the quadrupole trap is employed during the MOT and magnetic trap while the homogeneous field is used to control the interaction of the atoms.

- **The jump coils** are used to either increase or decrease instantaneously the B-field (Helmholtz configuration) by switching them on/off. This circumvents possible limitations of the power sup-

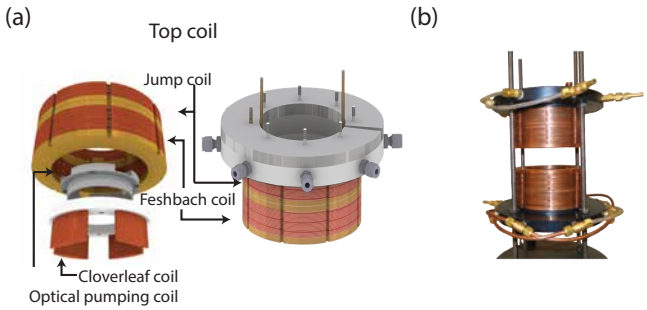

Figure 3.9: The Bitter assembly consists of a Feshbach coil, jump coil, optical pumping coil and an array of cloverleaf coils. The four coils allow producing homogeneous magnetic fields or gradients in different directions.

ply or PID bandwidths. In anti-Helmholtz configuration they produce a magnetic gradient needed to perform Stern-Gerlach separation during time-of-flight or spin distillation during the optical evaporation (see section 4.3.1).

- **The optical pumping coils** are used to define the quantization axis by creating a small homogeneous magnetic field (< 5 G). This pair of coils is mostly used during the optical pumping and imaging stage.

- **The cloverleaf (CL) coils** are used to compensate for the curvature or magnetic gradients that can be generated by the Feshbach coils in the radial direction.

In addition to the Bitter coil assembly, on each viewport of the science chamber, we installed copper wire coils that can be used for different tasks during the experimental sequence. They can be used either to create a homogeneous field for spin transfers or to control the position of the minimum of the quadrupole trap.

The earth field is compensated using three coils placed outside the optical table [30] .

Cloverleaf configuration

In Fig. 3.10 (a) we depict the cloverleaf configuration used in our experiment. This configuration allows us to compensate gradients or curvatures along the radial plane even in the presence of a transversal strong magnetic field.

Each pair of coils (denoted with and without "*") are connected in Helmholtz configuration. Depending on the direction of the field, we compensate in any direction the magnetic gradients and curvatures. An example of a possible configuration is presented in Fig. 3.10 (b). In the top panel both pairs AA* and CC* produce a magnetic field in the same direction. In dotted red line is represented the magnetic field along the x-axis produced by the cloverleaf coils. The blue and green lines represent a homogeneous magnetic field created by our Feshbach coil with and without the presence of the CL coils. In the bottom panel the magnetic field produced by the CL coils is created in opposite directions. Here we induce a magnetic gradient (green line) or homogeneous magnetic field (blue).

For the droplet experiments presented in chapter 6 we have cancelled out magnetic gradients in the presence of a Feshbach field of ~ 50 G. Compensation of magnetic gradients is crucial for these measurements.

30 Two of these coils have a dimension of 160 cm $\times$ 150 cm (top and bottom coils) while the lateral coil has a dimension of 160 cm $\times$ 120 cm. All of them are made of 5 turns of 20 multi-wire planar cable

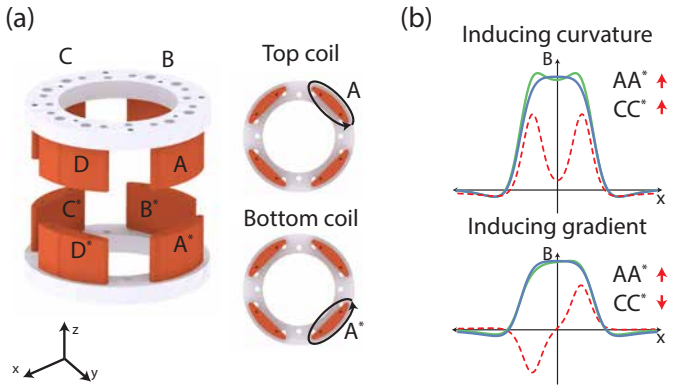

Figure 3.10: Cloverleaf coils. (a) Each pair of coils is connected in Helmholtz configuration. They are placed in a cloverleaf configuration aligned with respect to the vertical axis of the science chamber. (b) Depending of the direction of the magnetic field on each coil we can compensate for either magnetic curvatures or magnetic gradients along any direction in the radial plane.

Feshbach and jump coils electronics

As explained before, the Feshbach coils are used during the magnetic trap and also to provide a homogeneous bias field. During the experimental sequence the coils are changed from anti-Helmholtz to Helmholtz configuration by using an H-bridge circuit made of four mechanical relays[31]. As sketched in Fig. 3.11, by opening and closing the different relays we can control the current flow direction in only 100 ms. We use an FPGA to control the relay logic.

The switching on/off of the coils is provided by one high power IGBT[32] before the H-bridge circuit. In series to the IGBT a high power diode[33] is installed to protect the power supplies from any reverse current. Due to the inductive-load switching (on/off) generated by

31 LEV200A4NAF - Farnell
32 CM600HA-24H - RichardsonRFPD
33 LS410860 - RichardsonRFPD

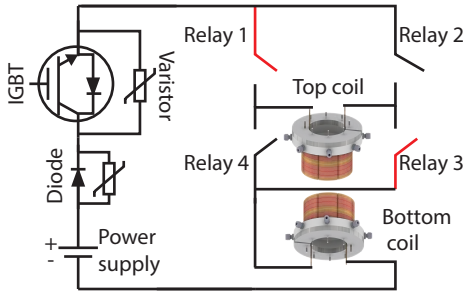

Figure 3.11: Four relays form the H-bridge configuration. When the relays R1/R3 are opened, and R2/R4 are closed, a positive voltage is on the coil. In contrast, when R2/R4 are opened, and R1/R3 are closed, the voltage can be reversed. This defines the Helmholtz or anti-Helmholtz configuration. In addition to the H-Bridge, the electronic circuit contains one IGBT that switches on and off the current of the coils, a varistor that protects the IGBT for transient signals and a high power diode that protects the circuit from reversed induced current.

the coils, a 95 V varistor[34] is placed in parallel to the IGBT to limit the transient peak voltage and protect the electronic circuit. The switch-off time of the coils is not limited by their inductance nor the circuit used (which leads to the extinction of 180 A in 50 μs), but by the eddy currents induced in the science chamber. This results in a switch off time of 100 G in $\sim$ 4 ms.

Stabilization of the Feshbach field

The stabilization of the magnetic field is essential to control the scattering length a precisely and is crucial if narrow Feshbach resonances are used. We deliver the current to the Feshbach and jump coils by using two different power supplies that range between 0 and 400 A and 0-50 A.

As a first approach, the jump coils are stabilized only by the internal PID of its power supply[35] while the current injected on the Feshbach

34 B72220S0950K101 - Farnell
35 Delta SM50-15- Delta

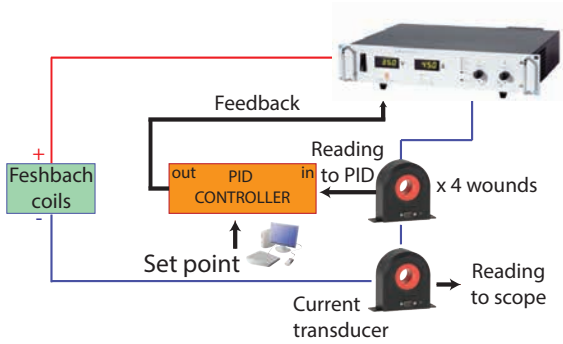

Figure 3.12: PID controller. The signal is boosted by increasing the number of turns around the current transducer. In our current configuration, four loops are wound around the current transducer. The noise in the PID controller can be improved by seeding the PID circuit with an automotive battery.

coil is stabilized with the locking scheme shown in Fig. 3.12. Here, the current given by the power supply[36] is measured with a high precision current transducer[37]. The signal then is compared with the set value imposed by the computer control[38] and fed into a home-made PID controller. This PID is designed along the same lines as ref. [96]. With this simple scheme, we were able to stabilize our magnetic Feshbach field up to $\pm$ 15 mG at 105 G. This stabilization technique was used for the Feshbach spectroscopy experiments presented in chapter 5.

In addition to the stabilization scheme, an extra current transducer[39] is used to readout the signal. To avoid unwanted noise, it is essential to have independent signals for reading and stabilization.

36 Delta SM400-15
37 DS600ILSA - DaniSense
38 We use National Instruments devices to control the experiment. The analog cards are the NI PXI-6733. The output of the cards are connected to a noise rejecting shielded BNC Connector Block (NI BNC-2110). The cards are installed in the PXIe-1082 rack. The experimental controll and interface were developed in the group of T. Esslinger at ETH.
39 DS600IDSA - DaniSense

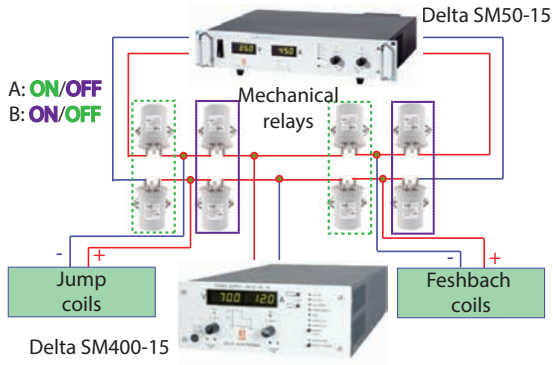

Figure 3.13: Power supply exchange. To improve the magnetic stability, we exchange during the sequence the power supply used for the Feshbach coils (A and B configuration). We match the range of the power supply to the current range required. This is done by using different mechanical relays.

The current stability is improved for the droplet experiments presented in Chapter 6 and 7 by performing some modifications in the locking scheme. First, we switched the power supplies between the Feshbach and jump coil during the experimental sequence by using mechanical relays (see Fig. 3.13). With this procedure, we matched the power supply to the current range required. To produce the quadrupole trap, where high current is required, we use a broad range power supply. However, when the coils are changed to Helmholtz configuration, the broad range power supply is exchanged by the small one.

In addition, the sensitivity of the current transducer is increased by wounding four times the copper wires that carry the current to the Feshbach coils.

Finally, the home-made PID is no longer connected to the AC transmission line but instead to two commercial automotive batteries. This suppresses the 50 Hz noise from the electric line. After these modifications, we measured through RF spectroscopy a magnetic field stability of $\pm$ 4 mG at 50 G.

Currently, in our experimental setup, we are limited by the magnetic field fluctuations in the environment. This will be solved in the future by implementing active magnetic stabilization similar to [97].

3.3.4 *Radio-frequency sources*

In our experiment, we use a radio frequency knife to evaporate the most energetic atoms in the magnetic quadrupole trap. It also allows us to prepare the internal state of the ultra-cold gas. Therefore a combination of several antennae, RF-amplifiers, and frequency signal generators are required.

The first stage of evaporative cooling consists of RF-evaporation in a magnetic quadrupole trap. In our cooling scheme, we only evaporate ^{41}K using RF. We use the transition $|F = 2, m_F = 2\rangle$ (low field seeker) to $|F = 1, m_F = 1\rangle$ (high field seeker) to remove the more energetic atoms. We evaporate using the hyperfine transition instead of the Zeeman one because during sympathetic cooling it allows us to selectively evaporate only ^{41}K.

The range of frequencies used during the RF evaporation ranges between 400 MHz and 265 MHz. We use a broad range flat response antenna (antenna 1) in combination with a 50 W RF amplifier[40] to address the transition. The antenna and RF amplifier are connected through a forward power circulator[41] to dump back reflections from the antenna. The frequency source is a commercial FPGA based frequency generator[42].

To manipulate and modify the internal state of the atoms, we perform either adiabatic frequency-sweeps or RF-pulses. This is done by using the antenna (2) in combination with a high power amplifier[43]

40 ZHL-50W-52-S+ - Mini-Circuits
41 F2520-0338-67S - WENTEQ
42 SD AOU-H3444-PXIe-1G - Signadyne
43 ZHL-100W-GAN+ - Mini-Circuits

and a frequency generator[44]. Different impedance matching circuits between the antenna and the amplifier are connected to maximize the RF-field at the location of the atoms. With this we broaden the atomic transition, and therefore we are less sensitive to magnetic field fluctuations.

3.3.5 *Far-detuned optical dipole trap: 1064/532 nm*

Harmonic traps

In the experiment, we trap the atoms optically in harmonic traps with either red (1064 nm) or blue (532 nm) detuned beams far from the potassium resonance.

The red detuned optical dipole trap beams in the experiment are created with a 25 W single mode YAG laser[45] with an ultra-narrow linewidth of 1 kHz[46]. The laser is protected against back reflections with a high power, high extinction ratio optical isolator[47]. The water cooling circuit is provided by a chiller[48] and monitored with a water flow sensor[49] interlock.

The power of this laser source is divided in different paths by using polarization optics[50]. In particular, one rotating waveplate[51] is installed to redistribute the power during the sequence into the different paths. Given the high power of the laser beams, the light is delivered to the

44 SMC100A Signal Generator - Rohde and Schwarz
45 Mephisto MOPA 25 W - Coherent
46 Value reported by the seller
47 Faraday Isolator FI-1060-5SC OEM4 - QIOPTIQ
48 P307-18344 WW-S - Termotek
49 800 Series flow meter - Proteus
50 Thin Film Polarizer (PO1045-FY) - Advanced Thin Films
51 PRM1Z8 - Thorlabs

atoms using single-mode photonic crystal fibers[52] with high power fiber couplers[53].

The crossed optical dipole traps (CDT) in the experiment are created by the intersection of the different beams presented in Fig. 3.14. Depending on the experiment performed, a different trap can be created with different trap depths and aspect ratio. The power of each beam is stabilized by using AOMs[54]. In particular, these AOMs are operated in opposite diffraction orders to avoid interference effects.

The blue-detuned lattice potential

The blue-detuned optical dipole beam is obtained from a single mode, single frequency optical fiber laser amplifier[55] at 532 nm. The laser source delivers 10 W of power using a seed of 30 mW from our Mephisto laser. The seed sets the linewidth of the blue-detuned laser. This laser source passes through an optical isolator[56] and then is coupled into a standard polarization maintaining fiber. The laser beam is stabilized in intensity as well with an AOM[57] placed before the fiber.

Besides the harmonic traps we have a small angle lattice potential for the droplet experiments presented in chapter 6. This setup was developed by P. Thomas [98]. The periodic potential is done by using the blue-detuned optical dipole beam presented before. The basic principle of our method is shown in Fig. 3.15. The 532 nm laser beam enters into a polarizing beamsplitter (PBS) cube that splits the light into two different paths. The horizontal beam is transmitted through the cube while the vertical one is reflected in a right angle prism[58] placed on top

52 LMA-PM-15 (SMA-905/SMA-905) - NKT Photonics.
53 60FC-SMA-T23-A7.5-03(input FIBER) and 60FC-SMA-T23-A15-03(output fiber) - Schäfter + Kirchhoff
54 ATM-A1/A2 series , Tellurium Dioxide (TeO_2) - IntrAction Corp
55 ALS-GR-532-10-A-SP - Azur Light systems
56 Tornos series 190-11944-0003-A - Electro-Optics Technology: EOT
57 ASM-B SERIES UV Grade Fused Silica - IntraAction Corp
58 Precision Bending Prism P90-050-532-UV - CVI Laser Optics

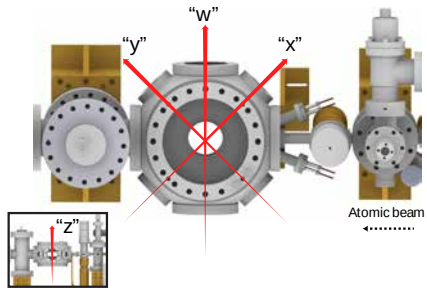

Figure 3.14: Axis convention. The different viewports are used to either image the atomic cloud or send dipole trap beams through. The convention is given for each axis and it will be employed along this thesis.

of the beamsplitter[59]. This setup produces a pair of parallel beams (at a distance D) which is then focused on the atoms with a single lens of focal length f. In the focal plane both beams interfere with a small angle θ, this produces a one-dimensional lattice potential of periodicity given by

$$d = \frac{\lambda}{2sin(\theta)}. \tag{3.2}$$

In our current setup, the lattice spacing is 10 μm. With this large lattice spacing, the loading of one single planes is straightforward. However, the probability to load more than one plane is not zero. Using the matter wave focusing technique introduced in [99], we measured that the population in other planes is below 5 %. More details about the characterization of our lattice potential can be found in [98].

3.4 IMAGING SYSTEM

In our experiment, the atomic cloud is characterized by using either absorption or phase contrast imaging. In the horizontal plane of the science chamber (X-axis, Y-axis, and W-axis), the atomic cloud is far

59 Fused silica PBS cube (L335534000)-PI Micos

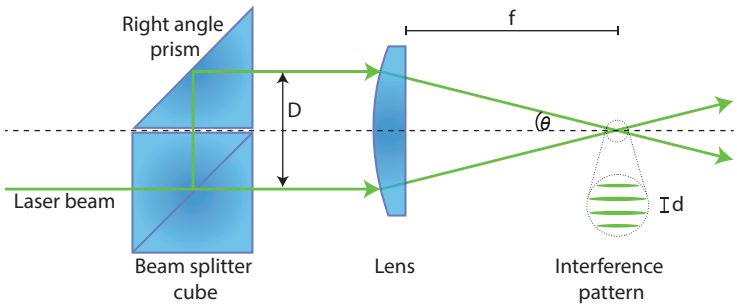

Figure 3.15: Schematic drawing of the lattice potential. Two parallel beams are produced by the combination of a beam splitter cube and a right angle prism. They interfere in the focal plane of a lens forming a periodic intensity pattern with spacing d. The beam spacing D is given by the size of the optical elements.

away from the viewports ($\sim$ 150 mm); therefore we use low-resolution optics and standard CCD cameras[60]. Here, we use standard absorption imaging techniques to obtain the atomic column density and the temperature of the gas after time-of-flight (ToF).

Along the vertical axis (Z-axis) the cloud is imaged *in situ* using dark field polarization phase contrast imaging [100, 101]. In contrast to the horizontal plane, here we have designed a high numerical aperture objective which consists of one catalogue aspheric lens[61] and one custom-made positive meniscus[62] [102] that corrects from the aberrations introduced by the viewport (see Fig. 3.16) . Thanks to the reentrant viewports explained in section 3.3.1, the asphere lens is only 35 mm away from the atomic cloud. This provides a numerical aperture of NA=0.43. The latter leads to a theoretical resolution of 1.1 μm (Rayleigh criterion) at 767 nm. In a test setup, the actual resolution has been measured to be below 1.5 μm [103].

60 CMLN-13S2C-CS- Point Grey
61 KPA24 - Newport
62 MSCP010 - Ross optical

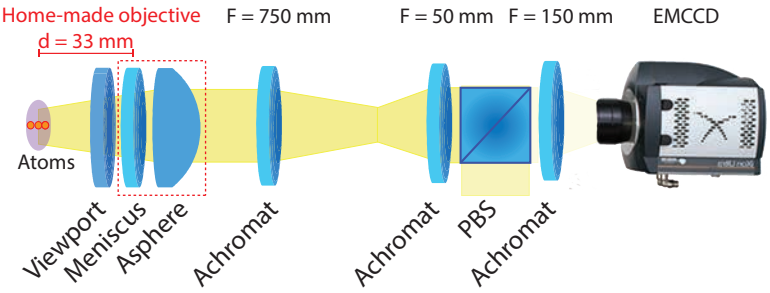

Figure 3.16: Homemade objective (red dashed area). Using an asphere lens and a commercial meniscus lens we obtain a high N.A objective (NA=0.43) and compensate the spherical aberrations introduced by the viewport. The lenses in the objective are mounted in a five-axis mount where it possible to control the different degrees of freedom. The best performance of the objective is achieved by aligning the objective perpendicular to the viewport. This is done by aligning the reflections of each optical element and make them overlap with the help of a probe beam. We magnify in two stages, besides the objective we use three additional achromat lenses to achieve a total magnification of $M = 49.6(9)$. The polarization beam splitter (PBS) is placed in the optical system to perform dark field phase contrast imaging.

The objective is mounted in a five-axis lens positioner[63] which allows controlling the different degrees of freedom required to align the objective with respect to the atoms and the 6 mm thick view-port[64] of the science chamber. The lens positioner is mounted in a high precision translational stage controlled by a piezo linear actuator[65]. This stage allows us to scan precisely the focal plane of the objective with respect to the atomic cloud.

In the final configuration the system has a total magnification of $M = 49.6(9)$ measured using Kapitza-Dirac diffraction[104] on a one-dimensional lattice potential.

63 LP-2A - Newport
64 Spectrosil synthetic fused silica - UKAEA special techniques group
65 N-470 PiezoMike Linear Actuator - PI

3.4.1 *Dispersive imaging*

Dark field polarization phase contrast imaging

Dispersive imaging techniques have been used in cold atoms experiments to perform non-destructive imaging of dense systems. The main idea is to measure the phase shift of the imaging light due to the presence of the atomic cloud. The scalar and vectorial part of the atomic polarizability gives this phase shift.

In our experiment, we use dark field polarization phase contrast imaging (DFPPC), also known as Faraday imaging. Here the vectorial part is the main contribution to the phase shift of our probe beam. The idea is to probe the atomic cloud with linearly polarized light, and measure its rotation due to the birefringence of the cloud. This rotation in polarization (Faraday angle θ_F) is measured by introducing a polarizer in between the cloud and the detector (see Fig. 3.17 (a)). In this way, we project the changes of polarization into intensity. In particular, we are in dark field configuration, this means, the polarizer does not transmit the light in the presence of atoms.

The Faraday angle θ_F is given by

$$\theta_F = c_F \, n_i \tag{3.3}$$

where n_i represents the integrated density of the cloud and c_F the Faraday coefficient.

The advantage of dispersive imaging techniques is the possibility to image in a non-destructive way the atomic clouds, however, far from the atomic resonance there is a low signal-to-noise ratio. To increase the contrast we acquired the signal in phase contrast imaging using an EMCCD camera[66].

66 iXonUltra897- Andor

3.4.2 *Atom number calibration*

Absorption imaging

An absolute calibration of the atom number in the experiment is performed with time-of-flight absorption imaging. Experimentally, we exploit the atom number dependence on the critical BEC temperature T_c (see Eq. 2.4). Here we take into account the shift of T_c due to interaction effects (scattering lengths of potassium computed by A.Simoni and M.Tomza) and finite size effects (see section 2.4.6). Detailed measurements of ^{39}K and ^{41}K T_c are presented in chapter 4. This calibration has a systematic uncertainty of 25%.

In situ imaging

We calibrate our *in situ* imaging system by measuring experimentally c_F of Eq. 3.3. We extract θ_F from the light intensity transmitted through the PBS due to the presence of the cloud.

To measure the phase shift (which is linked to c_F) imprinted by the atomic cloud, we have implemented a new scheme with the help of a rotating half-wave plate[67]. The idea is to record the response of the polarizer with and without atoms. We measure the transmitted light intensity vs. polarization angle of the light θ. We rotate the angle of the linear polarized light several multiples of π. A sketch of the response function obtained is shown in Fig. 3.17 (b). Both profiles with (green) and without atoms (red) follow the Malus´s law

$$I(\theta) = I_0 sin^2(\theta + \theta_F), \tag{3.4}$$

where I_0 represents the total intensity of the light and θ the angle set by the half-wave plate. The phase shift θ_F is given by the presence of atoms during the measurement.

67 PRM1Z8 - Thorlabs

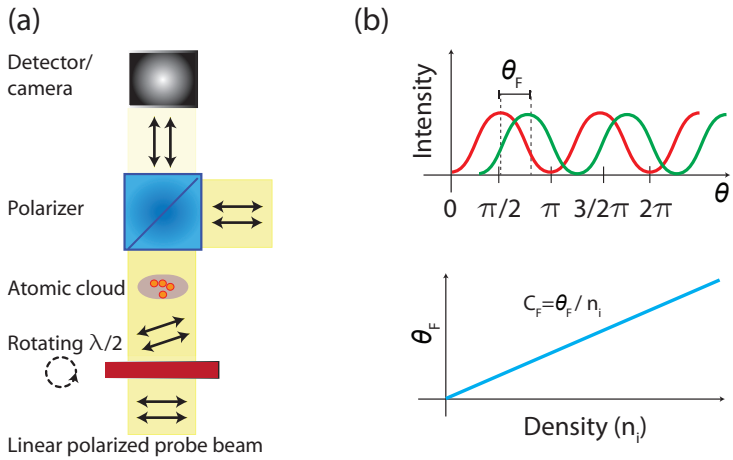

Figure 3.17: (a) Dark field polarization phase contrast imaging. The incoming light has a polarization orthogonal to the transmission of the cube. The detector records the phase shift in the presence of the atomic cloud. (b) Phase shift as a function of density. (top panel) We scan the response of the cube with (green) and without (red) the atomic cloud. We observe a phase shift of the light θ_F. (Bottom panel) Depending on the density of the cloud the θ_F increases. Here the Faraday coefficient is proportional to θ_F and n_c

The Faraday coefficient. Using a single-component BEC, the coefficient c_F is calibrated in two steps. First, we perform an absolute calibration of the atom number with absorption imaging as explained above. Then we measure directly the polarization phase shift as a function of n_i by performing measurements after different expansion times of the gas in a single-beam optical dipole trap. The density is given by the atom number N (calibrated in ToF), the volume of the cloud set by the harmonic oscillator length of the trap (measured in independent experiment) and the extension of the cloud after expansion in the optical waveguide.

In the linear regime, the value of c_F is represented as the slope of the θ_F vs n_i sketch in Fig. 3.17 (b).

Remarks.

- For a given density range of interest, the detuning of the light must be such that $0 < \theta_F < \pi/2$.
- If the detuning of the light is close to resonance, absorption effects need to be taken into account.

This phase contrast imaging technique is crucial in chapter 6 and chapter 7 to obtain qualitative results.

The development of the imaging system and its calibration has been mainly carried out by J. Sanz, and his Ph.D. thesis will describe it in more detail.

4

DEGENERATE QUANTUM MIXTURES: DUAL-BEC OF ^{39}K-^{41}K

In June 2015 we produced the first Bose-Einstein condensate of ^{41}K in our experimental apparatus. A few months afterwards the condensation of ^{39}K and the dual-Bose-Einstein condensation of ^{39}K-^{41}K were observed. In this chapter, we describe the experimental route employed to obtain the first quantum degenerate gases in our team.

4.1 LASER COOLING STAGE

The laser cooling stage is divided into different steps: 2D MOT, 3D MOT, CMOT, and molasses. Here the two different bosonic isotopes are trapped simultaneously on each step.

4.1.1 *Dual-2D$^+$ MOT of ^{39}K-^{41}K*

Vapour pressure of potassium

The road to the quantum degenerate regime starts in an enhanced 2D$^+$MOT. With a background pressure of $\sim 10^{-8}$ mbar of natural potassium (measured through the absorption of a propagating beam along the chamber [105]), we can selectively create an atomic beam of the three different isotopes by just tuning the frequency of cooler and repumper beams. The atomic flux for each isotope is limited by the partial pressure given by its natural abundance (see Table 3.1).

The potassium pressure is kept on the 2D MOT chamber by implementing a temperature gradient from the source to the 2D MOT

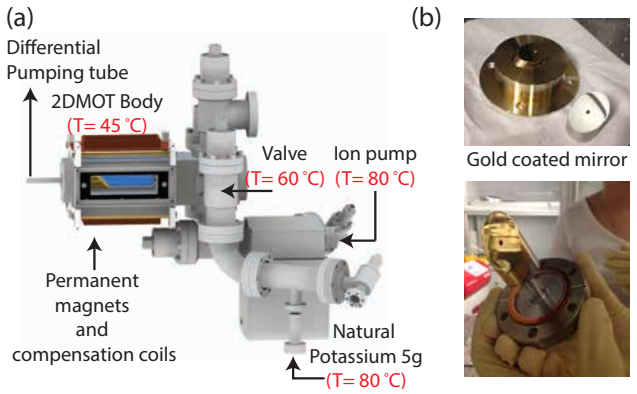

Figure 4.1: 2D MOT chamber. (a) The temperature gradient along the 2D MOT allows keeping the right vapor pressure needed to perform the experiments. Around the body of the 2D MOT chamber, four permanent magnets and 2 pairs of coils are placed to create the magnetic field required. (b) In the 2D$^+$MOT configuration longitudinal molasses are implemented with a gold-coated in-vacuum mirror. The top panel shows the polished steel mirror with and without coating. In bottom panel the in-vacuum mirror is mounted on the differential pumping tube.

chamber. The temperature gradient implemented is shown in Fig. 4.1 (a).

Several heating tapes[1] and PID controllers[2] are used to stabilize the temperature. We have observed that otherwise long-term temperature drifts modify the loading rate of the 3D MOT.

2D MOT configuration

In our configuration the 2D MOT consists of two pairs of retro-reflected elliptical beams ($1/e^2$ diameter = 70 mm $\times$ 20mm) and a pair of longitudinal molasses beams ($1/e^2$ diameter = 20 mm). These molasses provide longitudinal cooling allowing to increase the density of the cloud and therefore increase the atomic flux up to a factor of two on

1 SWH251-060 - Omega
2 CN77000 - Omega

each isotope [105, 106]. As shown in Fig. 4.2, the molasses are implemented by using a gold-coated in-vacuum mirror. We image a dark spot on the molasses beam to avoid distortions due to the mirror hole that connects to the differential pumping tube.

In addition, a small blue-detuned push beam ($1/e^2$ diameter = 800 μm) is used to transfer the atoms to the science chamber [107].

2D MOT in-vacuum mirror

On one end of the differential pumping tube explained in section 3.3.1, a home-made **45°gold-coated mirror** with a 2 mm hole in its center is installed in the front of the 2D MOT chamber (see Fig.4.1 (b)). The mirror is a polished piece of steel with three different layers deposited on its reflective side: titanium (100 nm), gold (100 nm) and SiO_2 (100 nm). The first layer is Titanium (Ti) because it is a common adhesive thin-film material used to attach gold on different surfaces. The gold layer increases the reflectivity of the mirror, and the SiO_2 one protects the mirror against potassium deposits due to the high vapor pressure. This prevents the decrease of the mirror reflectivity over time.

Magnetic fields and push beam

The magnetic field gradient required for the 2D MOT is created by four permanent rectangular magnets[3] placed around the 2D MOT chamber (see Fig. 4.1 (a)). This configuration creates a magnetic gradient of $B^{'}$ = 11 G/cm transversal to the 2D MOT chamber. We do not observe residual stray fields on the science chamber due to the presence of these magnets. More details about the magnetic field decay and characterizations of these magnets can be found in ref. [108].

Once the atoms are trapped in the 2D MOT, the clouds are sent to the science chamber with the help of a push beam aligned in the axis

3 6×6×148 NdFeB magnets (Q148x06x06Zn-30SH) - HKCM

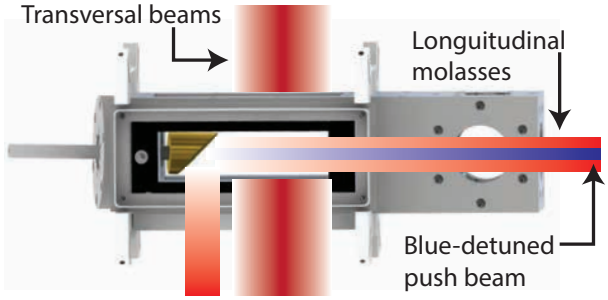

^{41}K-^{39}K	Total power (mW)	Detuning (Γ)
Cooler	160 - 60	-5.2 - -3
Repumper	92 - 30	-4.6 - -3
Molasses	7 - 2.5	-
Push beam	0.15 - 0.1	3 - 2.5

Figure 4.2: Configuration of our 2D$^+$ MOT. Two transverse elliptical beams and a pair of longitudinal molasses beams are used. One of them is directed to the atoms using the in-vacuum mirror. To avoid beam distortions due to diffraction by the hole, a dark spot is imaged on it. The table below presents the optimal parameters for our 2D$^+$ MOT.

of the atomic cloud. The push beam of each isotope is blue detuned from the cooling transition allowing to accelerate the atoms towards the science chamber (see beam parameters in Fig. 4.2).

We find that the best performance of our atomic source is highly sensitive to the centering of the 2D MOT (quadrupole and laser field) with respect to the mirror hole and push beam. Therefore, in addition to the permanent magnets, two pairs of coils in Helmholtz configuration are used to fine-tune the center of the 2D MOT quadrupole field. This is done independently for each isotope.

Best performance

The optimal parameters of the 2D MOT are indicated in Fig. 4.2. They are found by maximizing the fluorescence of the 3D MOT of each isotope. We measure a ^{41}K atomic flux of 1.8 $\times 10^8$ atoms/s extracted from the loading rate on the 3D MOT. Due to the higher natural abundance of ^{39}K, the flux is more than twice bigger (4.6 $\times 10^8$ atoms/s) although the beam intensities are lower compared to ^{41}K.

The atomic beam velocity for both cases ranges between 20-50 m/s depending on the detuning and power of the push beam. This has been measured by sending a probe beam at 45 °to the atomic beam and recording the fluorescence emitted when scanning its frequency around resonance [109].

4.1.2 *Dual-3D MOT and CMOT*

3D MOT. The atomic beam created by the 2D MOT is then captured in the science chamber in a 3D MOT. The dual-3D MOT consists of six independent beams ($1/e^2$ diameter = 22 mm), and a magnetic field gradient ($B^{'}$ = 5.3 G/cm) produced by the Bitter coils described in the previous chapter. Both cooler and repumper beams of each isotope are red detuned δ from the respective transition (see values Table. 4.1). The combination of such large beams, large detunings, and a small magnetic gradient gives, as a result, a dilute MOT. This dilute MOT reduces the particularly large light assisted collisions reported in potassium MOTs [87, 88].

The optimum dual-MOT-loading scheme is the following: we first load ^{41}K during 10 s (1/e loading time $\tau = 2.1(1)$ s), and then only during 650 ms, the ^{39}K MOT beams are switched on together with the ^{41}K beams. This scheme reduces the losses observed in the double-species MOT. With the parameters in Table. 4.1, around 1.5 $\times$ 10^9 atoms of ^{41}K and 3 $\times$ 10^8 of ^{39}K are captured. The population ratio between the

	^{41}K				^{39}K			
Stage	δ_c(D2) - I_s	δ_r(D2) - I_s	δ_c(D1) - I_s	δ_r(D1) - I_s	δ_c(D2) - I_s	δ_r(D2) - I_s	δ_c(D1) - I_s	δ_r(D1) - I_s
MOT	-6 - 6.8	-3 - 9	-	-	4 - 3.6	-4 - 2.1	-	-
CMOT	-	-3→-1.5 - 9→0	5.5 - 9.2	-	-	-	5 - 7	5 - 2.3
Molasses	-	-	5.5 - 9.2→0	5.5 - 3→0	-	-	5 - 7→0	5 - 2.3→0

Table 4.1: Optimal parameters during the MOT, CMOT and optical molasses sequence for ^{39}K and ^{41}K. The intensities reported are normalized respect to the saturation intensity I_s of the transition at resonance. The detunings δ are presented in units of Γ (linewidth of the transition).

two isotopes can be tuned easily by adjusting the MOT loading time of ^{39}K.

CMOT. To further increase the density of the atomic clouds, a hybrid D1-D2 CMOT strategy is employed on ^{41}K [90] while performing during this time a sort of gray molasses for ^{39}K.

In the ^{41}K CMOT the cooling is performed on λ_{D1} while the repumper transition is on λ_{D2} (see detuning Table 4.1). The CMOT lasts 100 ms. The experimental sequence of the CMOT stage is summarized in Fig. 4.3.

In our experimental sequence, we first reduce the I_{rep} ^{41}K to zero while keeping the maximum power in the D1 I_{cooler}. During this time, instead of increasing the magnetic gradient we reduce it to 3.8 G/cm. We have observed that compressing the magnetic field gradient enhances the losses in the system. We do not perform a CMOT in ^{39}K due to experimental constraints, because in our current setup we use sequentially the same tapered amplifier for both λ_{D2} and λ_{D1} (see section 3.3.2).

After using this hybrid scheme, interestingly each isotope reaches temperatures close to 70 μK. This value is lower than the Doppler temperature (T_D) of potassium ($T_D \sim 145\mu$K). Similar to the observations reported in ref. [90], the ^{41}K CMOT experiences a gray molasses type cooling in the presence of the blue-detuned D1 light. In the case of ^{39}K, it just experiences a long time D1 molasses. Due to the weak

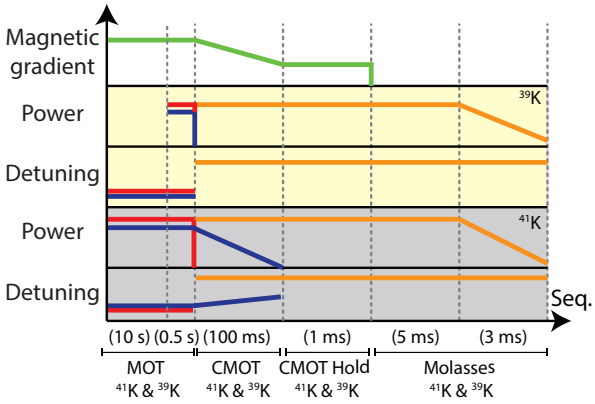

Figure 4.3: Sequence used to laser cool ^{41}K and ^{39}K. The lines in the drawing just indicate the change of magnitude of the parameter, and not the exact ramp shape. The cooler and repumper transitions on the λ_{D_2} are represented in red and blue respectively. The cooler transition in λ_{D_1} is represented in yellow. The repumper transition on the λ_{D_1} is created with a side-band of an EOM and is not represented here. The green line represents the magnetic gradient used during the MOT and CMOT.

magnetic gradient provided by the CMOT, ^{39}K reaches sub-Doppler temperatures as well.

Finally, the magnetic field is removed, and the clouds are further cooled down in the molasses scheme described below.

4.1.3 *Sub-Doppler cooling with D1 gray molasses*

Dual-D1 gray molasses. Compared to other alkali atoms, potassium has a relatively narrow hyperfine structure in the excited state of the D2 manifold. This is shown in Fig. 3.5. The energy splitting of the F' sublevels are on the order of the natural linewidth ($\Gamma = 2\pi \times 6.03$ MHz), therefore having an isolated single cooling transition is complicated due to the presence of off-resonant excitation. With this limitation, traditional sub-Doppler cooling on the D2-line has been difficult to achieve with standard optical molasses. Although a more complex scheme implemented in ref. [110] allows to achieve sub-Doppler tem-

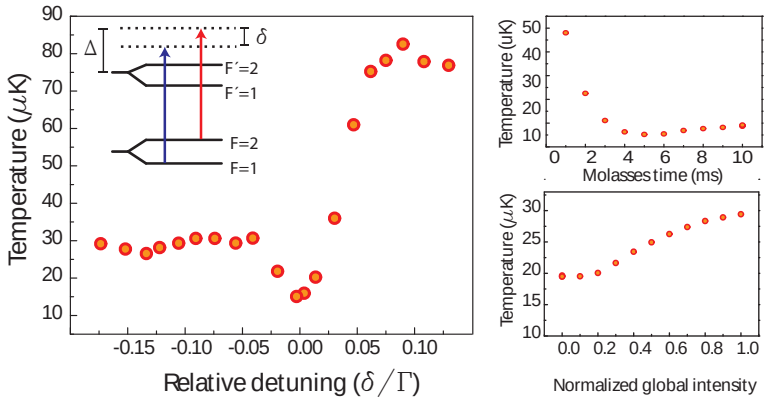

Figure 4.4: ^{41}K gray molasses characterization. (Left panel) gray molasses rely on a Λ level scheme where the detuning $\delta = 0$ provides the optimum parameters. We observe for $\delta < 0$ that the temperature of the atomic cloud is approximately constant (25 μK) while for positive values of δ a resonant heating increases the temperature of the system. (Right panel) In this Sisyphus-like cooling mechanism, the "height of the hills" needs to be reduced to cool down efficiently the cloud [69], we observe that by lowering the global intensity of the beams we achieve sub-Doppler temperatures in tenths of milliseconds.

peratures in ^{39}K, this method is highly sensitive to power balance, detuning parameters and intensity of the cooler and repumper beams. To circumvent these problems we use the D1-line.

A first reason to use the D1-line is that its states for all isotopes are well resolved. Therefore off-resonant excitation is less important. Here we implement the so-called *gray molasses*. In particular, this laser cooling technique has been reported to work successfully for the different potassium isotopes [85, 90, 91].

In our experimental setup, we perform this sort of molasses for both isotopes simultaneously. We obtain sub-Doppler temperatures by using a Λ-configuration between the F=1 (repumper) - F=2 (cooler) hyperfine ground states and F′=2 D1 excited state of ^{39}K and ^{41}K (see inset Fig. 4.4). We observe that the relative detuning between cooler δ_C and repumper δ_R beams is a critical parameter that defines crucially

the final temperature of the cloud. Fig. 4.4 (a) depicts the temperature dependence of the cloud as a function of the Raman detuning ($\delta = \delta_C - \delta_R$). For $\delta/\Gamma < -0.15$ the temperature of the cloud is $\sim 25\mu$K. Interesting close to $\delta = 0$ a narrow feature appears lowering first the temperature of the cloud close to 16 μK ($\delta < 0$) followed by resonant heating for $\delta > 0$. This effect is observed for both ^{39}K and ^{41}K with similar results.

We study the temperature of the cloud as a function of the global detuning Δ ($\Delta = \delta_C = \delta_R$) of ^{39}K and ^{41}K. The final temperature of the clouds is reduced below the Doppler cooling limit for a broad range of positive detunings as soon as we are blue-detuned from the transition.

As explained in 3.3.2, in ^{39}K as in ^{41}K the cooler and repumper frequencies are the carrier and sideband created by an EOM. The optimal amplitude ratio between the carrier and side-band is $\sim$ 2:1 for both cases. The additional side-band created in both cases by the EOM is so far detuned from the cooling transition (by the hyperfine splitting) that heating effects are not observed.

In conclusion, with the saturation intensities presented in Table 4.1, by reducing the global intensity of the D1 beams in 8 ms we cool down to sub-Doppler temperatures (from $\sim$ 70 μK to $\sim$ 16 μK) the two bosonic isotopes of potassium (see Fig. 4.4 right panel). We achieve at the end of this stage typical atom numbers of 8×10^8 and 2×10^8 for ^{41}K and ^{39}K respectively.

This stage is extremely robust against external magnetic fields[4] and global detuning of the laser beams. However, we observe that it is highly dependent on the relative detuning between the cooler and repumper light. Similar results have been previously reported in single species potassium experiments for ^{39}K and ^{40}K [90, 111]. Here, in addition, we have explored the molasses scheme for ^{41}K and dual-molasses ^{41}K - ^{39}K.

4 We passively cancel out residual magnetic fields on the position of the atoms below 5 mG.

Note. In addition to the both MOTs, by using the same experimental setup we have already produced a MOT of the fermionic isotope ^{40}K. After 30 s of loading time, we trap approximately 5×10^5 atoms in the 3D MOT. We are currently employing a natural potassium source, and the abundance of the fermionic isotope is only 0.01%. This number should be sufficient for our sympathetic cooling strategy to work and create a degenerate Fermi gas. Nevertheless, a solid sample enriched of ^{40}K has already been purchased and will be installed, if necessary, during the upcoming years.

4.2 EVAPORATIVE COOLING IN CONSERVATIVE TRAPS

4.2.1 *Optical pumping and spin purification*

After the laser cooling stages, the atoms are transferred into conservative traps. In our case, we first load the atoms in a magnetic quadrupole trap. Here the system needs to be prepared in a low-field seeker state that can be trapped by the magnetic gradient. In our case we decide to transfer the atoms to the state $|F = 2, m_F = 2\rangle$. This transition is particularly easy to prepare by just optically pumping the atomic cloud with circular polarized resonant light. This can be achieved by using either the D1 or D2 transition.

In our experiment, we optically pump using the D1-line. In comparison to the D2 transition, the well resolved hyperfine structure allows us to prepare colder and purer samples. In this way, the initial conditions of the RF evaporation stage are improved, and unwanted two-body collisions are suppressed. The optical pumping sequence consists of two stages: with a bias field of 2.5 G, we first repump the atoms from $F = 1 \longrightarrow F' = 2$ during 100 μs (hyperfine pumping). Then a 200 μs pulse with circularly polarized resonance light on the

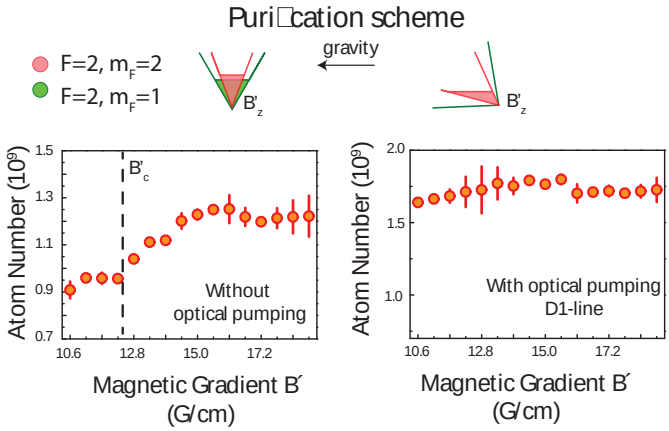

Figure 4.5: (top panel) By reducing the magnetic gradient atoms with lower magnetic moment cannot be held against gravity. (left panel) No optical pumping. The ^{41}K atom number is sketched as a function of the purification magnetic gradient. The step close to 12.8 G/cm is an indication of the critical gradient B'_c needed to hold the atoms in states different from $|F = 2, m_F = 2\rangle$. (right panel) Optical pumping in the D1-line. Within error bars, the atom number remains constant for any value of B'. This is a clear indication of the spin purity of the cloud.

D1 transition $F = 2 \longrightarrow F' = 2$ is applied (Zeeman pumping). This is performed for both isotopes simultaneously.

At the end of the optical pumping stage, around 100% of both isotopes are optically pumped to the state $|F = 2, m_F = 2\rangle$.

After optical pumping, the cloud is captured in the magnetic quadrupole trap produced by the same pair of coils used for the 3D MOT. The atoms are trapped with a gradient of $B'_z = 50$ G/cm (along the vertical direction). Subsequently, the trap gradient is reduced to 20 G/cm to only support the stretched state $|F = 2, m_F = 2\rangle$ of both isotopes against gravity. A pictorial representation of the spin purification scheme is presented in Fig. 4.5 (top panel). We find that this process is crucial to avoid inelastic collisions and spin relaxation during the RF-evaporation.

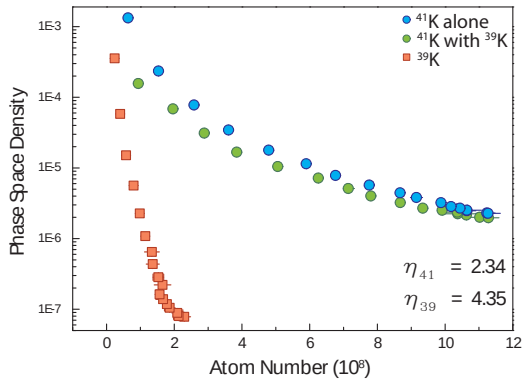

Figure 4.6: Phase-space density (PSD) in the magnetic quadrupole trap. Different PSD are presented: ^{41}K alone (blue dots), ^{41}K - ^{39}K optimal ratio (green dots - red squares). Although for ^{39}K a factor of ten in atom number is lost during the RF-evaporation, its PSD increases several orders of magnitude. The PSD of ^{41}K is slightly modified in the presence of ^{39}K.

Fig. 4.5 shows for comparison the effects of the spin purification with (left panel) and without (right panel) Zeeman pumping. In the left panel (no Zeeman pumping) the atoms with lower magnetic moment escape from the trap at a critical magnetic gradient B'_c. Only the atoms in spin $|F = 2, m_F = 2\rangle$ remain trapped. In the right panel (with Zeeman pumping on the D1 transition) we do not observe a pronounced change in the atom number as a function of magnetic field. The latter implies that our optical pumping procedure pumps nearly 100 % of the atoms to the right spin state. Similar results are found for ^{39}K. It is interesting to remark that in our experiment we initially performed optical pumping in the D2-line and only $\sim$ 85 % of the atoms were transferred to the right spin state for both cases. This is nearly the value obtained in the absence of the Zeeman pumping ($\sim$ 80 %).

4.2.2 *RF Evaporation*

After spin purification, the trap is recompressed back to $B'_z = 105$ G/cm, increasing the elastic collision rate. At this point, we start the radio-frequency evaporative cooling of ^{41}K. In particular we use the hyperfine transition from $|F = 2, m_F = 2\rangle$ (low field seeker) to $|F = 1, m_F = 1\rangle$ (high field seeker). The large and different ground state hyperfine splitting of the three isotopes allows evaporating only ^{41}K.

The RF signal is generated with the top antenna, located at ~ 25 mm from the atoms. During 10 s an exponential frequency sweep from 365 MHz to 265 MHz lowers the temperature of ^{41}K. Due to the background scattering length of the mixture ^{41}K-^{39}K (177 a_0), ^{39}K is cooled down by sympathetic cooling.

The evolution in phase-space density (PSD) is shown in Fig. 4.6 for three different situations: ^{41}K alone (blue circles), ^{41}K-^{39}K optimal ratio (green-orange). In dual-operation, we observe an increase in the phase space density of ^{39}K by four orders of magnitude. The optimal ratio in such configuration is $\sim$ 4:1 of ^{41}K with respect to ^{39}K. The evaporation efficiency is usually represented as $\eta = \frac{\partial(ln(PSD))}{\partial(ln(N))}$, where N represents the total atom number. In our situation this yields efficiencies of $\eta = 2.34$ for ^{41}K alone and $\eta = 4.35$[5] for the sympathetic cooling of ^{39}K with the optimal ratio. The ^{41}K efficiency is slightly modified in the presence of ^{39}K (< 10%).

In single operation, the typical atom number at the end of this stage is $\sim 6 \times 10^7$ at 25 μK. In the sympathetic cooling scheme, 2.5×10^7 of ^{39}K and 4×10^7 of ^{41}K are measured with a slight increase in temperature of 30 μK. The latter corresponds to a phase space density of $\sim 10^{-4}$. We stop the evaporation at this point due to Majorana losses and a subsequent decrease in the evaporation efficiency.

5 The efficiency η is computed for each isotope, here $N = N_{^{41}\mathrm{K}}$ or $N = N_{^{39}\mathrm{K}}$.

Conclusion. The favorable increase in PSD of ^{39}K is a proof of concept of sympathetic cooling by using ^{41}K as a cooler. The mixture ^{40}K-^{41}K ($\sim$ 97 a_0 background scattering length) presents similar properties [79]. In our experimental approach, achieving condensation in the magnetic quadrupole trap is not possible due to Majorana spin flips. Moreover, ^{39}K has an attractive background scattering that needs to be tuned *via* a Feshbach resonance to achieve condensation. These two problems are circumvented in our experimental setup by transferring the atoms to fully optical traps.

4.2.3 *Hybrid trap*

After magnetic evaporation, the final route to the quantum degenerate regime of the clouds is achieved in two different stages. First, the atoms are transferred from the quadrupole trap to a combined magnetic and optical trap. In this hybrid trap [112] an off-axis beam focused below the minimum of the quadrupole trap provides the transversal confinement while the longitudinal confinement is mainly given by a weak curvature of the magnetic field B. This technique offers large loading-volume avoiding the use of high power lasers. After some evaporation time in the hybrid trap, the magnetic gradient is removed adiabatically, and the atoms are transferred to a purely crossed optical trap. This opens up the possibility to control the interactions of the different isotopes by using the different Feshbach resonances available in the system. On this second step, the atoms are evaporated until condensation.

Hybrid trap. In our scheme, the atoms are transferred from the magnetic trap to a far-detuned optical trap. This dipole trap (aligned on the "W-axis"[6]) consist of a 7 W single YAG beam (1064 nm) that is focused to a waist of $w_0 = 65\mu$m below the magnetic field zero of the

6 see section 3.3.5 for axis convention

quadrupole field (see Fig. 4.7 (a)). This gives an optical trap depth of $\sim 130\ \mu$K as shown in Fig.4.7 (b).

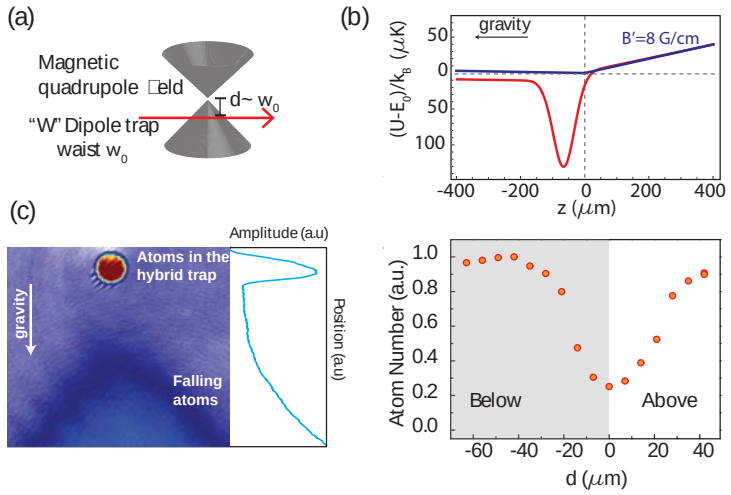

Figure 4.7: Hybrid trap. (a) The transversal confinement is given by a single dipole trap. The atomic scattering rate here is limited by the weak longitudinal confinement provided by the coils ($\sim$ 12 Hz). (b) The initial trap depth is $\sim 130\mu$K. The transfer to the atomic cloud is limited by the volume of the optical dipole trap (ODT). (c) (left panel) The gravitational sag due to the decompression of the magnetic trap allows transferring the atoms to the ODT. (right panel) The optimal value is approximately one waist below the zero of the quadrupole field

By decompressing adiabatically the B-field gradient from 105 G/cm to 8 G/cm, the gravitational sag allows capturing the atoms. The final value of the magnetic gradient is just above the minimum value required to levitate both ^{41}K and ^{39}K in state $|F = 2, m_F = 2\rangle$ against gravity.

We display in Fig. 4.7 (c) the normalized maximum transfer from the quadrupole field to the dipole trap as a function of the optimal position of the optical dipole trap beam after magnetic decompression. The value that maximizes the atomic cloud transfer to the ODT is off-centered approximately one waist from the zero of the quadrupole field. Either above or below the zero of the quadrupole the transfer

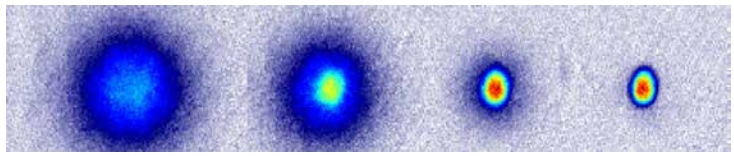

Figure 4.8: The first BEC in our apparatus was observed in June 2015. Here we present the momentum distribution after time-of-flight. From left to right the system goes from a thermal gas to a quantum degenerate gas. The atom number in the pure BEC phase was 2 x 10^4. This first BEC was achieved in the hybrid trap.

and the evaporation is similar. At the optimal position ($\sim$ 65 μm) the curvature of the magnetic field provides a longitudinal trap frequency close to 12 Hz. In optimal configuration around 15 % of the total atom number is transferred to the hybrid trap with typical temperatures of 9 μK.

We then perform forced evaporation. The power of the "W-beam" is reduced by rotating a half-wave plate in front of a polarization beam splitter (PBS). The intensity of the beam is additionally controlled with a PID connected to an AOM (see section 3.3.5). This technique reduces the optical potential while recycling the total power of our laser source for other dipole trap beams. The initial dipole trap depth is decreased by a factor of five in 3 seconds. After evaporation in the hybrid trap, the atoms are transferred to a crossed optical dipole trap where the interactions between the atoms can be controlled. The evaporation is optimized by increasing the initial PSD in the crossed optical dipole trap.

Note. In single-species operation (only ^{41}K) and by further decreasing the optical power of the "W-beam", quantum degeneracy was achieved. At T $\sim$ 300 nK, a bimodal distribution in the time-of-flight (ToF) absorption images appeared. By further evaporation, a nearly pure Bose-Einstein condensate with N = 20,000 atoms of ^{41}K was observed. This is shown in Fig. 4.8.

4.2.4 *Crossed optical dipole trap*

Crossed optical dipole trap. This trap is formed by crossing an additional far detuned vertical beam on the "Z-axis" derived from the same laser source as the "W-beam" (see section 3.3.5). The "Z-beam" waist is 150 μm and it has 3 W of power. As a result, the trap frequencies at the beginning of the evaporation are $\omega \approx 2\pi$ (300,300,145) Hz. The transfer from the hybrid trap is as follows: At the end of the hybrid evaporation, the vertical beam is ramped up to the maximum power in 500 ms, then the remaining weak magnetic gradient is ramped down to zero in 1 s. Because the trapping volume of the crossed optical dipole trap is considerably smaller compared to the hybrid trap, not all the atoms are trapped. Nevertheless, the presence of the additional vertical beam increases the PSD to 1×10^{-2}. Typical values at the beginning of this stage are around 1.5×10^6 at 1 μK in single isotope operation. In dual-operation, we measure similar temperatures with only half of this atom number for each isotope.

Internal state preparation

Before the last evaporation sequence, the Bitter coils are switched from anti-Helmholtz to Helmholtz configuration as presented in section 3.3.3. Subsequently, both isotopes are prepared in states where, either in single or dual-isotope operation, condensation is possible. In particular, they are prepared to exploit the tunability of the intra-species scattering length of ^{39}K.

At low magnetic field ($\sim$ 5 G) and using the W- coils, we sweep a 465 MHz and 270MHz radio frequency ramp to transfer ^{39}K and ^{41}K respectively to the state $|F = 1, m_F = 1\rangle + |F = 1, m_F = 1\rangle$. This is the lowest Zeeman state of the mixture and therefore is stable against two-body inelastic collisions. Subsequently, we ramp up the Feshbach field to $\sim$ 51.6 G where a series of Landau-Zener sweeps in magnetic field are done in both isotopes depending on the experiment required.

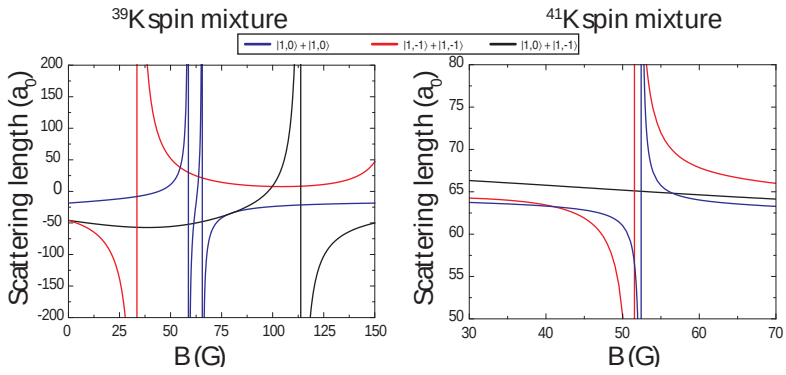

Figure 4.9: Feshbach resonances in ^{39}K and ^{41}K for the different channels in the ground state manifold F=1 (calculations from A. Simoni). Due to the presence of various Feshbach resonances, the transfers from the ground state $|F = 1, m_F = 1\rangle$ + $|F = 1, m_F = 1\rangle$ to the final state must be performed in the proper magnetic field range in order to minimize losses.

During the preparation of the final state, it is important to take care about the order of the Zeeman transfers to prepare at any moment the lowest energy state of the mixture.

Feshbach resonances in ^{39}K and ^{41}K

We choose this magnetic field window due to the presence of different Feshbach resonances that allow condensing ^{39}K and also perform the droplet experiments presented in chapter 6. The multiple Feshbach resonances for ^{39}K and ^{41}K are shown in Fig. 4.9.

d-wave shape resonance of ^{41}K

During the preparation of the different internal states of the system, we have observed by coincidence in $|F = 1, m_F = 1\rangle$ of ^{41}K two broad loss features centered at $\sim$ 17 G.

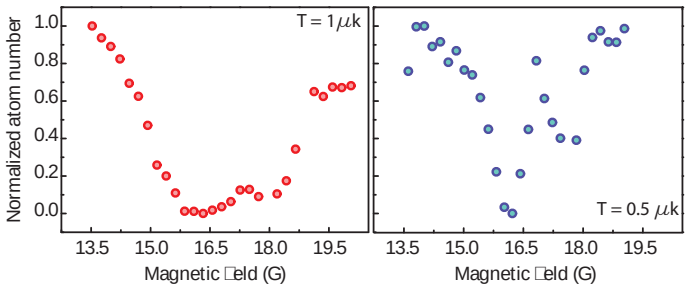

Figure 4.10: Due to inelastic losses we observe a loss feature at around $\sim$ 17 G in the internal states $|F = 1, m_F = 1\rangle$ of ^{41}K. It is attributed to a d-wave shape resonance [113].

We measure the dependence of the loss feature as a function of the temperature of the cloud using loss spectroscopy (see details of this technique in chapter 5) . In Fig. 4.10 we report our observations. We observe that at low temperatures (right panel) the feature becomes narrower. In fact a second peak appears at $\sim$ 17.5 G.

Different models including s- or p-wave resonances do not predict such feature. Interestingly in a recent publication [113] a detailed analysis is performed in the same vicinity of magnetic field for ^{41}K. They concluded that this feature is due to a high partial wave resonance. In particular, they associate it to a d-wave shape resonance.

4.3 QUANTUM DEGENERATE GASES OF POTASSIUM

Once we prepare the system in the correct spin configuration, three possible options are possible:

- Bose-Einstein condensation of ^{39}K.
- Bose-Einstein condensation of ^{41}K.
- Dual-Bose-Einstein condensation of ^{39}K-^{41}K.

In all of them, the production of a degenerate gas is possible with minor changes in the final evaporation ramp. They are explained in detail in the following section.

4.3.1 *Bose-Einstein condensation of ^{39}K and ^{41}K*

- **Bose-Einstein condensation of ^{39}K**. The isotopic mixture ^{39}K-^{41}K is prepared in state $|F = 1, m_F = -1\rangle$ and state $|F = 2, m_F = -2\rangle$ respectively. Due to the opposite magnetic moments at the Feshbach field, we can employ during the evaporation a spin distillation scheme to remove, if required, one of the isotopes.

  In the final evaporation ramp, the trap depth of the "W beam" is reduced in 1.5 seconds while tuning the scattering length of ^{39}K to 180 a_0 (B $\sim$ 39 G). During the time of evaporation, a magnetic gradient of 20 G/cm is applied with the jump coils to remove ^{41}K.

  The bimodal distribution, signature of the thermal gas to BEC phase transition is shown in Fig. 4.11 (right panel). It is observed after absorption imaging in time of flight at zero field. Before turning off the magnetic fields, the first 10 ms of ToF take place at the condensation field. Once the cloud is dilute enough the magnetic field is switched off, and 10 ms of ToF are performed. Because of the high densities of the ^{39}K condensate, this procedure is required in order to cross the $|F = 1, m_F = -1\rangle$+$|F = 1, m_F = -1\rangle$ resonance (see Fig. 4.9) without loss of atoms due to three-body recombination or molecule formation.

- **Bose-Einstein condensation of ^{41}K** is achieved with the same evaporation ramps as ^{39}K. The positive background scattering length ($\sim$ 60 a_0) at zero field allows condensing the system in any spin configuration. The use of Feshbach resonances is not needed, and therefore the experiment is performed using a small bias-field to avoid spin-depolarization. If ^{39}K is initially not loaded,

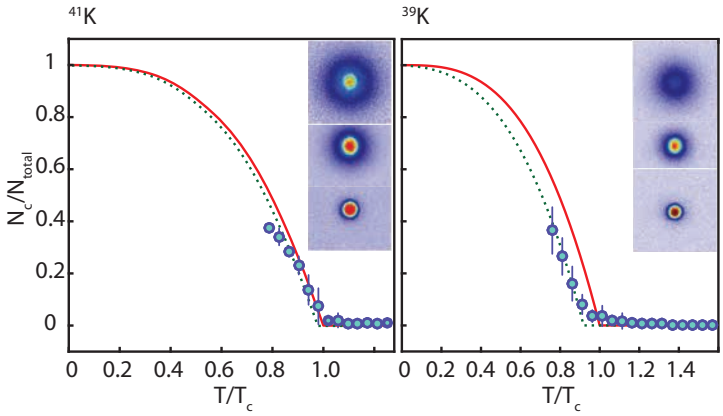

Figure 4.11: Bose-Einstein condensation of ^{41}K (left panel) and ^{39}K (right panel). We perform the experiments with ^{41}K in the state $|F = 1, m_F = 1\rangle$. Here the system is robust against spin exchange collisions. For ^{39}K experiments, we prepare the system in $|F = 1, m_F = -1\rangle$ where we can control the interactions between the atom *via* a Feshbach resonance. In both cases the solid red line and the dotted blue line correspond to the condensate fraction of a non-interacting and interacting condensate respectively.

the initial conditions in the crossed optical dipole trap are ~ 1 μK with $\sim 1.5 \times 10^6$. With these values, the PSD doubles compared with the dual-operation. Similar to ^{39}K condensates, the bimodal distribution and phase transition is shown in Fig. 4.11 (left panel).

The critical temperature T_c where condensation occurs in both cases is sketched in Fig. 4.11. We compare our results to the theoretical T_c^0 curve (solid red line) of a non-interacting BEC (see chapter 2). In both plots, the measured temperature is normalized to the transition temperature T_0 of an ideal bosonic gas with harmonic confinement. As expected for an interacting condensate we observe that the measured T_c is slightly lower. Due to the small gas parameter of the system, we neglect shifts in critical temperaure given by beyond-mean-field effects [114].

	Potassium condensates	Evaporation cooling technique	Atom number	Ref.
LENS (Italy)	^{41}K	Sympathetic cooling ^{87}Rb - ^{41}K	1×10^4	[72]
HFN (China)	^{41}K	Magnetic trap followed by ODT	1.2×10^6	[85]
IEI (Japan)	^{41}K	Magnetic trap followed by ODT	3×10^5	[78]
MIT (US)	^{41}K	Optically plugged magnetic trap	3×10^5	[75]
IOGS (France)	^{39}K	All optical	3×10^5*	[90]
LENS (Italy)	^{39}K	Magnetic trap followed by ODT	8×10^5	[115]
LENS (Italy)	^{39}K	Sympathetic cooling ^{87}Rb - ^{39}K	3×10^4	[116]
Cavendish Lab (UK)	^{39}K	Sympathetic cooling ^{87}Rb - ^{39}K	4×10^5	[88]
IFA (Denmark)	^{39}K	Sympathetic cooling ^{87}Rb - ^{39}K	3×10^5*	[55]

Table 4.2: Bose-Einstein condensates of potassium reported in the literature. The symbol "*" means the literature does not report this value explicitly.

The shift in T_c for ^{39}K and ^{41}K is due to the different intra-species scattering length used during the last optical evaporation. We remind the reader that we use this measurement to calibrate the atom number in our experiment.

At the end of the evaporation, a pure condensate of ^{39}K is observed with nearly 3.5×10^5 atoms. For ^{41}K we obtained condensates of $\sim 5 \times 10^5$ atoms. The condensation of ^{39}K by using ^{41}K as a coolant validates our new experimental approach.

Comparison to other experiments

Potassium experiments have been developed around the world using different approaches. Different techniques have been used such as: sympathetic cooling, all optical or combination of magnetic traps followed by optical traps. Here we summarize only the different potassium BECs published in peer-reviewed journals.

For comparison, both ^{41}K BEC and ^{39}K BEC have atom numbers similar to the ones presented in Table 4.2. In particular, the sympathetic cooling of ^{39}K using ^{41}K as a coolant obtains similar results as the experiments using ^{87}Rb, however here we have simplified the experimental setup by only dealing with different isotopes. We do not need different laser systems; instead, we can share the same laser sources.

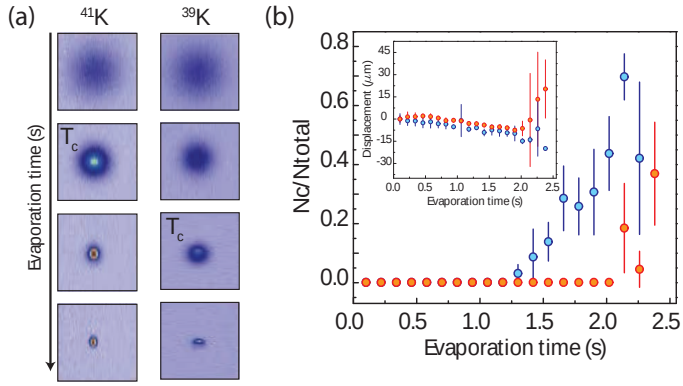

Figure 4.12: Dual-BEC of ^{39}K- ^{41}K. (a) Bose-Einstein condensation is observed after ToF. On each experimental sequence, both absorption images are taken in independent axes and CCD cameras simultaneously. Due to the large frequency difference between the imaging transitions, we do not observe crosstalk in the measurements. The system phase separates due to the difference in intra an inter-species scattering lengths. (b) At the beginning of the evaporation, both isotopes have similar atom numbers; however, due to the differences in scattering length of each isotope, they cross T_c at different moments in time. After crossing T_c the center of mass of the two isotopes is displaced differently due to phase separation (see inset).

Moreover, the vacuum system operates with one single atomic source. This means that we only need one single 2D MOT/ Zeeman slower. Finally the length of our experimental sequence is considerably shorter compared to Rb-K experiments.

In contrast to all optical experiments, we do not require high power lasers.

4.3.2 *Dual-Bose-Einstein condensation of ^{39}K–^{41}K*

In this section, we present the creation of, to our knowledge, the first quantum degenerate mixture of the two bosonic isotopes of potassium. The **dual-BEC of ^{39}K-^{41}K** is obtained by preparing the mixture into states $|F = 1, m_F = -1\rangle + |F = 1, m_F = -1\rangle$ at the same magnetic field used for condensation of ^{39}K. We have observed that both isotopes

need to be in the same spin state otherwise any residual magnetic field gradient evaporates in an uncontrolled manner one of the isotopes during the evaporation.

In the vicinity of this magnetic field, the scattering length of ^{39}K can be tuned to a_{39}= 150 a_0 while keeping the inter-species ^{39}K-^{41}K interaction
(a_{39-41}= 170 a_0) and intra-species ^{41}K interaction (a_{41}= 60 a_0) constant.

Using similar evaporation ramps, after two seconds of evaporation we produce a dual-BEC of ^{39}K- ^{41}K with $\sim 5 \times 10^4$ atoms on each isotope. This is observed after ToF (see Fig. 4.12 (a)). As expected, due to the intra- and inter- species scattering length of the mixture at this magnetic field, the system is in the immiscible phase.

Thus the repulsive interactions between the two isotopes is large enough that the ground state energy of the system is minimized by phase separating the two components (see Fig.4.12 (a)).

The inset in Fig. 4.12 (b) shows the center of mass evolution after ToF as a function of the evaporation time. Even though both isotopes have similar mass, the small gravitational sag breaks the symmetry between them making ^{39}K (orange dots) go upwards compared to ^{41}K (blue dots).

In Fig. 4.12 (b), the condensed fraction N_c of ^{39}K (orange dots) and ^{41}K (blue dots) is shown as a function of the evaporation time. Both systems condense in a different timescale due to the difference in the initial atom number and intra-species scattering length.

Remarks. During the dual-evaporation, a large shot-to-shot fluctuation in the atom number of the condensates is observed. A possible explanation could be that both isotopes do not cross T_c at the same time and therefore more complicated thermalization takes place. In fact, given the intra- and inter- species scattering length of the mixture, the system is in a strongly immiscible phase. Therefore the characteristic bimodal distribution of a BEC is displaced above (^{39}K) and below (^{41}K) with respect to the center of the thermal clouds just after crossing T_c. Due to the shift of the center of mass of the clouds, the

thermalizacion process on each isotope is no longer spatially homogeneous and different parts of the cloud experience different inter- and intra- species scattering events. The thermalization process during the production of a dual-BEC in the immiscible phase has been studied previously in ref. [117].

Note. For this particular spin state and magnetic field, we have tuned the inter-species scattering length of ^{39}K to values above 600 a_0 in order to be in the miscible phase. However, at such large scattering length the two and three body losses are enhanced and therefore the lifetime of the gas is reduced.

This chapter describes the first Bose-Einstein condensate in Spain. This marked the beginning of very exciting experiments in our lab!!!

5

FESHBACH SPECTROSCOPY OF POTASSIUM BOSE-BOSE MIXTURES

5.1 INTRODUCTION

After the achievment of our first dual BEC of the two bosonic potassium isotopes, we have characterized the scattering properties of this mixture. In this chapter, we report on the observation of 20 previously unobserved resonances in a ^{39}K–^{41}K system. We measure the position of the resonances by loss spectroscopy and perform a consistent assignment to molecular levels using an asymptotic bound-state model [118, 119]. Coupled-channel calculations are then employed to perform a full analysis of the width and position of the resonances, using the available model potentials for potassium scattering [120].

Additionally, Feshbach resonances are studied in spin mixtures of a single potassium isotope both in ^{41}K and ^{39}K. In the latter we characterize the resonance parameters by radio-frequency association of Feshbach molecules, giving a precise determination of the scattering length.

5.2 FESHBACH LOSS SPECTROSCOPY

Feshbach loss spectroscopy is a powerful tool to locate the position of Feshbach resonances experimentally. It consists on the observation of the atom number decay (atomic losses) due to the enhancement of inelastic losses close to the resonance. The low temperatures of the atomic clouds (temperatures below a few micro-Kelvin) increase the visibility of the loss feature and in particular *s-wave* Feshbach resonances are enhanced while high order partial waves are suppressed.

5.3 FESHBACH RESONANCES IN POTASSIUM MIXTURES

5.3.1 *Experimental preparation*

Our experiments are performed with ultra-cold clouds prepared in a crossed optical dipole trap and subjected to a homogeneous magnetic field in the range of $10 - 650$ G. The clouds are prepared by using the experimental sequence presented in chapter 4, however during the last stage of evaporation we do not cross the critical temperature T_c.

All experiments reported in this chapter are performed in a crossed beam optical dipole trap with trap frequency $\omega/2\pi = (67, 163, 176) \pm 5$ Hz. The initial atom number corresponds to $\sim 10^5$ atoms of both isotopes and a temperature of ~ 420 nK. Under these conditions, this results in $T/T_c \simeq 10$.

5.3.2 *Feshbach spectroscopy in ^{39}K-^{41}K mixtures*

In a first series of experiments, we locate Feshbach resonances in the ^{39}K–^{41}K mixture. This atomic combination has not been studied experimentally before. Therefore, and in order to provide sufficient data for a complete characterization of the inter-isotope interaction potentials, we explore scattering channels corresponding to all $M_F = m_F^{39} + m_F^{41}$ values where the mixture is in the lowest state of energy. The latter ensures that we will observe the decay in atom number only due to three-body losses and not due to spin exchange relaxation.

The different spin state combinations are prepared using Landau-Zener radio-frequency (RF) sweeps. Feshbach spectroscopy is then performed by ramping the magnetic field to the desired value and measuring simultaneously the atom number of ^{39}K and ^{41}K after a variable hold time. This is adjusted empirically in order to optimize the experimental signal. As explained before, a resonance manifests itself as an enhancement of atomic losses and the corresponding increase of temperature. Typical data is presented in Fig. 5.1 (a), where for a given

Entrance channel	M_F	B_0^{exp} [G]	B_0^{ABM} [G]	$\delta\mu$ [μ_B]	B_0^{CC} [G]	Δ^{CC} [G]	$a_{\mathrm{bg}}^{\mathrm{CC}}$ [a_0]
$^{39}\mathrm{K}\vert 1,1\rangle$+$^{41}\mathrm{K}\vert 2,2\rangle$	3	341.5(2)	340.608	1.56	341.619	0.138	135.2
	3	353.8(3)	351.706	1.26	354.010	0.493	135.2
$^{39}\mathrm{K}\vert 1,1\rangle$+$^{41}\mathrm{K}\vert 1,1\rangle$	2	139.27(4)	139.122	-2.97	139.400	0.0374	173.0
	2	146.24(7)	146.011	-2.45	146.411	0.111	173.0
	2	338.12(7)	337.758	-1.95	338.281	0.0461	176.4
	2	500.2(3)	495.592	-0.73	500.049	0.700	176.1
	2	518.4(1)	516.038	-1.56	518.433	0.128	176.1
$^{39}\mathrm{K}\vert 1,1\rangle$+$^{41}\mathrm{K}\vert 1,0\rangle$	1	88.2(1)	68.898	0.02	88.475	0.0258	168.4
	1	160.05(6)	159.805	-2.62	160.128	0.0474	172.5
	1	165.80(5)	165.409	-2.23	165.933	0.110	172.5
	1	344.4(1)	343.864	-1.93	344.509	0.128	176.2
	1	522.6(2)	518.198	-0.78	522.478	0.621	176.0
	1	553.1(1)	550.218	-1.30	552.964	0.198	176.0
$^{39}\mathrm{K}\vert 1,1\rangle$+$^{41}\mathrm{K}\vert 1,-1\rangle$	0	189.88(5)	189.343	-2.97	189.999	0.0766	172.6
	0	348.4(1)	347.567	-1.92	348.463	0.180	176.2
	0	384.91(7)	384.631	-1.92	385.073	0.0635	175.4
	0	553.5(2)	549.759	-0.94	553.378	0.506	176.1
$^{39}\mathrm{K}\vert 1,0\rangle$+$^{41}\mathrm{K}\vert 1,-1\rangle$	-1	228.88(8)	228.256	-0.88	229.039	0.989	171.8
$^{39}\mathrm{K}\vert 1,-1\rangle$+$^{41}\mathrm{K}\vert 1,-1\rangle$	-2	149.84(6)	145.561	0.07	149.764	-0.0252	163.7
$^{39}\mathrm{K}\vert 1,-1\rangle$+$^{41}\mathrm{K}\vert 2,-2\rangle$	-3	649.6(6)	645.937	-1.00	649.167	0.673	176.2

Table 5.1: Summary of the Feshbach resonances between ^{39}K and ^{41}K observed in this mixture. The experimental positions are determined from Gaussian fits to the measured loss features. Their uncertainty corresponds to the $1/e^2$ half-width of the Gaussian fit. B_0^{ABM} and $\delta\mu$ denote the theoretical predictions of the asymptotic bound-state model for the resonance positions and difference in magnetic moments for the open and close channels. B_0^{CC}, Δ^{CC} and $a_{\mathrm{bg}}^{\mathrm{CC}}$ are the results of a coupled-channel calculation using the model potentials of ref. [120].

magnetic field, the atom number decays while the temperature of the systems increases.

We find a total of 20 loss features within the range $88 - 650$ G, which are summarized in Table 5.1. Since all observed features are narrow in magnetic field (between 10 mG and 100 mG), we identify the position of the resonance with the center of the loss curve. For all the measurements the magnetic field is calibrated to a precision of 10 mG using radio-frequency transitions between Zeeman sublevels in the vicinity of each of the resonances.

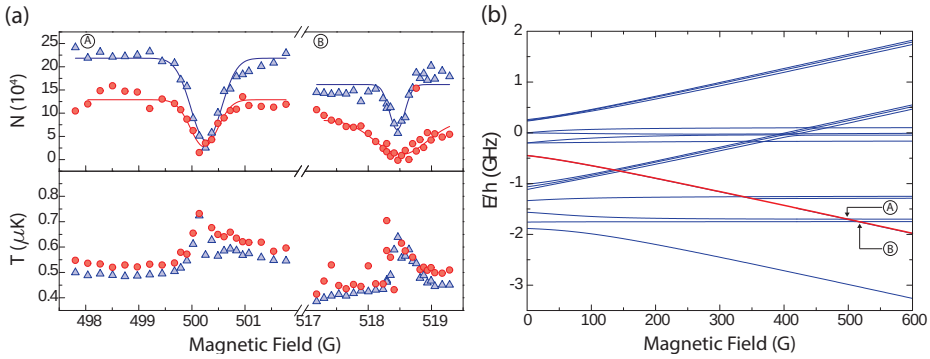

Figure 5.1: Feshbach resonances for $^{39}K|1,1\rangle+^{41}K|1,1\rangle$ collisions. (a) Top and bottom panel denote typical data of experimentally measured resonances. Here we present two inter-isotope Feshbach resonance: one at $\sim$ 500 G and the other one at $\sim$ 518.5 G. The loss in atom number (top panel) comes with an increase of temperature of the clouds (bottom panel). The blue and red colors represent the measurements in ^{41}K and ^{39}K respectively. The solid lines represent a Gaussian fit. (b) Results of the ABM model ^{41}K-^{39}K mixture. In red, open-channel threshold energy. In blue, uncoupled $s-$wave molecular state energies. The crossing between the red and blue lines is where a Feshbach resonance appears. The A and B letters make reference to the Feshbach resonances presented in (a).

5.4 THEORETICAL ASSIGNMENT OF FESHBACH RESONANCES IN POTASSIUM

The Feshbach resonances reported in Table 5.1 might provide the opportunity to improve the model potentials used to predict the potassium scattering properties. We compare our results with the predictions of two different theoretical models: The coupled channel (CC) method [121] and the asymptotic-bound-state model (ABM) [118, 119].

On the one hand, the coupled channel calculation makes a quantitative prediction of the properties of a resonance. Here the Schrödinger equation associated to the full Hamiltonian that describes the collision of an atomic pair is solved numerically. In order to obtain precise results, this requires a good knowledge of the two body potential (the single and triplet part). This calculation was performed by M. Tomza.

On the other hand, the asymptotic-bound-state model (ABM) is a method that allows predicting the position of Feshbach resonances in a simpler way[1]. The main idea of this model consists on finding at which magnetic field the closed-channel bound-state energy will intersect the energy of the free atom pair. This is sketched in Fig. 2.2 (b). Usually, the required ingredient is the zero-field energy offset E_b of the closed-channel bound-states with respect to the energy of the free atom pair. This depends on the details of the potential of the atomic pair.

5.4.1 *The asymptotic-bound-state model for potassium mixtures*

The model is explained in detail in ref. [118, 119, 122] and has been adapted to ^{39}K-^{40}K-^{41}K resonances. This calculation was performed in the group by L. Tanzi. We have employed this model to have a first assignment of the observed Feshbach resonances and identify the molecular channels responsible for them. In order to reproduce all of the observed loss features, the two last vibrational states of both potentials need to be taken into account. The corresponding energies and Franck-Condon factors are $E_S^1/h = -32.1$ MHz, $E_T^1/h = -8.33$ MHz, $E_S^2/h = -1698.1$ MHz, $E_T^2/h = -1282.5$ MHz, $\eta_{11} = 0.9180$, $\eta_{22} = 0.9674$, $\eta_{12} = 0.0895$ and $\eta_{21} = 0.0463$. Here $S(T)$ denotes a singlet (triplet) bound state, vv' (with $v(v') = 1, 2$) the overlap between the singlet and triplet wavefunctions in the vibrational state v and v' respectively.

In Fig. 5.1 (b) we show an example of our calculation. The blue lines represent the energy of the molecular states as a function of magnetic field in the mixture $^{39}\text{K}|1,1\rangle + ^{41}\text{K}|1,1\rangle$. The red line depicts the energy of a free atom pair. The crossing between these lines gives rise to a Feshbach resonance. We confirm our predictions experimentally, the

1 The ABM model is a good starting point to locate Feshbach resonances theoretically in different systems, however it is not as precise as the CC calculation.

two crossing points depicted as A and B at around 500 G correspond to the loss features sketched in Fig. 5.1 (a).

5.4.2 *The coupled-channel calculation*

A more accurate description of the scattering properties of the ^{39}K–^{41}K system is obtained by performing a coupled-channel (CC) calculation using the model potentials of potassium from [120]. We neglect the spin-dipole-spin-dipole interaction and second-order spin-orbit coupling responsible for the dipolar relaxation, which are expected to have a negligible effect on the *s*-wave resonances (except in the case of overlapping higher partial wave resonances). The coupled-channel equations are solved as in refs.[123, 124], assuming a temperature of 100 nK in all calculations. The resonance position B_0, the resonance width Δ, and the local background scattering length a_{bg} are obtained by fitting the numerical points with the analytical expression

$$a(B) = a_{\mathrm{bg}} + a_{\mathrm{res}} = a_{\mathrm{bg}} \left(1 - \frac{\Delta}{B - B_0}\right). \tag{5.1}$$

For two overlapping Feshbach resonances we use instead the more general expression [125]

$$a(B) = a_{\mathrm{bg}} \left(1 - \frac{\Delta_1}{B - B_{0,1}}\right) \left(1 - \frac{\Delta_2}{B - B_{0,2}}\right), \tag{5.2}$$

where the $i = 1, 2$ denote each of the resonances.

The results of the CC calculation are summarized in table 5.1. By quantifying the agreement with the experimental data through $\delta = B_0^{\mathrm{exp}} - B_0^{\mathrm{CC}}$. Given the accuracy of our data, our measurements could be used to construct improved scattering potentials for potassium. Furthermore the use of an isotopic mixture could be used to verify the validity of the Born-Oppenheimer approximation made to derive the model potentials.

5.5 ^{41}K SPIN MIXTURE

In a second series of experiments we study spin mixtures of ^{41}K. We locate a new Feshbach resonance in the $|1,0\rangle + |1,-1\rangle$ channel, in the vicinity of 51.92 G, close to the single-component resonance $|1,-1\rangle + |1,-1\rangle$ (51.14 G) reported in ref. [126]. This situation provides good control over both the inter- and intra-state scattering lengths, and makes ^{41}K an interesting system for the study of two-component Bose gases with repulsive intra-state interactions, and tunable inter-state ones. This situation can lead to the formation of quantum droplets, as those studied in chapter 6 and 7.

Fig.5.2 displays the measured loss features, together with the relevant inter and intra-state scattering lengths predicted by our CC model. We find good agreement between experiment and CC calculations when the mass-scaled model potentials of ref. [120] are employed.

5.6 ^{39}K SPIN MIXTURE

We perform a last series of experiments in a spin mixture of ^{39}K. This isotope has several broad single-component Feshbach resonances [127]. Recently, a resonance in the $|1,0\rangle + |1,-1\rangle$ channel, with a width $\Delta B \simeq 16$ G, was reported [128]. Since it is in a magnetic field range where the scattering length of $|1,-1\rangle$ is approximately constant and positive, it is very well adapted to the study of Bose-polaron physics using $|1,-1\rangle$ as bath and $|1,0\rangle$ as impurities. Such studies were performed by the Aarhus group [128]. In order to determine experimentally its parameters, we measure the binding energy of the Feshbach molecules. Combined with our coupled-channel model, this allows us to obtain accurate values of the resonance position, width and background scattering length.

Two different techniques are employed to measure the binding energy E_b. In the close vicinity of the resonance, we directly associate molecules starting from a $|1,0\rangle + |1,-1\rangle$ mixture and subjecting it to a

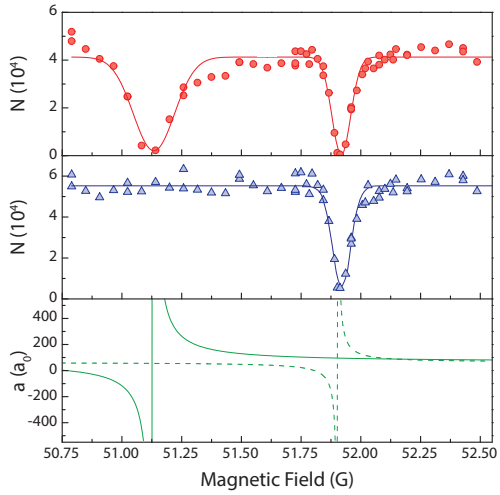

Figure 5.2: (Top and central panel.) Feshbach resonances in a $|1,-1\rangle + |1,0\rangle$ mixture of ^{41}K. The top panel present the loss features for $|1,-1\rangle + |1,-1\rangle$ while the central panel presents the losses in state $|1,0\rangle$. The bottom panel shows the scattering lengths predicted by our CC calculations for the single component resonance (solid line) and the spin mixture (dashed line).

modulated magnetic field of frequency corresponding to E_b [129, 130]. For larger binding energies, we exploit instead radio-frequency association [131]. Starting from the non-resonant state $|1,0\rangle$, we apply a radio-frequency pulse near the $|1,0\rangle$ to $|1,-1\rangle$ transition and transfer atoms to the bound state. In both cases, the formation of molecules is signalled by a reduction of the trapped atom number because the molecules decay due to vibrational quenching induced by collisions with unpaired atoms, and leave the trap. The top inset of Fig. 5.3 displays a typical radio-frequency spectrum. The association of molecules corresponds to the asymmetric feature, which reflects the fact that the association frequency depends on the kinetic energy of the atom pair forming the molecule. We model it by a convolution of a Maxwell-Boltzmann distribution and a Gaussian function (solid line) [132]. The latter results from the finite molecule lifetime, as well as technical

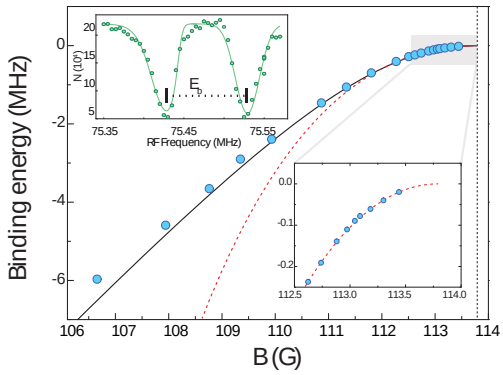

Figure 5.3: Binding energy of the molecular state in ^{39}K measured by radio-frequency spectroscopy. Red dashed line: Binding energy of a Feshbach molecule in the universal regime. Black solid line: CC prediction. (Top inset) Typical data for RF spectroscopy. The asymmetric peak represents the position of the molecular energy, the additional peak corresponds to the atomic hyperfine transition. The distance between the two features is the molecular binding energy E_b. (Bottom inset) Regime where the universal relation $E_b = -\hbar^2/ma^2$ is valid.

broadening. The binding energy here is given by the distance between the molecular peak and the additional peak that corresponds to the atomic hyperfine transition.

Fig. 5.3 summarizes the measured molecular binding energy as a function of the magnetic field. Near the resonance, it follows the universal relation $E_b = -\hbar^2/ma^2$. At larger detunings, finite range corrections become important and this simple expression loses its validity. In order to provide a model-independent parametrization of the scattering length we thus restrict ourselves to the range above ~ 112 G, where the non-universal corrections are negligible. The fit to the universal formula (red dashed line) yields $B_0 = 113.79(2)$ G for the resonance position, and $a_{bg}\Delta B/a_0 = 755(20)$ G for the product of the resonance width and background scattering length. The coupled-channel calculation (black solid line), on the other hand, provides a good description of our measurements in the complete magnetic field range.

5.7 CONCLUSIONS

In conclusion, in this chapter we have performed a comprehensive experimental and theoretical study of the low energy scattering properties of our new Bose-Bose mixture. Using the isotopic mixture ^{39}K–^{41}K we have confirmed the validity of the model potentials of ref. [120]. In addition we have explored spin mixtures of ^{39}K and ^{41}K.

Moreover, we have compared our ABM model predictions with a full CC calculation. Both approaches have been corroborated experimentally. The discrepancy between theory and experiments is in agreement within experimental error bars.

6

QUANTUM FLUIDS: FROM QUANTUM GASES TO QUANTUM LIQUIDS

Quantum droplets are small clusters of atoms self-bound by the balance of attractive and repulsive forces. Here we report on the observation of a novel type of droplets, solely stabilized by contact interactions in a mixture of two Bose-Einstein condensates. We demonstrate that they are several orders of magnitude more dilute than liquid helium by directly measuring their size and density via *in situ* imaging. Moreover, by comparison to a single-component condensate with only contact interactions, we show that quantum fluctuations stabilize them against collapse. We observe that droplets require a minimum atom number to be stable. Below, quantum pressure drives a liquid-to-gas transition that we map out as a function of interaction strength. These ultra-dilute isotropic liquids remain weakly interacting and constitute an ideal platform to benchmark quantum many-body theories.

This chapter is partially published in ref. [66].

C. R. Cabrera, L. Tanzi, J. Sanz, B. Naylor, P. Thomas, P. Cheiney, and L. Tarruell, Science **359**, 301 (2018).

6.1 INTRODUCTION

This chapter presents the first observation of quantum liquid droplets in a mixture of Bose-Einstein condensates. This new exotic phase of matter, predicted by D. Petrov [3] and observed first in dipolar systems and now in a mixture of alkali atoms [66, 67], exhibit properties of a liquid such as surface tension, surface excitations (ripplons) and the gas-to-liquid phase transition.

For a better understanding, this chapter is divided in two parts. In section 6.2 we first present the state-of-the-art in quantum liquids with ultra-cold quantum gases. Subsequently in section 6.2.2 we explain the theoretical background and the main mechanism responsible for giving rise to a quantum gas-to-liquid phase transition in a Bose-Bose mixture. We present in sections 6.2.3 and 6.2.4 the main properties of our quantum droplets such as excitation spectrum and density profile. We introduce the phase diagram of the system for the free space case as a function of the different experimental parameters. This phase diagram is investigated by performing a variational ansatz. Finally in section 6.3 we conclude the first part of this chapter by comparing the well known dipolar droplets with the composite droplets.

In the second part, we present in section 6.4 the experimental observation of this self-bound quantum liquid droplet state and its properties in our experimental apparatus. We characterize in sections 6.5 and 6.6 the quantum liquid-to-gas phase transition as a function of interaction strength and atom number in the condensates. We compare our results with the theory presented in the first part of this chapter.

Given the novelty of the system, different experimental groups have explored the formation of this self-bound state. We conclude in section 6.6.6 this chapter by discussing our results and the ones recently published from European Laboratory for Non-Linear Spectroscopy (LENS) group [67]. In both groups, we follow different experimental approaches, and therefore both publications complement each other in the understanding of this liquid phase.

6.2 QUANTUM FLUIDS

6.2.1 *State-of-the-art*

Quantum fluids can be liquids – of fixed volume – or gases, depending on the attractive or repulsive character of the inter-particle interactions and their interplay with quantum pressure. On the one hand, gases are dilute systems where attractive interactions are not enough to create a finite size system. Here the system has high compressibility and volume defined by the container. On the other hand, liquids are dense, and they exist when the **attractive** forces which hold the particles together equilibrate the **repulsive** ones that stabilize them against collapse. In such circumstances, the system acquires properties such as surface tension, fixed volume, and very low compressibility.

Two primary examples of quantum fluids are liquid helium (He) and Bose-Einstein condensates of ultra-cold atoms. Both systems exhibit similar properties such as superfluidity. However, an inherent property of a liquid not previously seen in BECs was the formation of droplets: a self-bound cluster of atoms with finite size.

In liquid He for example, such clusters are **self-bound states** that emerge from the compensation of attractive forces, associated to van der Waals interactions, and repulsive terms that stem from the overlap of the electronic wavefunction of the atom pair (Pauli exclusion principle). This picture is valid for most of the liquids that can be described using the van der Waals equation of state. In ultra-cold atoms, these "common" liquids are not possible due to the low density of the system. As explained in chapter 2, the interaction between atoms are effectively described using the s-wave scattering length a. Even though we can impose attractive interactions in the condensate *via* a Feshbach resonance, at the length scale imposed by the density of the system in the single component case no restoring force can prevent the system from collapse.

To circumvent the collapse of the condensate and create ultra-cold atomic droplets several stabilization mechanisms have been proposed so far, including either three-body correlations [133, 134], dynamical stabilization using Rabi oscillations between two states [135], or quantum fluctuations [3].

It has been shown recently that indeed quantum fluctuations can stabilize a two-component mixture with inter-component attraction and intra-component repulsion [66, 67, 136]. In contrast to He droplets, in this system, the repulsion stems from quantum fluctuations, which are a genuine quantum many-body effect, while the mean-field energy gives the attraction. Shortly before these experiments, similar droplets have been realized in magnetic quantum gases with attractive dipolar and repulsive contact interactions [137–142]. In this case, the anisotropic character of the magnetic dipole-dipole force leads to the formation of filament-like self-bound droplets with highly anisotropic properties [141, 143, 144].

6.2.2 *Stabilization mechanism of composite quantum droplets*

The formation of quantum droplets in ultra-cold atoms is due to the competition of repulsive beyond mean-field effects and attractive mean-field interactions. The original prediction proposed to use a Bose-Bose mixture in the regime where the collapse is predicted ($\delta g < 0$)[3]. Let us recast the simplest form of the energy density function of a homogeneous Bose-Bose mixture with equal masses presented in Eq. 2.61. This reads

$$\mathcal{E} = \overline{\eta} n_0^2(r)\delta a + \overline{\kappa} n_0^{5/2}(r) a^{5/2}, \tag{6.1}$$

where $\overline{\eta} = \frac{\pi\hbar^2}{m}$ and $\overline{\kappa} = \sqrt{\frac{\pi}{2}}\frac{64}{15m}\hbar^2 F\left(1, \frac{a_{\uparrow\downarrow}^2}{\overline{a}^2}, 1\right)$. Here $\overline{a} = a_{\uparrow\uparrow} = a_{\downarrow\downarrow}$. Notice that in comparison to chapter 2, here we express this equation using explicitly the scattering length a and the parameter δa. This allows to compare with the experimental results directly.

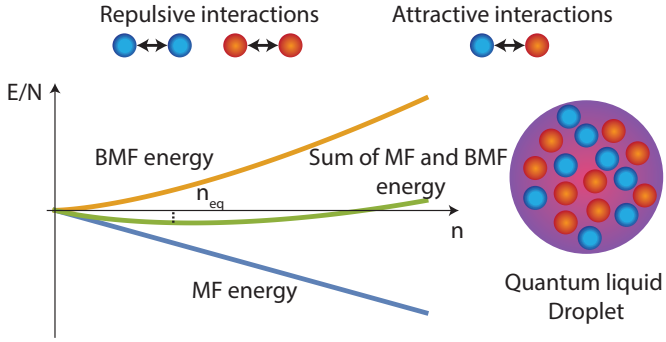

Figure 6.1: In a two-component BEC with competing interactions, it is possible to go in regimes where the MF energy is canceled and therefore beyond mean-field corrections are revealed. Strikingly, for a given density n_{eq} the competition of the mean-field (MF) and beyond mean-field (BMF) energy give rise to the formation of a self-bound quantum liquid droplet. Figure adapted from [145], notice the rescaling on the vertical axis E/N.

For $\delta a < 0$, the mixture is expected to collapse in the mean-field formalism. However, the collapse is avoided by the repulsive character of the BMF term. Due to the different density scaling of both terms, they compensate when

$$n_{\mathrm{eq}}^2 \propto \frac{|\delta a|}{a^{5/2}}. \tag{6.2}$$

A pictorial representation of the stabilization mechanism is shown in Fig. 6.1.

The following points are important to remark:

- For a given interaction strength given by δa and a, there is a fixed equilibrium density. Once n_{eq} is reached, increasing the atom number will only increase the size of the droplet, but the density remains constant. A flat top density profile is expected for large atom numbers [3] (see discussion section 6.2.3).

- The system has very low compressibility. It costs a large amount of energy to change the density of the liquid droplet.

- For typical experiments, this quantum liquid droplet is several orders of magnitude more dilute than He droplets.
- Unlike their dipolar counterparts, the equilibrium density n_{eq} depends only on *s*-wave contact interactions and the droplets are therefore isotropic (see discussion section 6.3).
- Finally, the fact that the density depends only on a and δa implies that the details of the potential are not required to describe the system.

6.2.3 *Properties of composite quantum droplets*

Density profile

In this section we discuss several aspects calculated by D. Petrov in his original proposal [3]. First the formation of a quantum droplet in the absence of any external potential is proposed. This droplet is stabilized in a system that is described only with s-wave contact interactions. Therefore it is isotropic in space.

For large atom number, once the equilibrium density n_{eq} has been reached, the system exhibits a flat-top density profile as depicted in red lines in the left panel of Fig. 6.2 (a). More atoms in the droplet increase its size however the bulk density remains constant. This is the regime of a uniform liquid. In the edges the density decreases exponentially, this represents the surface thickness. At this length scale the quantum pressure is not negligible with respect to the interaction energy terms. This thickness is usually defined as the length where the bulk density drops from 90 to 10% [146].

For low atom number, below the saturation density n_{eq}, the dilute self-bound droplet has a profile dominated by surface effects. This is appreciated in the dashed and solid lines in Fig. 6.2 (a). In this particular case, the droplet is mainly made of "surface." Finally for a critical

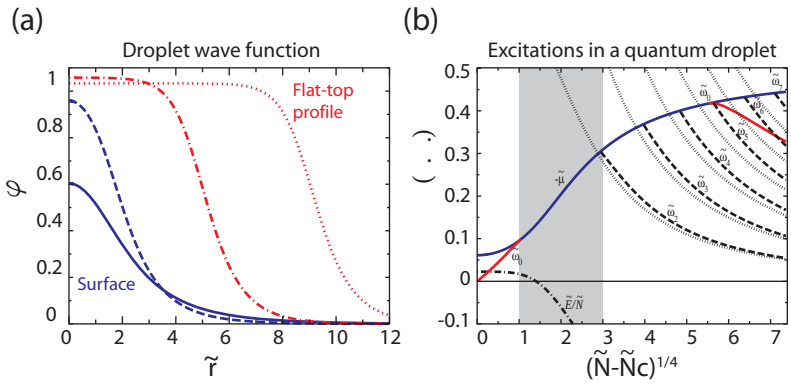

Figure 6.2: Figures taken from [3].(a) For large atom number a flat-top density profile, an inherent property of a liquid, is expected to occur. For low atom number, if the saturation density is not reached, the density profile is mainly dominated by surface effects. (b) The excitation spectrum of an isotropic droplet. The different modes are sketched. The dashed blue line represents the boundary between discrete modes and the continuum. The gray area represents the region where no excitations exist. The axis are presented in rescaled units, see [3] for details.

atom number $\tilde{N}_c$ the repulsive character of the quantum pressure dissociates the system into a gas. This phase transition is explained more in detail in the following sections.

Excitation spectrum

The quantum droplet is predicted to have a peculiar excitation spectrum. In particular with very few or absence of discrete modes. In the large droplet limit, its spectrum contains surface modes or so-called ripplons. These quantized surface waves are analogous to the ones found in superfluid ^{4}He [147].

Fig. 6.2 (b) shows the different modes $\tilde{\omega}_l$ as a function of the total atom number in the droplet. Here l represents the angular momentum. The axis is rescaled with respect to the critical atom number $\tilde{N}_c$ (see [3] for details). The solid blue line represents the particle emission threshold which separates the discrete modes of the droplet with

respect to the continuum. We observe how by decreasing the atom number the different modes cross the threshold and disappear. However, the monopole mode $\tilde{\omega}_0$ (solid red line) reappears again at low atom number.

This monopole mode corresponds to the breathing of the droplet radius, and therefore it does not conserve volume. This mode can be associated to the compressibility of the system [148]. The lower the monopole frequency is the larger the compressibility of the system. Intuitively we can expect that the compressibility of the droplet is larger close to the dissociation point $\tilde{N}_c$ this is why the frequency of the monopole is low in Fig. 6.2 (b). It costs less energy to deform or compress the droplet surface. At-large atom number, kinetic effects are not dominant, and it cost more energy to compress the bulk.

Regarding the surface modes $l \geqq 2$, they do not change the density of the droplet, and therefore the volume remains constant. The monopole is not coupled to the surface modes, this is why in Fig. 6.2 even though the monopole mode disappears close to $\tilde{\omega}_5$ the surface modes are still present.

For $l = 1$, the so-called dipole mode describes the evolution of the center of mass of the droplet. In BEC experiments the frequency of this mode is given by the harmonic confinement and its independent of two-body interactions. In the absence of external trapping potential $\tilde{\omega}_1 = 0$. This is why it is not included in Fig. 6.2 (b).

Finally, in an unexpected way a regime with no excitations appears (gray area) where any excitation in the droplet will couple directly to the continuum. The droplet will expel atoms, or in other terms will "self-evaporate" to a regime with not excitations. The consequence, as stated from the publication of D. Petrov is the possibility to create macroscopic zero-temperature objects:

> "This means that starting from an ordinary finite temperature trapped condensed mixture one arrives at a macroscopic zero-temperature object; excitations corresponding

to the continuum spectrum evaporate, when the trap is switched off [3]."

In the next section, we study more properties of these quantum droplets using an extended Gross-Pitaevskii equation together with a variational ansatz technique.

6.2.4 *Extended Gross-Pitaevskii equation with quantum fluctuations*

Following ref. [3] and using the effective low-energy theory presented in chapter 2 for Bose-Bose mixtures, we can write an extended Gross-Pitaevskii equation (eGPE) with an additional repulsive term. This additional term includes the effect of quantum fluctuations as an effective potential for the low-energy degrees of freedom of the system. We assume in our theory that both wavefunctions overlap by minimizing the mean-field energy through the condition $n_\uparrow/n_\downarrow = \sqrt{a_{\downarrow\downarrow}/a_{\uparrow\uparrow}}$ and therefore our measurements are valid in the absence of spin excitations [3]. In this chapter, we do not analyse the validity of this approximation, however in chapter 7 a detailed experimental analysis of the spin composition of the system is performed.

In the homogeneous case, the corresponding energy density functional reads

$$\begin{aligned}\mathcal{E} &= \mathcal{E}_{\text{kin}} + \mathcal{E}_{\text{MF}} + \mathcal{E}_{\text{LHY}} \\ &= \frac{\hbar^2}{2m} n_0 |\nabla\phi|^2 + \frac{4\pi\hbar^2\delta a}{m} \frac{\sqrt{a_{\downarrow\downarrow}/a_{\uparrow\uparrow}}}{(1+\sqrt{a_{\downarrow\downarrow}/a_{\uparrow\uparrow}})^2} n_0^2 |\phi|^4 \\ &+ \frac{256\sqrt{\pi}\hbar^2}{15m} \left(\frac{n_0\sqrt{a_{\uparrow\uparrow}a_{\downarrow\downarrow}}}{1+\sqrt{a_{\downarrow\downarrow}/a_{\uparrow\uparrow}}}\right)^{5/2} F\left(1, \frac{a_{\uparrow\downarrow}^2}{a_{\uparrow\uparrow}a_{\downarrow\downarrow}}, \sqrt{\frac{a_{\downarrow\downarrow}}{a_{\uparrow\uparrow}}}\right) |\phi|^5\end{aligned} \tag{6.3}$$

where $n_0 = n_\uparrow + n_\downarrow$ and $\mathcal{E}_{\text{kin}}$, $\mathcal{E}_{\text{MF}}$ and $\mathcal{E}_{\text{LHY}}$ denote the kinetic, potential, mean-field and quantum fluctuation (Lee-Huang-Yang) contri-

butions to the energy density of the mixture, respectively. This energy functional results in an extended Gross-Pitaevskii equation given by

$$i\hbar\dot{\phi} = \left[\left(-\frac{\hbar^2}{2m}\nabla^2\right) + \alpha n_0|\phi|^2 + \gamma n_0^{3/2}|\phi|^3\right]\phi, \tag{6.4}$$

where α and γ of the two last terms are defined as

$$\begin{aligned}\alpha &= \frac{8\pi\hbar^2\delta a}{m}\frac{\sqrt{a_{\downarrow\downarrow}/a_{\uparrow\uparrow}}}{(1+\sqrt{a_{\downarrow\downarrow}/a_{\uparrow\uparrow}})^2},\\ \gamma &= \frac{128\sqrt{\pi}\hbar^2}{3m}\left(\frac{\sqrt{a_{\downarrow\downarrow}a_{\uparrow\uparrow}}}{1+\sqrt{a_{\downarrow\downarrow}/a_{\uparrow\uparrow}}}\right)^{5/2} F\left(1, \frac{a_{\uparrow\downarrow}^2}{a_{\uparrow\uparrow}a_{\downarrow\downarrow}}, \sqrt{\frac{a_{\downarrow\downarrow}}{a_{\uparrow\uparrow}}}\right).\end{aligned}$$

6.2.5 *Variational Gaussian ansatz*

To obtain the ground state phase diagram given by Eq. 6.3 we use a variational technique. Similar to the calculation performed in section 2.4.3, we introduce a Gaussian ansatz of the form:

$$\phi(x,y,z) = \sqrt{n_0}\exp\left(-\frac{x^2}{2\sigma_x^2} - \frac{y^2}{2\sigma_y^2} - \frac{z^2}{2\sigma_z^2}\right), \tag{6.5}$$

where n_0 is the peak density of the system normalized through the condition

$$n_0 = \frac{N}{2\pi^{3/2}\sigma_x\sigma_y\sigma_z}. \tag{6.6}$$

We explore the regime where $\delta a < 0$. In particular we focus in the free space case where $V_{\text{ext}} = 0$. In such situation the system is isotropic therefore $\sigma_x = \sigma_y = \sigma_z = \sigma$. With these assumptions we minimize numerically Eq. 6.3.

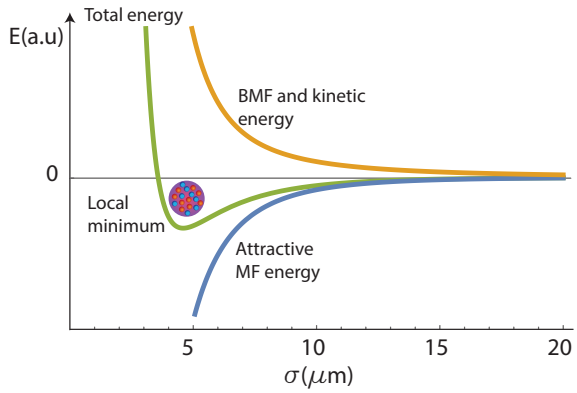

Figure 6.3: (a) The green line represents the total energy of the system for the total atom number $N = 500,000$ and $\delta a = -2.88\, a_0$ as a function of the radial size σ_r. We observe that a local minimum appears for a given width. The stabilization of a self-bound state in the absence of a trap is what we call quantum droplet.

Ground state phase diagram

The ground state phase diagrams shown in this section are obtained for the relevant parameters in the mixture of ^{39}K (see section 6.4 for details).

Using the previous formalism, we find the equilibrium points where the width of the system minimizes its energy. In Fig. 6.3, we show the energy of the binary atomic cloud as a function of σ (green line). For a total atom number $N = N_\uparrow + N_\downarrow$ and interaction strength $\delta a < 0$ the cloud does not collapse, as expected from mean-field theory, but instead minimizes the energy forming a system with finite size. This self-bound phase in the absence of trapping potential is what we identify as: **quantum liquid droplet**.

Without the presence of the BMF contribution (yellow line), we could recover for low atom number the stability diagram shown in Fig. 2.4. Due to the competition of the BMF (yellow line) and MF (blue line) energy, a minimum appears which defines the size of the quantum droplet.

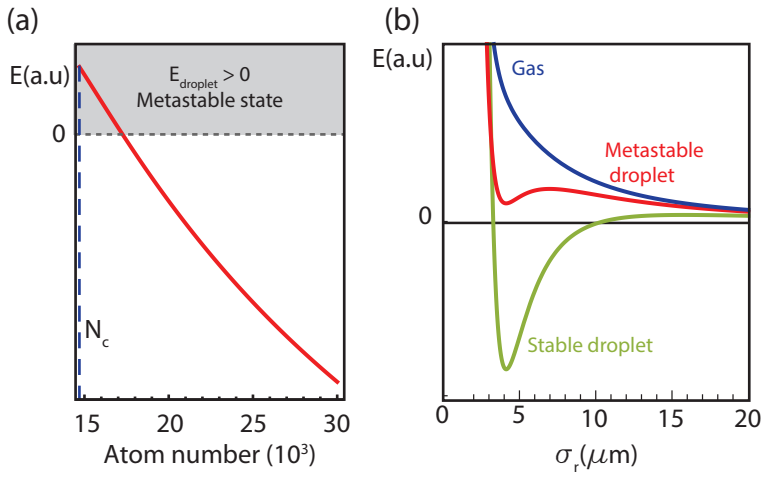

Figure 6.4: (a) Droplet energy as a function of atom number. We observe that for low atom number the droplet becomes metastable ($E_{\text{droplet}} > 0$) and then unstable for a critical atom number N_c. (b) Droplet minima for three different values of N. For large atom number ($N > N_c$) the droplet is stable (green line). Close to the critical atom number $N \sim N_c$ the droplet becomes metastable (red line). Finally for low atom number ($N < N_c$) the droplet dissociates into a gas.

In Fig. 6.4 (a) we depict the droplet energy as a function of the total atom number. We find that the droplet becomes metastable $E_{\text{droplet}} > 0$ (shaded area) by decreasing the atom number. For a critical value N_c the minimum in energy disappears; In Fig. 6.4 (b) we show the minima in energy for a stable droplet (green) and metastable droplet (red). Below N_c when the minimum in energy disappears this results in a liquid-to-gas phase transition.

In fact, if we compute the density landscape of the droplet as a function of the total atom number N (see Fig. 6.5 (a)), for a critical atom number N_c, the droplet solution vanishes and instead the system goes back into a gas phase.

This gas phase is interesting on its own. Effectively the system is dominated by the attractive character of the mixture (remember we are at $\delta a < 0$); however, the gas does not collapse. In chapter 2, we

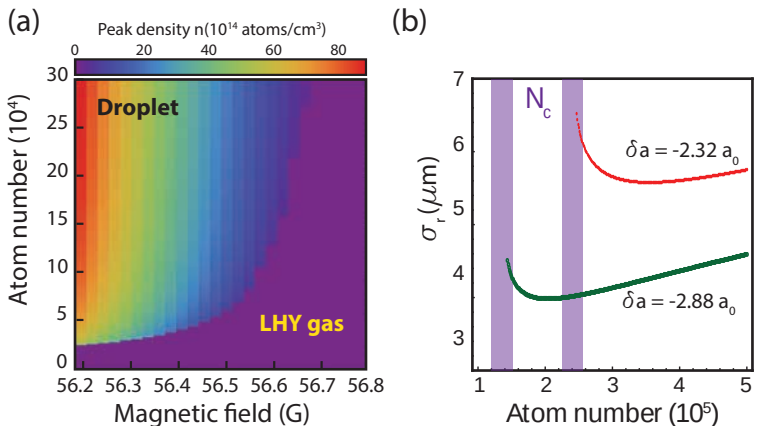

Figure 6.5: (a) Phase diagram of a ^{39}K Bose-Bose mixture for $\delta a < 0$. Depending of the critical atom number and interaction strength the system could form a quantum liquid droplet or remain in the LHY gas phase. (b) For a critical atom number N_c the system dissociates into a gas. This is depicted in the shadowed area where the width of the droplet diverges.

have explained that a homogeneous condensate with attractive interactions collapses. We have presented as well that a trapped condensate can circumvent the collapse for low atom number due to the quantum pressure. However, in the present case, the condensate exists for attractive interactions without the atom number constraint and in the absence of a trap. This we call a **LHY gas**.

Following refs. [3, 141, 149, 150], we attribute this liquid-to-gas phase transition to the effect of quantum pressure, which acts as a repulsive force. As the atom number decreases, the relative weight between kinetic ($\mathcal{E}_{\mathrm{K}}$) and interaction energies ($\mathcal{E}_{\mathrm{MF}}$, $\mathcal{E}_{\mathrm{LHY}}$) changes, for each energy term scales differently with N: $\mathcal{E}_{\mathrm{K}} \propto N$, $\mathcal{E}_{\mathrm{MF}} \propto N^2$ and $\mathcal{E}_{\mathrm{LHY}} \propto N^{5/2}$. Below a critical atom number, kinetic effects become sufficiently strong to drive this transition. In Fig. 6.5 (b) we show the evolution of the droplet width as a function of atom number for two different interaction strengths δa. For a critical atom number N_c (depicted in shadow area) the width of the droplet diverges.

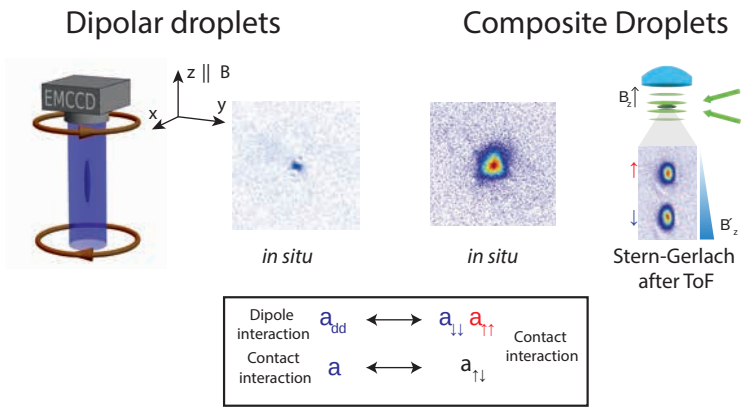

Figure 6.6: Dipolar droplets vs. Composite droplets. (Left panel) Figure taken from [141]. Dipolar droplets have two sorts of interactions: Dipole-dipole interaction and contact interaction. Depending on the quantization axis and geometry of the trap, this two interactions can be tuned in order to create a dipolar quantum droplet. (right panel) Composite droplets are formed using a Bose-Bose mixture, this is revealed with a Stern-Gerlach experiment after ToF. Here the two interactions that can be controlled are the inter- and intra-species one. (Black box) Correspondence between dipolar and composite droplets. In both systems the two sorts of interactions can compete to reduce the MF energy and allow to reveal BMF effects.

Regarding the density profile of this self-bound state, for an equilibrium density n_{eq}, a flat top profile is expected (see section 6.2.3). We cannot account for this effect in our variational model due to the shape of our initial Gaussian ansatz.

In the following sections we present how the phase diagram in Fig. 6.5 (a) is modified in the presence of a trapping potential. This will be discussed in detail in section 6.6.4.

6.3 COMPOSITE DROPLETS VS DIPOLAR DROPLETS

Along this section we have explored the mechanism of stabilization in composite quantum droplets together with the main properties of

such liquid phase. However, it is essential to remark some similarities and differences between these droplets and the dipolar droplets.

Both composite and dipolar droplets are stabilized through the same mechanism: quantum fluctuations. In both cases, the competing interactions in the system allow observing beyond mean-field effects. For composite droplets (right panel of Fig. 6.6 shows after ToF its composite nature) the contribution of the mean-field energy is reduced due to the competition between inter- (positive) and intra- (negative) interactions.

Dipolar droplets, instead, are made of a single component dipolar BEC. In contrast to non-dipolar BEC, here dipole-dipole interactions are important in addition to the contact interaction. Depending on the quantization axis and geometry of the trap, in this system, the mean-field energy is reduced due to the competition of this two sort of interactions. This is sketched in Fig. 6.6 (left panel).

The anisotropic character of dipole-dipole interactions gives the main difference between these two quantum liquids. Dipolar droplets are elongated systems along the magnetic field quantization axis (see left panel Fig. 6.6). In the case of composite droplets only contact interactions play a role and therefore they are isotropic.

If several dipolar droplets are formed, they tend to spatially separate due to the strong dipole-dipole interaction between them, however for the composite ones, the interaction effects between several droplets are negligible.

Remark. We conclude this section emphasizing that in dipolar droplets and composite droplets, despite of being two different systems, the stabilization mechanism has the same origin. In the inset of Fig. 6.6, the mapping between both systems due to the interactions is presented. In both cases the mean-field energy is reduced by the competition of two different terms. In our case, intra- and inter-species interactions compete while in dipolar droplets these are contact and dipolar interactions.

6.3.1 *Dipolar droplets state-of-the-art*

Before presenting our results in composite droplets, here we summarize the current research in dipolar droplets.

So far two different groups have been working with dipolar droplets: T. Pfau´s group with Dysprosium (^{164}Dy) and F. Ferlaino´s group with Erbium (^{166}Er) atoms. In several publications, they have characterized different properties of their systems.

The first observation of dipolar droplets was performed with Dy atoms [137]. They reported the "crystallization" of a Dysprosium dipolar condensate in the regime where a mechanical instability should occur. This self-organized structure made of several long-lived droplets is analogous to the Rosensweig instability in classical ferrofluids [151]. Shortly after they reported the observation of stable dipolar droplets that confirmed quantitatively that indeed quantum fluctuations stabilized the system against the expected mean-field collapse [138]. This was tested by measuring the density of these small droplets ($\sim$ 800 atoms) and comparing the density scaling as a function of the interaction strength. The three-body repulsion mechanism proposed to explain the observation of quantum droplets could not explain the experimental observations. In addition, in the same publication they have observed matter wave interference of several droplets.

This dilute liquid phase has been characterized in terms of the total atom number and interaction strength. In fact, a liquid-to-gas phase transition in the system was observed [141]. Below a critical atom number, it was shown that the droplet dissociates into a gas.

The peculiar excitation spectrum of ultra-cold quantum droplets is one of the properties that is object of attention. However, it has been shown theoretically that dipolar droplets do not exhibit the no-excitation regime proposed originally for composite droplets [152]. Nevertheless, the collective modes of an Er droplet have been measured to unveil the presence of the LHY energy as a key ingredient of the stabilization mechanism [139]. Dy experiments have explored

as well the collective modes of the droplet. Here they have focused in particular in the *scissor mode* [153]. By measuring the mode frequency they have extracted the unknown background scattering length of Dy.

Finally, recent experiments with Dy atoms have explored the phase diagram of a dipolar condensate as a function of the contact interaction a and trap aspect ratio λ_{trap} [140]. For λ_{trap} above a critical value of λ_c, the BEC could evolve into a droplet adiabatically and create a single self-bound state. However for $\lambda_{\text{trap}} < \lambda_c$ a modulation instability could lead to the formation of crystals. These results provide the connection between the formation of dipolar crystals in ref. [137] with respect to the formation of a single dipolar droplet presented in refs.[138, 141].

6.4 QUANTUM DROPLETS: EXPERIMENTAL OBSERVATION

6.4.1 *Scattering lengths: the magic magnetic field window*

The mechanism of stabilization of such droplets is general for any Bose-Bose mixture. The main condition is to find a configuration where the intra-species interaction is repulsive while the inter-species interaction is attractive. Despite the diversity of degenerate atomic mixtures that have been produced, the promising candidates are ^{39}K-^{23}Na [154], ^{87}Rb-^{39}K [55], ^{87}Rb-^{41}K [155, 156]. There the overlap of several Feshbach resonances presents a regime where $\delta a < 0$.

Interestingly a Bose-Bose mixture made of internal states of either ^{41}K or ^{39}K presents such condition as well. This is convenient because gravitational sag is therefore negligible and both components overlap perfectly. Undoubtedly, this feature simplifies the experiment and therefore we have decided to explore both options.

In Fig. 6.7, the scattering length of the states $|\uparrow\rangle \equiv |m_F = -1\rangle$ and $|\downarrow\rangle \equiv |m_F = 0\rangle$ of the $F = 1$ manifold for ^{39}K and ^{41}K are shown as a function of magnetic field B. In both cases the green line depicts the parameter δa defined previously. The gray vertical dashed line splits the regime where δa is positive or negative.

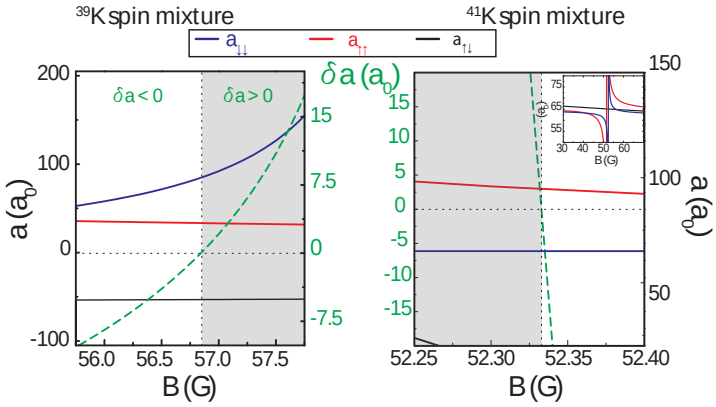

Figure 6.7: Scattering lengths a (solid lines) and parameter $\delta a = a_{\uparrow\downarrow} + \sqrt{a_{\uparrow\uparrow} a_{\downarrow\downarrow}}$ (dashed line) vs. magnetic field B for a ^{39}K (left) and ^{41}K (right) mixture both in states $|\uparrow\rangle \equiv |F = 1, m_F = -1\rangle$ and $|\downarrow\rangle \equiv |F = 1, m_F = 0\rangle$. The condition $\delta a = 0$ (dashed vertical line) separates the repulsive ($\delta a > 0$, grey area) and attractive ($\delta a < 0$, white area) regimes. In both cases a statistical mixture in the internal states $|\uparrow\rangle \equiv |m_F = -1\rangle$ and $|\downarrow\rangle \equiv |m_F = 0\rangle$ is prepared with a radio-frequency (RF) pulse.

For ^{39}K the regime where droplets exist is broader in magnetic field compared to ^{41} K. Concerning the magnetic field stability, it is experimentally less demanding; therefore we have decided to perform the experiments presented in this thesis using the bosonic isotope ^{39}K. However, it is important to stress that we have observed similar results to the ones presented in this chapter using ^{41}K.

Key ingredients

Experimentally, the main idea behind the observation of composite quantum droplets is to prepare a Bose-Bose mixture in the right range of magnetic field ($\delta a < 0$) and look for a "smoking gun" of the gas-to-liquid phase transition. The droplet should exist in the absence of external confinement and the time evolution of the system needs to behave completely different from the BEC. In one case ($\delta a > 0$), the

binary condensate should expand in the absence of external confinement (as expected for a gas in the absence of container). In the other case ($\delta a < 0$) the ground state should form a self-bound object (liquid droplet).

In our experiments, the droplet is highly sensitive to the preparation procedure and therefore it is easy to excite the ground state of the system and create multiple droplets. Therefore, to resolve the formation of one single droplet, we observe the system *in situ* using a high numerical aperture objective together with a dark phase contrast scheme (see section 3.4). Using absorption imaging after time-of-flight would not resolve in many cases the formation of several droplets during the preparation, and therefore it could lead to misinterpretation of the results[1].

We prepare the system adiabatically as it will be explained in the following section. Due to the low atom number in our initial ^{39}K condensate (see chapter 4), we neither achieve flat-top density droplets nor access the regime where collective excitations are suppressed [3]. Therefore the different ramps in the sequence need to be at least comparable to the frequency of the low branch monopole mode of the droplet. This is on the order of ~ 10 Hz[2]. Dipolar droplets present similar sensitivity to the preparation sequence as reported in [157, 158].

One important thing to consider is that self-bound solutions for attractive BEC exist in the presence of confinement, these are called bright solitons (see [159] and references therein). Therefore we need to ensure that we do not confuse the observation of a quantum droplet with this self-bound matter wave. These two finite size systems are a priori different states that can coexist in some specific conditions, however, a full discussion on this topic is presented in chapter 7.

In order to discern bright solitons from quantum droplets, and explore the properties of the system, here we perform the experiment in

1 We started our experiments using absorption imaging after ToF without success. Only after using *in situ* imaging we understood the sensitivity of the preparation.

2 According to our variational calculation not presented in this thesis

one single plane of a blue-detuned optical lattice (see section 3.4). This configuration is convenient for the following reasons:

- We can levitate the two-component mixture against gravity (spin independent potential). Magnetic levitation is not possible due to the opposite magnetic dipole moment of the different internal degrees of freedom of the mixture. In this situation, we do not have to deal with gravitational sag (this will be crucial in case of using a Bose mixture of two different atoms).
- The high N.A aperture objective is orthogonal to the lattice plane. We can observe the evolution of the system within the field of view.
- The lattice potential provides confinement only on the vertical direction and a small anti-curvature in the radial plane. With this geometry, bright solitons (mean-field localized solutions) do not exist [21, 160]. Therefore in our experimental setup, the presence of any self-bound state corresponds to a quantum droplet state.

In addition, to corroborate the absence of bright solitons in our experimental geometry, we have explored the regime of attractive interactions in a single component condensate. Here the system should collapse due to the negligible contribution of the LHY energy. Using either a one- or two- component condensate, we can effectively compare in the same experimental setup the behavior of systems with and without the presence of the LHY contribution.

Finally, with this potential the radial plane is free of confinement, therefore we have observed that it is important to compensate the residual magnetic gradients in this plane. This increases the lifetime of the droplets. We use the cloverleaf coils presented in chapter 3 to perform this task .

Remark. In this chapter, we observe the evolution (dynamics) of the system on the lattice plane. Even though the word lattice is employed,

we do not study any sort of Hubbard model. In fact, the lattice spacing between planes is so large that the hopping term is close to zero and can be neglected in our experimental timescales.

6.5 MAKING AND PROBING QUANTUM DROPLETS

6.5.1 *Experimental sequence*

The experimental sequence developed to observe our composite quantum droplets is sketched in Fig. 6.8. We can summarize it as follows

- (a) The experiment starts with a pure BEC of ^{39}K in state $|\uparrow\rangle \equiv |m_F = -1\rangle$ of the $F = 1$ hyperfine manifold. The atoms are loaded in one plane of a vertical blue-detuned lattice potential. Here, a crossed vertical red-detuned optical dipole trap provides radial confinement in the horizontal plane. In this configuration, a balanced mixture is prepared in the states $|\uparrow\rangle \equiv |m_F = -1\rangle$ and $|\uparrow\rangle \equiv |m_F = 0\rangle$. To this aim we apply a radio-frequency pulse at $B \approx 57.3$ G, which lies in the miscible regime ($\delta a \approx 7\, a_0$) [50].

- (b) We ramp down the magnetic field at a constant rate of 59 G/s and enter the attractive regime $\delta a < 0$. At the same time, we ramp up the magnetic field of the cloverleaf coils to compensate for magnetic gradients. During the magnetic sweep, we decompress the radial confinement to a value depicted as Z_{final} in Fig. 6.8. This confinement defines the width of the atomic cloud, and therefore it is matched to the expected initial size of the droplet in order to avoid excitations. We observe large oscillations of the droplet that dissociate the system if the initial size is not matched properly.

- (c) Once the system is at the right magnetic field value and optimum radial confinement, we switch off the vertical red-detuned optical dipole trap while keeping only the lattice confinement.

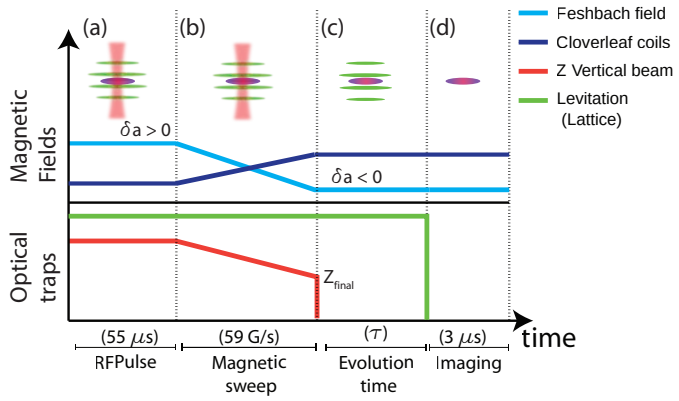

Figure 6.8: After transferring the atoms to a single plane of the lattice potential, we adiabatically go from the miscible regime to the droplet regime. The radial confinement (red line) is reduced in order to match the theoretical width of the droplet for a given interaction strength with the size of the atomic cloud. The *in situ* imaging is performed at high field in the absence of trapping.

This allows the atoms to evolve freely in the horizontal plane for a time τ.

- (d) The integrated atomic density is imaged *in situ* at high magnetic field for different evolution times. We remove the levitation potential just before the imaging pulse in order to avoid light shifts of the transition that could affect our imaging calibration.

6.5.2 *Loading the blue-detuned lattice potential*

The droplet experiment is performed in a blue-detuned lattice potential. The lattice spacing is close to 10 μm as explained in section 3.3.5. In order to maximize the transfer of the atoms to one single plane of the lattice potential we use the following protocol (see Fig. 6.9): (a) The condensate is first prepared in a nearly isotropic optical crossed dipole trap. (b) We then reshape the atomic cloud by transferring the atoms to a red-detuned elliptical pancake trap with an aspect ratio 5:1.

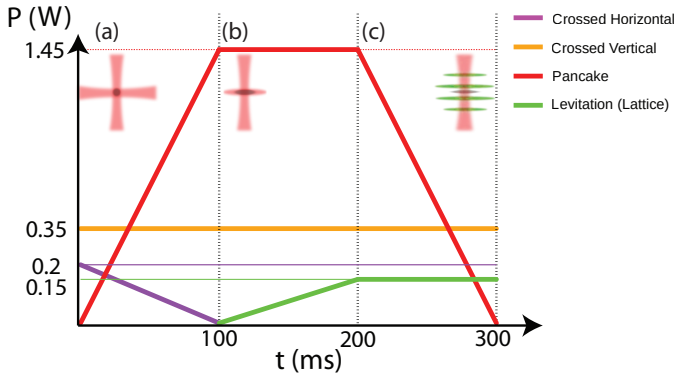

Figure 6.9: Experimental protocol used to transfer the atoms from a crossed optical dipole trap to one single plane of a blue-detuned lattice potential. The atoms on the crossed optical dipole trap (a) are first preshaped in a pancake trap (b) in order to maximize the loading into one plane of the lattice potential (c). The vertical width of the condensate in the pancake trap is smaller than the lattice spacing of the blue-detuned potential.

This gives, as a result, a "flat" BEC of vertical width smaller than the lattice spacing of the blue-detuned potential. At the end of this protocol, close to 100 % of the atoms are transferred to one single plane. More details about the transfer to the blue-detuned lattice potential, its characterization, and some other features can be found in [98].

6.5.3 *3-D criteria*

Using small angle lattices has been shown to be an alternative way to create 2-dimensional systems [161]. However, we are interested in the properties of the liquid state in the three-dimensional regime. In our case, although the system is not isotropic due to the vertical confinement, the vertical trap frequency is chosen such that it is large enough to compensate gravity but small enough that the BEC can still be considered as three-dimensional.

For the experimental parameters, the vertical trapping frequency is $\omega_z/2\pi = 635(5)$ Hz. We compare the vertical harmonic oscillator

length $a_{\mathrm{ho}} = 0.639(3)\ \mu$m with the characteristic length of the most energetic Bogoliubov excitation branch of the Bose-Bose mixture (see Eq. 2.51). The a_{ho} is typically a factor of 3 larger than ξ_s. We assume that this corresponds to a three-dimensional regime.

6.5.4 *Imaging and atom number calibration with open transitions*

In order to perform reliable *in situ* imaging of the droplets, we employ the dispersive polarization phase-contrast technique explained in chapter 3. We image orthogonally to the plane where the system evolves; therefore we obtain the integrated density of the atomic cloud along the vertical direction. The vertical confinement imposes the width σ_z of the cloud, this is on the order of the harmonic oscillator length.

The major challenges for imaging our system are the following:

- The densities of the condensate/droplet are high therefore we cannot perform reliable *in situ* absorption imaging [162]. We use a dispersive imaging technique where we exploit the birefringence of the atoms to circumvent this problem.
- We cannot extinguish fast enough the magnetic Feshbach field to perform imaging at zero field with a closed optical transition. We observe that during switch-off the results of the measurements are modified. Thus the imaging is performed at high field using non-cycling transitions.
- We perform phase contrast imaging at high field, however the shift of polarization is low. Thus due to the composition of the states in terms of the electronic spin projection (m_s), we need to perform the imaging "close to resonance" to increase the signal-to-noise ratio. However close to the resonance transition we cannot perform non-destructive imaging.
- We must use short imaging pulses to avoid depumping to states that are not coupled to the imaging light.

- In our current configuration it is not possible in one single shot to obtain spin-resolved images.

To circumvent these problems we illuminate the atoms for only 3 μs with a probe beam linearly polarized along a direction perpendicular to the applied magnetic field. The imaging pulses are shorter than the depumping time. We obtain the Faraday coefficients of the two states independently using the method presented in chapter 3. For each state, we measure the polarization phase shift as a function of n. We choose an imaging beam frequency for which we have the same sensitivity for both spin states. This condition is found with a detuning $\Delta_{|\uparrow\rangle} = -73(1)$ MHz and $\Delta_{|\downarrow\rangle} = -105(1)$ MHz from the respective transition

$$|\uparrow\rangle \rightarrow \left|m_{J'} = -3/2, m_{I'} = -1/2\right\rangle$$
$$|\downarrow\rangle \rightarrow \left|m_{J'} = -3/2, m_{I'} = 1/2\right\rangle,$$

with J the total electronic angular momentum and I the nuclear spin. For the magnetic field range of the experiment this yields nearly identical Faraday coefficients for the two components $c_{F,\uparrow} = 1.1(1) \times 10^{-11}$ rad·cm^2 and $c_{F,\downarrow} = 1.4(1) \times 10^{-11}$ rad·cm^2.

Several challenges were found during the calibration of the atom number, therefore we have just summarized here the essential experimental details. The full analysis and comparison with theoretical calculations will be reported in the thesis of J. Sanz.

Cross-check of the imaging calibration

We perform an independent cross-check of our calibration procedure exploiting the transition

$$|F = 2, m_F = -2\rangle = |m_J = -1/2, m_I = -3/2\rangle \rightarrow \left|m_{J'} = -3/2, m_{I'} = -3/2\right\rangle,$$

which is cycling at any magnetic field.

To this end, we transfer the atoms from $|\uparrow\rangle$ to $|F = 2, m_F = -2\rangle$ with an RF pulse before imaging them on the cycling transition at different detunings. This allows us to compare our calibration with the expected two-level system prediction, finding excellent agreement. Second, by transferring a variable fraction of atoms to $|F = 2, m_F = -2\rangle$, we confirm the linearity of our imaging scheme and rule out the existence of collective atom-light interaction effects in the imaging.

6.6 QUANTUM DROPLETS VS. QUANTUM GASES

The "smoking gun" in our experiment is the observation of a self-bound state in the presence of only vertical confinement. After the experimental sequence presented in section 6.5, we let the system evolve for different times t. Subsequently, the mixture is imaged *in situ*.

Typical images of the mixture time evolution in the repulsive and attractive regimes are displayed in Fig.6.10. For $\delta a = 1.2(1)\, a_0 > 0$ (top row), the cloud expands progressively in the plane, as expected for a repulsive Bose gas in the absence of radial confinement. In contrast, in the attractive regime, $\delta a = -3.2(1)\, a_0 < 0$ (central row), the dynamics of the system is remarkably different, and the atoms reorganize in an isotropic self-bound liquid droplet. Its typical size remains constant for evolution times up to 25 ms.

In the presence of a small trapping potential in the radial direction, at the mean-field level, the system should also form a self-bound state as explained in chapter 2. To verify that our results at this level are not corresponding with bright solitons, in an analogous experiment with a single-component attractive condensate $|\downarrow\rangle$ of scattering length $a = -2.06(2)\, a_0 < 0$, we have observed how the system collapses (bottom row). This is expected to happen due to the absence of any restoring force. In section 2.6.5, we have explained that the theory for single and two-component condensates are equivalent at the mean-field level provided one replaces $\delta a \to\sim 2a$; therefore we can conclude that in our experimental geometry, quantum pressure can never stabilize bright

solitons due to the presence of weak anti-confinement in the horizontal plane.

In dipolar experiments, it is complicated to study systems close to the collapse point where the effect of the LHY energy does not contribute. Comparing in the same experimental setup equivalent systems where beyond mean-field corrections can be effectively "switched off" is a unique property of composite mixtures.

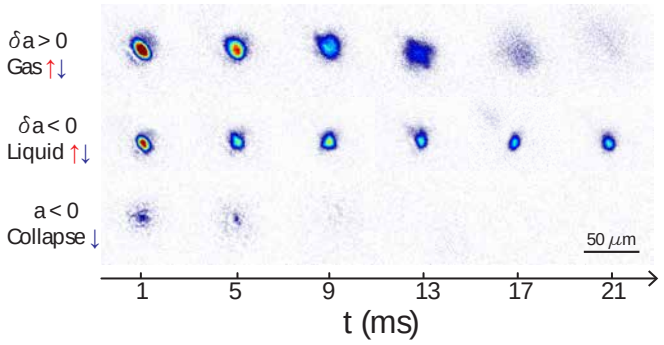

Figure 6.10: Evolution of the mixture. Typical *in situ* images taken at time t after removal of the radial confinement but in the presence of the lattice potential. Top row: expansion of a gaseous mixture ($B = 56.935(9)$ G and $\delta a = 1.2(1)\, a_0 > 0$). Central row: formation of a self-bound mixture droplet ($B = 56.574(9)$ G and $\delta a = -3.2(1)\, a_0 < 0$). Bottom row: collapse of a single-component $|{\downarrow}\rangle$ attractive condensate ($B = 42.281(9)$ G and $a = -2.06(2)\, a_0 < 0$). In our geometry, quantum pressure cannot stabilize bright solitons. Therefore, the existence of self-bound liquid droplets is a direct manifestation of beyond mean-field effects.

6.6.1 *Characterization of the liquid phase*

To further characterize the mixture, we perform a quantitative analysis of the Fig. 6.10 by fitting the integrated atomic density profiles with a two-dimensional Gaussian $N e^{-x^2/\sigma_x^2 - y^2/\sigma_y^2}/(\pi\sigma_x\sigma_y)$. We find $\sigma_x/\sigma_y \approx 1$ for all our measurements and therefore we define $\sigma_r = \sqrt{\sigma_x\sigma_y}$. We extract the atom number N and radial size σ_r and infer the peak density

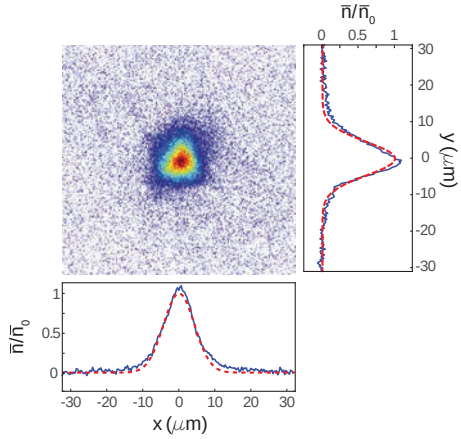

Figure 6.11: Experimental density profiles. *In situ* column density profile of a quantum droplet integrated along the imaging direction z, for $N = 1.7(4) \times 10^4$ and $B = 56.574(9)$ G ($\delta a = -3.2(1)\, a_0$). The right and bottom panels depict the corresponding doubly-integrated density profiles $\bar{n}$ (solid lines), together with the two-dimensional Gaussian fit used to analyze the data (dashed lines). Both are normalized to the peak value $\bar{n}_0$.

$n_0 = N/(\pi^{3/2}\sigma_r^2\sigma_z)$ by assuming a vertical size σ_z identical to the harmonic oscillator length a_{ho}.

Data analysis

For the initial atom number in our experiment, as we will explain in the next section, we do not reach the equilibrium density n_{eq}. Therefore our droplet is mainly made of "surface" (see Fig. 6.2 (a)) and the fitting function accounts well for the measured density profiles.

We have verified that the zeroth and second moments of raw images give compatible results for the atom number and radial size, respectively.

Results

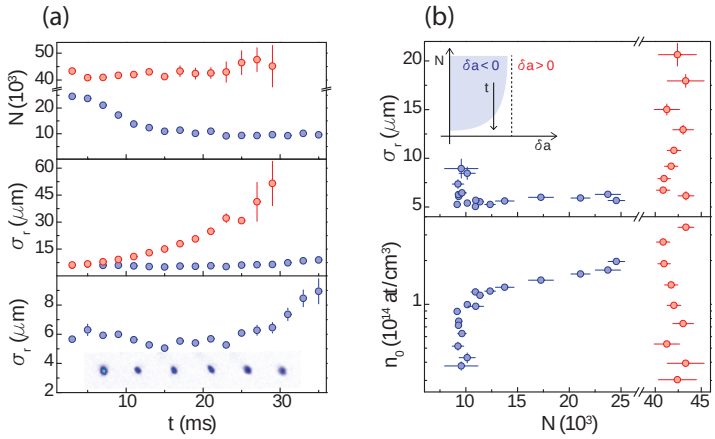

Figure 6.12: Liquid-to-gas transition. (a) Atom number N and radial size σ_r of the mixture for different evolution times t. The measurements are taken in the repulsive ($\delta a = 1.2(1)\, a_0 > 0$, red circles) and attractive ($\delta a = -3.2(1)\, a_0$, blue circles) regimes. Top panel: while for $\delta a > 0$ the atom number in the gas remains constant, for $\delta a < 0$ it decreases on a timescale compatible with three-body recombination. Central panel: the radial size of the droplet remains constant at $\sigma_r \approx 6\,\mu$m, demonstrating its self-bound nature. In contrast, the size of the gas increases continuously with time. Bottom panel: closer view of σ_r for $\delta a < 0$. For $t > 25$ ms the droplet dissociates and a liquid-to-gas takes place. The inset displays images corresponding to $t = 25 - 35$ ms. (b) Radial size σ_r (top panel) and peak density n_0 (bottom panel) vs. N. For $\delta a < 0$ and large atom number both remain approximately constant, as expected for a liquid. For a critical atom number we observe that σ_r diverges and n_0 drops suddenly, signalling the liquid-to-gas transition. In the gas phase, the $\delta a < 0$ system behaves as the $\delta a > 0$ one. Inset (top panel): sketch of the phase diagram. In the liquid phase (blue region), observing the mixture at variable evolution times gives access to different values of N (black arrow). Error bars represent the standard deviation of 10 independent measurements. If not displayed, error bars are smaller than the size of the symbol. Additionally, N has a calibration uncertainty of 25%

The evolution time of the atom number N and size σ_r is measured for the interaction parameters of Fig. 6.10. This is represented in Fig.6.12 (top and central panel). For $\delta a > 0$ (red circles) the gas quickly expands while its atom number does not vary. Instead, for $\delta a < 0$ (blue circles)

the system is in the liquid regime, and the radial size of the droplet remains constant at $\sigma_r \approx 6\,\mu$m. Initially its atom number is $N = 24.5(7) \times 10^3$, corresponding to a peak density of $n_0 = 1.97(8) \times 10^{14}$ atoms/cm^3. We attribute the subsequent decay of the droplet atom number shown in the top panel of Fig. 6.12 (a) to three-body recombination. By directly measuring the density of our droplets we confirm that they are more than eight orders of magnitude more dilute than liquid helium and remain very weakly interacting. Indeed, the interaction parameters of each component are small.

$$(n_\uparrow a_{\uparrow\uparrow}^3, n_\downarrow a_{\downarrow\downarrow}^3, \sqrt{n_\uparrow n_\downarrow} a_{\uparrow\downarrow}^3) \sim 10^{-5}.$$

6.6.2 *Inelastic losses and three-body decay model*

In Fig. 6.12 (a), we attribute the atom number decay to inelastic processes. The main contribution could be given by either two- or three-body losses. We neglect two-body inelastic processes (dipole-dipole interactions), because these rates[3] are too small to explain the fast decay time observed. Since no theoretical predictions are available for the three-body recombination rates $K_{\uparrow\uparrow\uparrow}$, $K_{\uparrow\uparrow\downarrow}$, $K_{\uparrow\downarrow\downarrow}$ and $K_{\downarrow\downarrow\downarrow}$, we determine their values experimentally.

Measuring the three-body coefficient K3

In the experiment we trap thermal atomic clouds using an additional trap along the $X-$axis with 100 μm waist and 1.5 W of power together with the optical dipole trap along $W-$axis. The mean trap frequency of the resulting potential is $\bar{\omega}/2\pi = 331(7)$ Hz and the depth is $U_0/k_B = 36(2)\,\mu$K.

3 $K_{\uparrow\downarrow} < 1.92 \times 10^{-16}$ cm^3/s, $K_{\uparrow\uparrow} < 2.34 \times 10^{-15}$ cm^3/s, and $K_{\downarrow\downarrow} < 7.28 \times 10^{-16}$ cm^3/s computed by A. Simoni using a coupled-channel calculation.

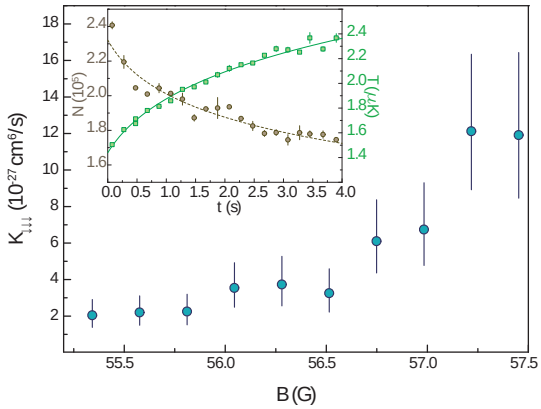

Figure 6.13: Three-body recombination rate $K^{\text{th}}_{\downarrow\downarrow\downarrow}$ as a function of magnetic field B. Inset: time evolution of the atom number N and temperature T at $B = 55.811(9)$ G, fitted to eq. (6.7) (dotted line) and eq. (6.8) (solid line).

We then record the time evolution of their atom number N and temperature T. For single-component systems, we model our measurements by the set of coupled equations

$$\frac{\dot{N}}{N} = -\frac{\beta}{\sqrt{27}}\frac{K_3^{\text{th}} N^2}{T^3} \tag{6.7}$$

$$\frac{\dot{T}}{T} = \frac{\beta}{\sqrt{27}}\frac{K_3^{\text{th}} N^2 (T + T_h)}{3T^4}, \tag{6.8}$$

which includes the effect of anti-evaporation [163]. In other words, we include the heating of the cloud due to the loss of the less energetic atoms after the three-body collision. Additionally, the parameter T_h is introduced in order to account for recombination heating. Finally, here $\beta = (m\bar{\omega}^2/2\pi k_{\text{B}})^{3/2}$, K_3^{th} denotes the corresponding three-body recombination rate. We neglect evaporation effects, which is a good assumption in our parameter regime $T \lesssim 2.5\mu\text{K} \ll U_0/k_{\text{B}}$.

We have performed these measurements in single-component samples of $|\uparrow\rangle$, $|\downarrow\rangle$ and in mixtures of different concentrations. The in-

set in Fig. 6.13 represents typical data during the measurement. For the magnetic field range of the experiment, we find that losses of $|\downarrow\rangle$ dominate over all the other processes and that the effective three-body loss rate of the mixture is proportional to the fraction of atoms in this state. The Fig. 6.13 summarizes the magnetic field dependence of $K^{\text{th}}_{\downarrow\downarrow\downarrow}$ as a function of magnetic field B. It remains approximately constant in the range $55.5 - 56.5$ G studied in Fig. 7.8. We analyze the corresponding decay of the self-bound atom number using the average value $K^{\text{th}}_{\downarrow\downarrow\downarrow} = 3(1) \times 10^{-27}$ cm^6/s. The other three rates are compatible with the ^{39}K background value 7.74×10^{-29} cm^6/s [32, 164]. Note that all our three-body loss rate measurements have a large systematic uncertainty (not included in the error bar) of up to a factor of two, dominated by the 25% systematic uncertainty of the atom number calibration (see section 3.4).

In conclusion for the densities explored in the experiment inelastic processes are dominated by three-body recombination in the $\downarrow\downarrow\downarrow$ channel.

Unexpected enhancement of the three-body collisions

During the measurement of the three-body loss coefficient K_3 in the state $|\downarrow\rangle \equiv |F = 1, m_F = 0\rangle$ we discovered that for a magnetic field ~ 54.8 G ($\sim 39a_0$), an enhancement of the three-body loss rate appears. This is depicted in Fig. 6.14.

The evidence of a three-body recombination maximum might correspond to Efimov physics [165].

Further investigation is required to provide a deeper understanding of the origin of this unexpected enhancement in the three-body collision rate. This feature appears in a regime where we do not expect an Efimov resonance using the theory presented in [166]. This theory is valid in the universal regime where the scattering length a is larger than the effective range of the potential r_0. However here we are in a situation where $a \sim r_0$.

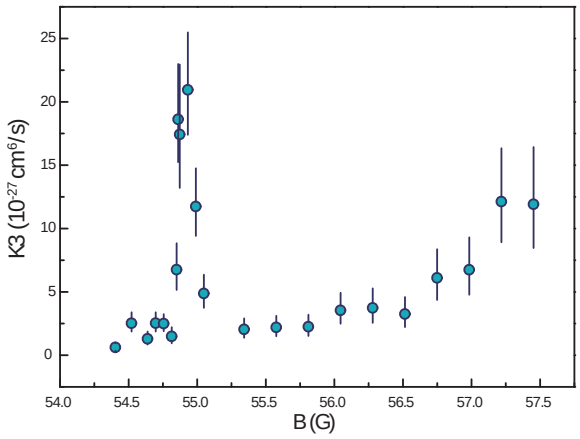

Figure 6.14: Enhancement of the three-body recombination rate in the state $|F = 1, m_F = 0\rangle$ at ~ 54.8 G. This corresponds to a scattering length of $\sim 39\ a_0$.

This enhancement could also be associated with higher partial waves resonances. Preliminary calculations (A. Simoni and P. Julienne, private communication), seem however to discard this possibility.

6.6.3 *The quantum liquid-to-gas phase transition*

For a given atom number, we expect that the quantum liquid droplet should dissociate into a gas due to the effect of quantum pressure, which acts as a repulsive force. Below a critical atom number, kinetic effects become sufficiently strong to drive a liquid-to-gas transition.

An insight of the phase transition is observed in the bottom panel of Fig. 6.12 (a). A closer view of the droplet size shows that at $t \sim 25$ ms, σ_r starts to increase and the system behaves like the $\delta a > 0$ gas. To support this scenario, Fig. 6.12 (b) depicts the radial size and atomic density as a function of atom number. For $\delta a < 0$ (blue circles) we observe that both size (top panel) and density (bottom panel) remain constant at large N. For decreasing atom number, we observe a point

where the size diverges, and the density drops abruptly. This indicates a liquid-to-gas transition, which takes place at the critical atom number N_c. Below this value, the attractive gas is still stabilized by quantum fluctuations (LHY gas) but expands due to kinetic effects, similarly to the repulsive mixture ($\delta a > 0$, red circles).

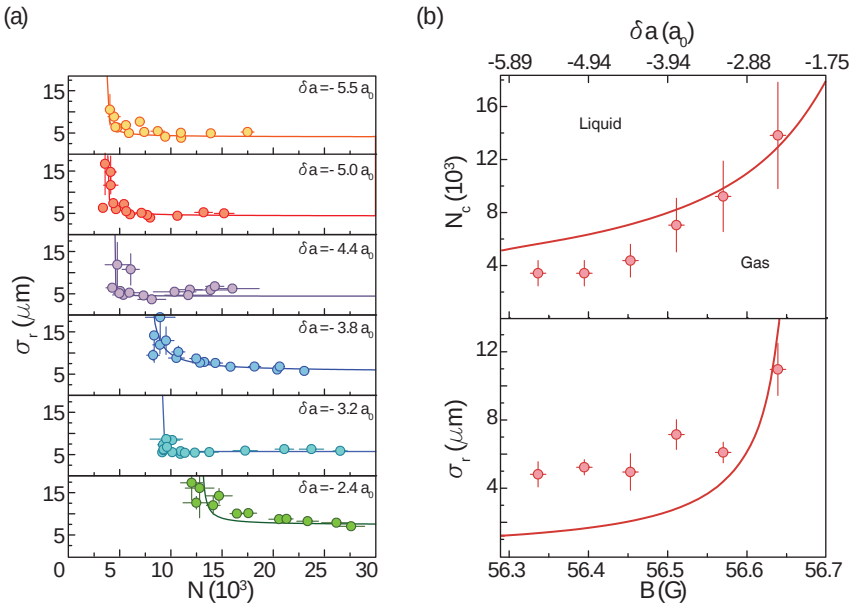

Figure 6.15: Liquid-to-gas phase diagram.(a) Radial size of the mixture σ_r as a function of atom number N for different magnetic fields B, from strong to weak attraction (top to bottom). The critical atom number N_c increases as attraction decreases. Solid lines display the phenomenological fit $\sigma_r(N) = \sigma_0 + A/(N - N_c)$ used to locate the liquid-to-gas phase transition. (b) N_c (top panel) and σ_r for fixed $N = 1.5(1) \times 10^4$ (bottom panel) as a function of B. The upper horizontal axis shows the corresponding values of δa. Solid lines are the predictions of an extended Gross-Pitaevskii model without fitting parameters (see main text). Error bars for σ_r correspond to the standard deviation of 10 independent measurements. If not displayed, error bars are smaller than the size of the symbol. Error bars for B and N show the systematic uncertainty of the corresponding calibrations.

The liquid-to-gas transition is also expected to depend on δa and N, as sketched in the homogeneous phase diagram computed in Fig.

6.5 (b). We expect to have similar phase diagram but the critical number N_c is modified in the presence of the trapping potential (see section 6.6.4). We explore the phase diagram by tuning the interaction strengths with magnetic field B. Fig. 6.15 displays the measured size as a function of the atom number for magnetic fields corresponding to δa between $-5.5(1)\,a_0$ and $-2.4(1)\,a_0$.

The critical number N_c shows a strong dependence on the magnetic field. The top panel of Fig. 6.15 (b) presents our experimental determination of the phase transition line. We observe that N_c increases when the attraction decreases, confirming that weakly bound droplets are more susceptible to kinetic effects and require a larger atom number to remain self-bound. Fig.6.15 (a) also yields the droplet size as a function of atom number and magnetic field. In the bottom panel of Fig. 6.15 (b) we display the measurements obtained at a fixed atom number $N = 1.5(1) \times 10^4$, always larger than N_c for our interaction regime. As expected, the droplet size decreases as the attraction increases.

6.6.4 *Theoretical model in the presence of a trap*

To compare our experimental measurements, we provide a simplified theoretical model similar to the one presented in section 2.5. Here in addition to the effective low-energy theory explained before we include the experimental confinement along the vertical direction $V_{\text{trap}} = \frac{1}{2}m\omega_z^2 z^2$.

One assumption in our model is the form of LHY energy term. Since the corresponding harmonic oscillator length a_{ho} typically exceeds ξ_s by a factor of three, the Lee-Huang-Yang term has been calculated assuming the Bogoliubov spectrum of a homogeneous three-dimensional system. Thus, it does not take into account finite-size or dimensional crossover effects due to the presence of the vertical harmonic confinement. The energy density functional reads

$$\mathcal{E} = \mathcal{E}_{\text{kin}} + \mathcal{E}_{\text{trap}} + \mathcal{E}_{\text{MF}} + \mathcal{E}_{\text{LHY}} \tag{6.9}$$

We compare the results of the variational technique with a numerical solution of the extended Gross-Pitaevskii equation presented in Eq. 2.55 (this calculation was performed by P. Cheiney and B. Naylor). We observe that even for the densest droplets realized in the experiment, their density profile is well approximated by a Gaussian. Indeed, for the atom numbers and magnetic fields considered in the experiment, the bulk density of the liquid is not reached, and the droplet size is comparable to the surface thickness [3]. As depicted in Fig. 6.16, we find excellent agreement between the two approaches, with deviations that remain well below the experimental error bars for the complete parameter range explored in the measurements.

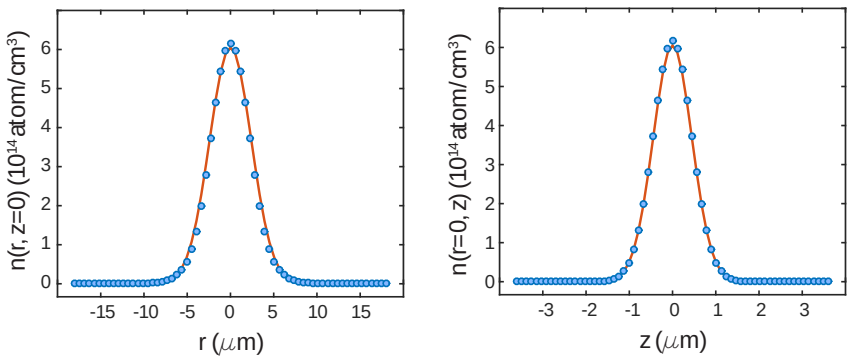

Figure 6.16: Theoretical density profiles. Density profiles predicted by the extended Gross-Pitaevskii model along the radial (left panel) and vertical (right panel) directions, for $N = 25000$ and $B = 56.57$ G ($\delta a = -3.20\, a_0$). Blue circles: full numerical solution. Red lines: variational calculation with a Gaussian ansatz. The excellent agreement between both, even for the densest droplets realized in the experiment, justifies the Gaussian fitting function used to analyze the measured density profiles (see data analysis section).

Therefore the experimental points in Fig. 6.15 are compared for simplicity (computing power) with the variational predictions. For the top panel of Fig. 6.15 (b) the critical atom number is obtained by applying to the theoretical $\sigma_r - N$ curves the same phenomenological fit used for the experimental data. We have verified that including the residual

anti-confinement of the optical lattice does not modify the theoretical predictions appreciably.

6.6.5 *Discussion of the results*

In Fig.6.15 (b) we compare the experimental results to the predicted critical atom number and droplet size (solid lines). We find qualitative agreement for the complete magnetic field range with no adjustable parameters. In the weakly attractive regime, the agreement is even quantitative, similarly to the dipolar Erbium experiments of ref. [139]. In contrast, when increasing the effective attraction, the droplets are more dilute than expected. In particular, their size exceeds the theoretical predictions by up to a factor of three. This is almost one order of magnitude larger than our measured imaging resolution, excluding finite-resolution effects. Furthermore, the critical atom number is a factor of two smaller than the theoretical value. Interestingly, a similar discrepancy was reported for dipolar Dysprosium droplets, with a critical atom number one order of magnitude smaller than expected [141]. In this case, the deviation was attributed to insufficient knowledge of the background scattering length. This explanation seems unlikely in the case of potassium, where excellent interaction potentials are available [77, 120, 167]. Furthermore, for deeply bound droplets the role of the magnetic dipole-dipole interactions (computed similarly to ref. [144]) can be neglected. We conclude that none of these effects seem to explain the discrepancies between our model and the experimental measurements.

Other physical mechanisms might be responsible for the diluteness of the observed droplets. Although our system is three-dimensional, the confinement along the vertical direction might affect the Lee-Huang-Yang energy, modifying its density and interaction dependence or introducing finite-size effects. A description of quantum fluctuations in the dimensional crossover between two and three dimensions is challenging and goes beyond the scope of this thesis. Nevertheless, theoret-

ical studies have been performed just before submission of this thesis in order to understand the scaling of the LHY term in the dimensional crossover [168, 169]. Comparisons between these models and the experiment will be performed in the near future.

Interestingly, the almost perfect cancellation of the mean-field energy could reveal other corrections besides the Lee-Huang-Yang term. Higher-order many-body terms might play a role, as proposed in ref. [134] for single-component systems. Taking them into account requires a good knowledge of the three-body interaction parameters of the mixture, which are non-universal and difficult to estimate in our interaction regime. Alternatively, our results could be compared to *ab initio* quantum Monte Carlo simulations, as recently performed in ref. [146]. Given the ultra-dilute character and simple microscopic description of our system, a direct comparison to different theoretical approaches could give new insights on yet unmeasured many-body effects.

6.6.6 *ICFO and LENS quantum droplets*

During the experimental realization of our quantum droplets, related experiments were performed by LENS group [67]. This is an interesting result because it allows corroborating in an independent way the existence of quantum droplets in atomic mixtures.

In this complementary work, they have studied the formation of spherical quantum droplets using the same atomic mixture and magnetic field range as the one presented in this chapter. In their case, they have studied the formation of this self-bound state in the "absence" of external confinement. To achieve this, the atoms were levitated optically using a fast modulated optical potential that creates an optical gradient large enough to compensate for gravity. In this aspect, their system is similar to the one presented in the original proposal.

Similar to our results they have observed the dynamics of the Bose-Bose mixture and how it remains self-bound for different propagation times. As expected, for a critical atom number the droplet dissociates

into a gas, giving rise to the liquid-to-gas transition. In addition to these results, they have measured the spin ratio that in principle minimizes the energy of the mixture $N_1/N_2 = \sqrt{a_{22}/a_{11}}$. In our case we discuss this aspect in chapter 7.

In terms of experimental sequence, we perform an adiabatic preparation of the system. We ramp down slowly the magnetic field from $\delta a > 0$ to $\delta a < 0$ while removing the z optical dipole trap. In their case, the droplet is prepared by quenching the system. A BEC in state $\uparrow$ is prepared in a magnetic field range where $\delta a < 0$, then a RF pulse transfer 50% of the atoms to state $|\downarrow\rangle$.

In both preparations schemes, if the initial size of the system is matched with the size of the droplet, collective modes should not be observed. However, in both experiments, we do observe a small oscillation around the equilibrium size of the droplet. This implies that the system is highly sensitive to excitations.

Regarding the geometry, the main difference between the two systems is the vertical confinement that we imposed on the atoms to levitate them. Although this should not affect the results [4], we observe discrepancies in the critical atom number and size for larger values of δa. In their case this discrepancy is small and fits with the theory within error bars. This is an interesting result because probably the LHY energy in our case is slightly modified due to the presence of the trap.

To summarize, both experiments present a smoking gun of the liquid-to-gas phase transition in Bose-Bose mixtures. In two distinct scenarios, different experimental sequences and analysis of data both converge to similar results. They reveal the existence of BMF effects that stabilizes the system into the **quantum liquid droplet**.

4 Remember that the healing length associated to each mode in our systems is larger than the confinement, therefore we are in the 3D regime

7

BRIGHT SOLITON TO QUANTUM DROPLET TRANSITION

Attractive Bose-Einstein condensates can host two types of macroscopic self-bound states: bright solitons and quantum droplets. Here, we investigate the connection between them with a Bose-Bose mixture confined in an optical waveguide. We show theoretically that, depending on atom number and interaction strength, solitons and droplets can be smoothly connected or remain distinct states coexisting only in a bi-stable region. We measure their spin composition, extract their density for a broad range of parameters and map out the boundary of the region separating solitons from droplets.

This chapter is partially published in Ref. [136].

P. Cheiney, C. R. Cabrera, J. Sanz, B. Naylor, L. Tanzi, and L. Tarruell, Phys. Rev. Lett. **120**, 135301 (2018).

7.1 INTRODUCTION

In this chapter we address a fundamental question that was raised when performing the experiments presented in the previous chapter: The difference between bright solitons and quantum droplets. Both states are self-bound solutions that appear in an attractive BEC, therefore it is important to reveal and clarify the difference between the two systems. Setting aside the semantic problem, we show in this chapter how the two systems are stabilized by different mechanisms, however in some regimes of parameters the two solutions can connect to each other.

7.2 BRIGHT SOLITONS VS QUANTUM DROPLETS

Bose-Einstein condensates (BECs) with attractive mean-field interactions constitute ideal model systems to explore in the same setting self-bound states stabilized by repulsive forces of different classes. On the one hand, bright solitons in optical waveguides have been observed with ^{7}Li [26–28], ^{85}Rb [29–31] and ^{39}K atoms [32]. These matter-wave analogs of optical solitons are stabilized against collapse by the dispersion along the unconfined direction, which is a (single-particle) kinetic effect. On the other hand, quantum droplets, as explained in chapter 6 are stabilized due to the contribution of quantum fluctuations.

Bright solitons and quantum droplets are *a priori* distinct states which exist in very different regimes. Solitons require the gas to remain effectively **one-dimensional**, which limits their maximal atom number [21, 25, 170]. In contrast, droplets are three-dimensional solutions that exist even in free space and require a minimum atom number to be stable [3, 66, 139, 141, 143, 149]. Up to now, quantum droplet experiments focused exclusively on systems where solitons were absent, enabling unambiguous identification of the droplet state. Therefore, they could not provide any insights on their connections to solitons. Here we address such question.

7.3 ATTRACTIVE BOSE-BOSE MIXTURE IN AN OPTICAL WAVEGUIDE

As explained in chapter 2, a pure BEC of ultracold atoms can be described in terms of the Gross-Pitaevskii equation. In quasi 1D systems, Bose-Einstein condensates support a self-bound solution a bright soliton. This stable state can be predicted for either single or two component condensates using only a mean field description.

In chapter 6, we have discussed how in a Bose-Bose mixture the presence of quantum fluctuations can modify strikingly the predictions using only MF theories. In particular, in a 3D system, we have explored exotic self-bound states called quantum droplets.

Here we explore the physics of Bose-Bose mixtures trapped in an optical waveguide. In such geometry (see Fig. 7.1 (a)), we explore the regime where the strong radial trapping potential allows us to freeze the transversal excitations and explore, at first sight, the dynamics only in the longitudinal direction.

Due to the non-negligible presence of quantum fluctuations, here we can expect to observe an interplay between the bright solitons and quantum droplets.

Using our extended GPE presented before (see Eq. 2.21), it is possible to describe the properties of an attractive Bose-Bose mixture in an optical waveguide.

7.3.1 *Two-component bright soliton and quantum droplets*

The energy density functional of a Bose-Bose mixture in an optical waveguide is similar to the one presented in Eq. 6.9:

$$\varepsilon = \overbrace{\varepsilon_{\text{kin}} + \varepsilon_{\text{trap}} + \underbrace{\varepsilon_{\text{MF}}}_{\text{Quantum droplets}}}^{\text{Bright solitons}} + \varepsilon_{\text{LHY}} \tag{7.1}$$

where the brackets denote the terms involved in the stabilization of bright solitons and quantum droplets. Here the trapping potential is given by the one in Eq. 2.31, however we neglect for simplicity the weak longitudinal confinement:

$$V(r) = \frac{1}{2} m\omega_{\perp} r^2. \tag{7.2}$$

Taking into account quantum fluctuations there is an interplay of the different energy terms and not only bright solitons exist but also quantum liquid droplets. In the regime $\delta a < 0$, these three different terms of different origins compete (interaction strength or atom number) and they could give rise to the following solutions:

- *"Bright-bright" solitons*. Similar to the one-component bright solitons explained before ($\mathcal{E}_{\mathrm{MF}} \sim \mathcal{E}_{\mathrm{kin}}$), but including two components.
- *Quantum droplets*. Self-bound solutions that do not depend on the characteristic length scale imposed by the harmonic oscillator length of the trap ($\mathcal{E}_{\mathrm{MF}} \sim \mathcal{E}_{\mathrm{LHY}}$).
- *Soliton-to-droplet like state*. Regime where the three energy scales relevant to the system are comparable ($\mathcal{E}_{\mathrm{MF}} \sim \mathcal{E}_{\mathrm{LHY}} \sim \mathcal{E}_{\mathrm{kin}}$).

7.3.2 *Full numerical simulation and variational ansatz*

To clarify the nature of the self-bound states and their relation to the well-known bright solitons and quantum droplet limits, we perform a theoretical analysis of the system. We compute the ground state of the system by solving Eq. 7.1 numerically. We employed two different methods: full numerical simulation of the eGPE (the full numerical simulation has been performed by P. Cheiney, B. Naylor) or minimization of the energy through a variational ansatz. The two methods provide different information that allows to understand the different

features and interplay of the different energy terms presented in Eq. 7.1.

The simulations are performed using the effective eGPE introduced for a Bose-Bose mixture of ^{39}K previously (see Eq. 6.3). Here in addition we confine the system with a cigar shape potential with a radial trapping frequency $\omega_\perp = 2\pi \times 109$ Hz[1]. The mixture is assumed to be in the same internal degrees of freedom as in the one used in chapter 6. The scattering length for the different terms ($a_{\uparrow\downarrow}$, $a_{\uparrow\uparrow}$, $a_{\downarrow\downarrow}$) and δa is calculated by A. Simoni (private communication) from the ^{39}K model interaction potentials of refs. [77, 167]. Notice that we have changed the axis definition compared to previous chapters in order to simplify the calculation (see Fig. 7.1).

Full numerical simulation

We find the stationary solutions numerically using the three-dimensional MATLAB toolbox of ref. [171]. For each magnetic field B we first solve the eGPE for $N = N_\uparrow + N_\downarrow = 1000$, using as a initial guess for ϕ a three-dimensional Gaussian function of size a_{ho}. We subsequently compute the solution for increasing values of N, choosing as initial guess the function ϕ determined in the previous step. The phase diagram of the system is presented in Fig. 7.1 (b). The peak density n_0 is depicted as a function of the total atom number $N = N_\uparrow + N_\downarrow$ and magnetic field B (equivalently, interaction strength δa). For large attraction we find two distinct behaviors: a high-density solution ($n_0 \sim 10^{16}$ atoms/cm^3) for large N, and a low-density one ($n_0 \sim 10^{13}$ atoms/cm^3) for small N.

In between, the gray region corresponds to a bi-stable regime where both solutions are possible. A discontinuity of the density signals its boundaries. This behavior disappears above a critical magnetic field

1 This trapping frequency is chosen such that we can compare the simulations with further explained experiments.

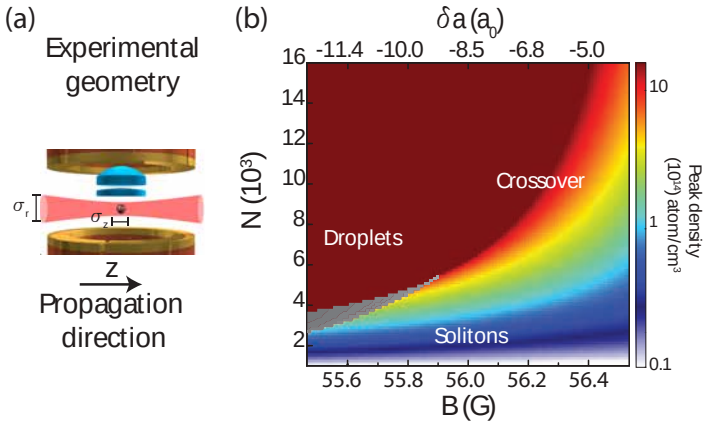

Figure 7.1: Soliton-to-droplet density diagram. (a) Experimental geometry. The atoms experience a radial trapping potential while they propagate free of confinement along z direction. Notice that we have changed the axis definition compared to previous chapters in order to simplify the calculation. (b) Ground state peak density as a function of atom number N and magnetic field B computed numerically from the effective single-component eGPE in the presence of a cigar-shaped potential. Solitons and droplets are distinct solutions, which coexist in a bi-stable region (shaded area) and become smoothly connected in the crossover above $B_c \sim 55.8$ G.

($B_c \sim 55.85$ G, for the confinement given above). Beyond, the system supports a single solution whose density increases progressively with N. This situation is analogous to a quantum ($T = 0$) first-order liquid-to-gas phase transition: the bi-stable regime contains metastable regions surrounding a transition line, and a crossover region appears above B_c. The B_c where the critical point appears depends on $\omega_\perp$, in fact, the atom number required to enter in the bi-stable regime is larger by reducing $\omega_\perp$. In the limit $\omega_\perp \longrightarrow 0$ the soliton solution disappears and the phase diagram of Fig. 6.5 is recovered.

For all the parameters explored in the experiment (see section 7.4), we find that ϕ is well approximated by a Gaussian. Therefore we use our variational technique introduced in chapter 2 and chapter 6 to gain further insight into the properties of the system.

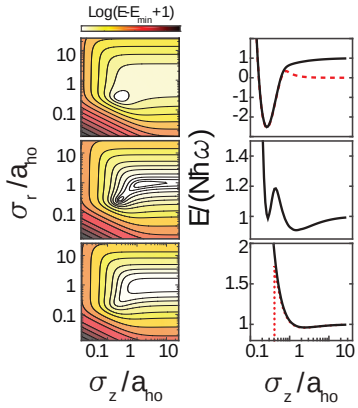

Figure 7.2: Energy E of the Gaussian ansatz as a function of the radial σ_r and longitudinal σ_z sizes, for $B = 55.6$ G and $N = 9000$ (top, droplet), $N = 4000$ (center, bi-stable region) and $N = 2500$ (bottom, soliton). Right panel: one-dimensional cuts along σ_z, for σ_r minimizing E. All panels, solid lines: complete model; top panel, dashed line: no optical waveguide; bottom panel, dotted line: no quantum fluctuations.

Variational Ansatz

In this geometry the appropriate Gaussian ansatz is:

$$\phi = \sqrt{n_0} \mathrm{e}^{-r^2/2\sigma_r^2 - z^2/2\sigma_z^2}.$$

It yields the following functional for the total energy of the mixture $E = \int \mathrm{d}\mathbf{r}\, \mathcal{E}$:

$$\begin{aligned}\frac{E(\sigma_r,\sigma_z)}{N\hbar\omega} &= \frac{1}{N\hbar\omega}\left(E_{\rm kin}+E_{\rm trap}+E_{\rm MF}+E_{\rm LHY}\right)\\ &= \frac{1}{4}\left(\frac{2a_{\rm ho}^2}{\sigma_r^2}+\frac{a_{\rm ho}^2}{\sigma_z^2}\right)+\frac{1}{4}\left(\frac{2\sigma_r^2}{a_{\rm ho}^2}\right)\\ &+ \frac{1}{\sqrt{2\pi}}\frac{Na_{\rm ho}^3}{\sigma_r^2\sigma_z}\left(\frac{2\sqrt{a_{\downarrow\downarrow}/a_{\uparrow\uparrow}}\delta a}{\left(1+\sqrt{a_{\downarrow\downarrow}/a_{\uparrow\uparrow}}\right)^2 a_{\rm ho}}\right)\\ &+ \sqrt{\frac{2}{5}}\frac{512}{75\pi^{7/4}}\frac{N^{3/2}a_{\rm ho}^{9/2}}{\sigma_r^3\sigma_z^{3/2}}\left(\frac{\sqrt{a_{\uparrow\uparrow}a_{\downarrow\downarrow}}}{a_{\rm ho}(1+\sqrt{a_{\downarrow\downarrow}/a_{\uparrow\uparrow}})}\right)^{5/2}\\ &\quad F\left(1,\frac{a_{\uparrow\downarrow}^2}{a_{\uparrow\uparrow}a_{\downarrow\downarrow}},\sqrt{\frac{a_{\downarrow\downarrow}}{a_{\uparrow\uparrow}}}\right). \end{aligned} \tag{7.3}$$

In fact, by replacing the expression presented in Eq. 2.58, we recover at the mean-field level the behaviour of a single-component condensate of scattering length a [4]. For $\delta a < 0$ Eq. (7.3) contains a composite bright soliton solution stabilized by the balance between $E_{\rm kin} > 0$ and $E_{\rm MF} < 0$. In the mean-field approximation ($E_{\rm LHY} = 0$), we can define a collapse criterion similar to the one defined in Eq.2.29

$$N_c = 0.6268\frac{\left(1+\sqrt{a_{\downarrow\downarrow}/a_{\uparrow\uparrow}}\right)^2 a_{\rm ho}}{2\sqrt{a_{\downarrow\downarrow}/a_{\uparrow\uparrow}}|\delta a|},$$

where the pre-factor has been computed numerically using the same MATLAB toolbox but without including the LHY energy. This prefactor can be in principle computed using the variational ansatz, however, is known that this calculation overestimates the soliton stability[2] [21].

Using the variational ansatz we study in particular the bistable region (gray region in Fig. 7.1). In Fig. 7.2 we display the energy landscapes obtained at a fixed magnetic field $B = 55.6$ G $< B_c$. For small

2 The variational calculation predicts a prefactor equal to 0.7598 while the numerical simulation 0.6268 as we already explain in chapter 2.

values of N (bottom row), the energy has a single minimum corresponding to a dilute and elongated cloud: a bright composite soliton. Its radial size σ_r corresponds to the harmonic oscillator length a_{ho} and its longitudinal size σ_z and energy E are similar to those obtained in a mean-field treatment without quantum fluctuations (bottom right panel, red dotted line). For large values of N (top row) the minimum corresponds to a dense and isotropic solution with $\sigma_r \ll a_{\text{ho}}$: a quantum liquid droplet. Its properties are not affected by the trapping potential, and it exists in its absence (top right panel, red dashed line). In the bi-stable region (central row) both composite bright solitons and liquid droplets exist simultaneously. Above the critical magnetic field, B_c a crossover takes place, with a single solution which evolves from soliton-like to droplet-like upon increasing the atom number. A related behavior, involving a bistable region and a crossover regime, has been studied in harmonically trapped dipolar gases [139, 141, 149, 172]. In this case, the low- and high-density solutions correspond to a BEC and a quantum droplet.

7.3.3 *Dimensional crossover: From quasi-1D to 3D*

Using the variational technique we have observed how the solitons and droplets are two different solutions. We find that depending on atom number, interaction strength and confinement, solitons and droplets can be smoothly connected or remain distinct states coexisting only in the bi-stable region.

In chapter 2 we have shown that single component quasi-1D solitons collapse for a critical atom number that depends on the harmonic oscillator length and the s-wave scattering length. This collapse is suppressed in the two-component case due to the presence of the LHY correction. Here instead of the collapse, the droplet solution appears.

In fact, on this system we are exploring a dimensional crossover that goes from quasi-1D to 3D. In Fig. 7.3 we show the values of σ_r (red) and σ_z (blue) that minimize the functional presented in Eq. 7.3.

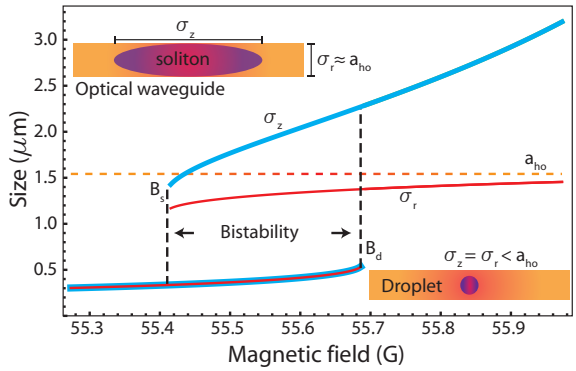

Figure 7.3: For an atom number $N = 3000$, we explore the bistability region between solitons and droplets. We observe that preparing the system in the soliton regime (top branch) for a given magnetic field B_s there is a discontinuity in the radial and longitudinal size of the soliton (black dashed line). The system jumps to a phase where both directions of the system are isotropic and below the size of the harmonic oscillator (orange dashed line). By preparing the system on the bottom branch (quantum droplet), for a magnetic field B_d, the system goes back to the soliton phase. An hysteresis loop is observed due to the soliton-to-droplet transition.

For a fixed atom number ($N = 3000$) we observe in the top branch how as a function of the magnetic field, σ_z reduces its size until it becomes comparable to the size of the harmonic oscillator a_{ho} (orange dashed line). As mentioned before, in the soliton regime this system is essentially quasi-1D and therefore $\sigma_r \approx a_{\text{ho}}$. For a given magnetic field there is a discontinuity on both sizes (black dashed line), and then the system jumps to the bottom branch where the size of the self-bound solution is isotropic and below the size of the harmonic oscillator length ($\sigma_z = \sigma_r < a_{\text{ho}}$).

This behavior implies the following: In a single component soliton, the system collapses when both sizes go below the harmonic oscillator length (the bottom branch does not exist). There the system goes from the quasi-1D regime (imposed by the confinement of the harmonic trap) to a 3D situation where the length scale of the external potential is larger than the characteristic length scale of the system. In these

circumstances, the mean field energy becomes comparable to the kinetic energy term, and therefore a bright soliton behaves similarly to an attractive 3D homogeneous BEC: the system collapses.

In contrast, composite bright solitons are protected against collapse due to the presence of the LHY energy. When the system goes below the size of the harmonic oscillator length, instead of collapsing, the system becomes isotropic and self-bound. The system at this moment is not affected by the length scale imposed by the trap. In analogy to the droplets presented in the previous chapter, it is a fully 3D system mainly stabilized by the LHY contribution.

The insets presented in Fig. 7.3 sketch the dimensional crossover. The top inset shows a soliton propagating in an optical waveguide with a radial size given by the trap. In the droplet phase (bottom inset), the size of the system is below the length scale of the trap (a_{ho}). The latter implies that it is effectively a self-bound state in the absence of a trapping potential: a **quantum droplet**.

One last remark. In Fig. 7.3 we observe that the transition from soliton-to-droplet appears at different magnetic fields depending on the initial state and whether the magnetic field is decreased or increased. This sort of hysteresis loop is associated to phase transitions where metastable states are present. Such soliton-to-droplet phase transition is discussed in detail in section 7.4.5. A similar hysteresis loop is predicted in the dipolar BEC-to-quantum droplet transition [137, 149].

7.4 EXPERIMENTS WITH BRIGHT SOLITONS AND QUANTUM DROPLETS

7.4.1 *Experimental sequence: observation of self-bound states*

Similar to the experiments with quantum droplets in Chapter 6, we perform experiments with a mixture of ^{39}K BECs in Zeeman states $|\uparrow\rangle \equiv |m_F = -1\rangle$ and $|\downarrow\rangle \equiv |m_F = 0\rangle$ of the $F = 1$ hyperfine manifold. Here instead, the lattice potential presented before is replaced by a 1064 nm red detuned dipole trap propagating through the "W-direction" (see inset Fig. 7.5.). This potential acts as an optical waveguide. The radial trapping frequency is $\omega/2\pi = 109(1)$ Hz. For our experimental parameters, this is the lowest value needed to levitate the mixture against gravity.

The interactions are tuned *via* magnetic Feshbach resonances and parameterized by the intra- and inter-component scattering lengths $a_{\uparrow\uparrow}, a_{\downarrow\downarrow} > 0$ and $a_{\uparrow\downarrow} < 0$ [167]. We use the same magnetic window presented in section 6.4. In contrast to the quantum droplet experiments presented in Chapter 6, here we extend the range in which the phase diagram is explored. We scan the magnetic field range from $B = 55 - 57.5$ G, in the vicinity of a Feshbach resonance for state $|\downarrow\rangle$. In accordance with the parameter $\delta a = a_{\uparrow\downarrow} + \sqrt{a_{\uparrow\uparrow} a_{\downarrow\downarrow}}$, the overall mean-field interaction goes from positive to negative values ($\delta a = 0$ corresponds to $B = 56.84$ G). The intra- and inter-component scattering lengths on this range for the different Zeeman states are presented in Fig. 7.4.

Experimental sequence

The experiment starts with a pure BEC in state $|\uparrow\rangle$ confined in a crossed optical dipole trap of frequencies

$$\omega_{x,y,z}/2\pi = [119(1), 109(1), 49(1)]\,\text{Hz}.$$

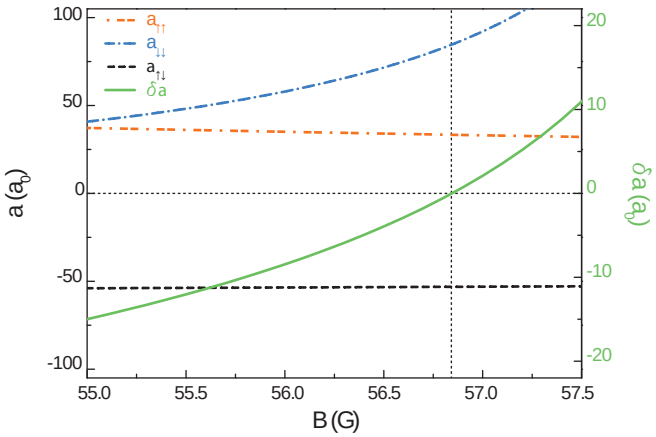

Figure 7.4: Scattering lengths $a_{\uparrow\uparrow}$, $a_{\downarrow\downarrow}$, $a_{\uparrow\downarrow}$, and parameter $\delta a = a_{\uparrow\downarrow} + \sqrt{a_{\uparrow\uparrow} a_{\downarrow\downarrow}}$ (expressed in units of the Bohr radius a_0) as a function of magnetic field B for a ^{39}K mixture in states $|\uparrow\rangle \equiv |F = 1, m_F = -1\rangle$ and $|\downarrow\rangle \equiv |F = 1, m_F = 0\rangle$.

A radio-frequency (RF) pulse is used to prepare a controlled mixture of the two components. The pulse is performed at $B \sim 57.2$ G, where $\delta a > 0$ and the system is in the miscible regime [50]. Subsequently, the magnetic field is ramped down at a constant rate of 11.8 G/s while reducing the longitudinal confinement. The latter is removed in 5 ms at the final magnetic field, leaving the system unconfined along the z direction (the beam creates a longitudinal confinement of frequency $\omega_z \lesssim 2\pi \times 1$ Hz along its propagation direction. This value is small compared to the radial confinement and therefore is neglected).

Fig. 7.5 (b) shows typical *in situ* images of the time evolution of the mixture after release in the optical waveguide. Fig. 7.5 (a) displays its longitudinal size σ_z as a function of magnetic field, for three different evolution times. In the repulsive regime ($\delta a > 0$) σ_z increases with δa, reflecting the increase of the released energy of the gas. In contrast, in the attractive regime ($\delta a < 0$) the absence of expansion indicates the existence of self-bound states. Experimentally, we only observe this behavior below $\delta a \sim -2a_0$, where a_0 denotes the Bohr radius. As in

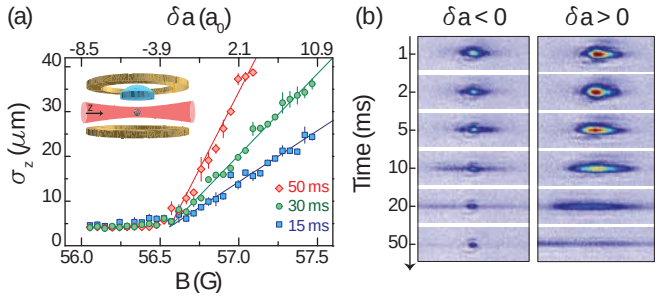

Figure 7.5: Self-bound states. (a) Gaussian $1/e$ width σ_z of the mixture as a function of the magnetic field B (corresponding to different values of δa), for various evolution times after release in the optical waveguide (inset). For $B < 56.6$ G the system becomes self-bound and the value of σ_z saturates our imaging resolution. Solid lines are linear fits to the data in the expanding regime and error bars denote the standard deviation of 10 independent measurements. (b) Typical *in situ* images for increasing evolution times, corresponding to a self-bound state (expanding gas) in the attractive (repulsive) regime with $\delta a < 0$ ($\delta a > 0$) and initial atom number $N \sim 7000$ ($N \sim 30000$).

ref. [32], we attribute this effect to the initial confinement energy of the system.

7.4.2 *Spin composition*

The observed self-bound states are intrinsically composite objects, involving both $|\uparrow\rangle$ and $|\downarrow\rangle$ atoms. To probe this aspect, we prepare mixtures of different compositions by varying the RF pulse time τ. Large population imbalances between the two states result in bi-modal density profiles in the *in situ* images, see left panel of Fig. 7.6 (a). They consist of a self-bound state surrounded by a wider and expanding cloud of atoms of the excess component. We find that the fraction of self-bound atoms is maximized for an optimal pulse time, see the central panel of Fig. 7.6. We do not perform spin-resolved in situ imaging due to the electronic spin composition of the states at high magnetic field (see section 6.5.4).

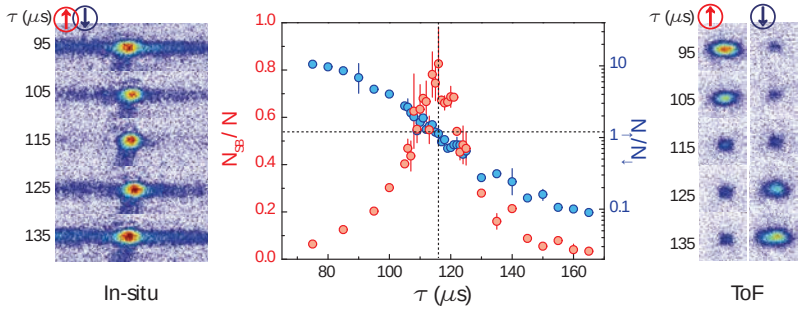

Figure 7.6: Spin composition. *In situ* images of the mixture for various RF pulse times τ and $B = 56.35(1)$ G. Away from an optimal value the density profile is bi-modal, with a self-bound state surrounded by atoms of the excess component. Central panel: fraction of self-bound atoms N_{SB}/N (red squares) and spin composition $N_\uparrow/N_\downarrow$ (blue circles) as a function of τ. Error bars denote the standard deviation of 4 measurements. Right panel: corresponding time-of-flight (ToF) Stern-Gerlach analysis of the spin composition.

To determine its spin composition we perform a complementary set of measurements, modifying the detection sequence. We dissociate the self-bound state by increasing the magnetic field to the repulsive regime ($B \sim 57.3$ G) in 1 ms. When the system is dissociated, we do not observe losses after ToF and therefore absorption imaging can be used. This technique has been used in ref. [137] to extract the atom number in the droplet phase.

We then measure the atom number per spin component $N_\uparrow$ and $N_\downarrow$ *via* Stern-Gerlach separation during time-of-flight expansion, see right panel of Fig. 7.6. We extract the optimal composition as a function of B by combining the *in situ* and time-of-flight measurements, see Fig. 7.7. The interaction energy of the system is minimized by maximizing the spatial overlap of the two components [3, 173]. The theoretical prediction assuming that both occupy the same spatial mode yields $N_\uparrow/N_\downarrow = \sqrt{a_{\downarrow\downarrow}/a_{\uparrow\uparrow}}$ (solid line), which is in fair agreement with the data.

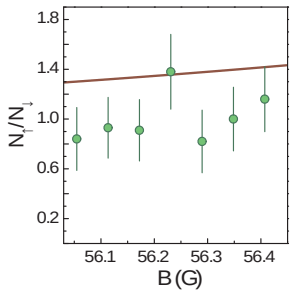

Figure 7.7: Spin composition. Optimal ratio $N_\uparrow/N_\downarrow$ as a function of magnetic field B. Error bars correspond to the confidence interval of the fit. The solid line depicts the theoretical prediction $N_\uparrow/N_\downarrow = \sqrt{a_{\downarrow\downarrow}/a_{\uparrow\uparrow}}$.

7.4.3 *Exploring the phase diagram*

We explore experimentally the phase diagram presented in Fig. 7.1 by preparing self-bound states at different interaction strengths, starting from the high N regime. We observe that their atom number decreases in time due to inelastic processes, see Fig. 7.8). For our experimental parameters these are completely dominated by three-body recombination in the $\downarrow\downarrow\downarrow$ channel (see section 6.6.2).

We model the decay of the self-bound atom number using the simplified rate equation $\dot{N}/N = -K_3^{\text{eff}}\langle n^2\rangle$, where $\langle n^2\rangle$ is the total mean square density and K_3^{eff} an effective three-body loss coefficient presented in section 6.6.2. The model assumes that the $|\downarrow\rangle$ losses are accompanied by the expulsion of $|\uparrow\rangle$ atoms from the self-bound state in order to maintain the value of $N_\uparrow/N_\downarrow$ constant. For more details see Appendix C.1.

Similarly to recent experiments on dipolar ^{166}Er droplets [139], we extract the density of the self-bound state by measuring the decay of its atom number. The later allows us to map out the density as a function of N from a single decay curve. Moreover, this technique allows circumventing the limitations imposed by the imaging resolution. The harmonic oscillator length imposes the size of a bright soliton in the

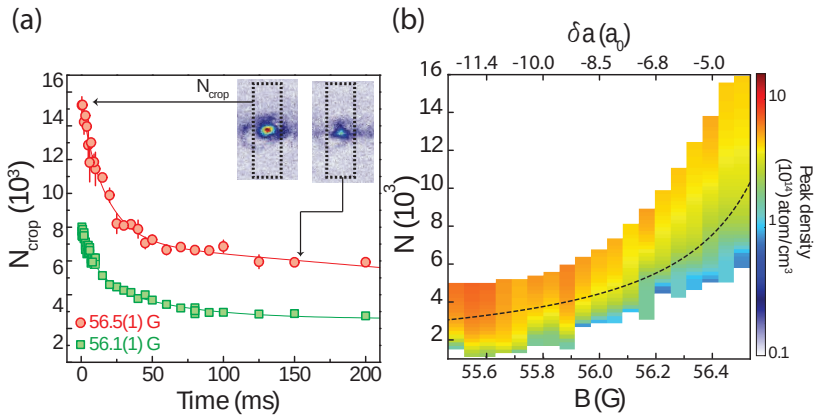

Figure 7.8: (a) Peak density extracted from the decay of the self-bound atom number. Self-bound states are stabilized by beyond mean-field effects well above the mean-field collapse threshold for composite bright solitons (dashed line). (b) Evolution of the self-bound atom number N_{crop}, determined from the zeroth moment of the cropped region (insets), as a function of time t. Solid lines: empirical fit for extracting the decay rate. Error bars: standard deviation of 4 measurements.

radial direction of the optical dipole trap ($\sim$ 1.5 μm). This value is below our imaging resolution. Note that on these measurements our resolution is worse than the one reported in the previous chapter. This is due to a misalignment of the objective.

We determine the atom number of the self-bound states from the *in situ* images quantitatively by evaluating the zeroth moment of the images $N = M_{00} = \sum_{x,z} n_c(x,z)$, which is independent of lens aberrations [100]. In order to count only the self-bound atoms we crop the images around the maximal column density and extract N from this observation region (see inset Fig. 7.8 (a)). We have verified that increasing the crop size in the direction perpendicular to the waveguide does not modify the results. The longitudinal crop size needs to be adjusted more carefully to avoid counting excess atoms that are expanding in the waveguide. We fix its value by comparing the atom number extracted from *in situ* images with no excess component with

time-of-flight measurements. We find that for all the data, possible errors in N associated to incorrect choices of the longitudinal crop size remain $< 10\%$, below the systematic error of the N calibration (25%).

The Fig. 7.8 (b) displays the determined peak densities as a function of atom number and magnetic field. Interestingly, a large fraction of the measurements lie well above the mean-field bright soliton collapse threshold (black dashed line). At the theoretical optimum $N_\uparrow/N_\downarrow$, as presented in section 7.4, it corresponds to the condition

$$N_c = 0.6268\, a_{\mathrm{ho}} \left(1 + \sqrt{a_{\downarrow\downarrow}/a_{\uparrow\uparrow}}\right)^2 / \left(2|\delta a|\sqrt{a_{\downarrow\downarrow}/a_{\uparrow\uparrow}}\right).$$

The absence of collapse in our measurements shows the existence of a stabilizing beyond mean-field mechanism.

In the deeply bound regime, the measured peak densities agree only qualitatively with the eGPE predictions. The discrepancies might stem from two sources. First, we have considered that the spin composition of the system adjusts to $N_\uparrow/N_\downarrow = \sqrt{a_{\downarrow\downarrow}/a_{\uparrow\uparrow}}$ while we have seen experimentally that population imbalances are possible. Second, our decay model is very simplified and assumes that the $|\downarrow\rangle$ losses are immediately accompanied by the disappearance of $|\uparrow\rangle$ atoms when, in reality, these require a finite time to exit the observation region. This assumption imposes a lower bound in the measurement because it underestimates the total atom number.

7.4.4 *Density and three-body decay*

Three-body decay model

In the regime explored in the experiment, one- and two-body processes are negligible compared to three-body recombination (private communication from A. Simoni). Moreover the K_3 coefficient measured in the previous chapter is for a thermal gas, however, in order to

describe properly the decay observed in Fig. 7.8, we need to take into account the following:

- The system is in the BEC phase; therefore there is no bunching. A proper normalization of the K3 needs to be performed in order to avoid double counting [174].
- For a Bose-Bose mixture in the regime where δa is small, the LHY energy is non-negligible and therefore beyond mean-field corrections to the three-body correlation functions need to be taken into account.

Considering the later points the three-body recombination rates are described in the form

$$\begin{aligned} K_{\sigma\sigma\sigma} &= \frac{1}{3!}K^{\text{th}}_{\sigma\sigma\sigma}\left[1+\frac{6}{n_\sigma^2}\frac{\partial\mathcal{E}_{\text{LHY}}}{\partial g_{\sigma\sigma}}\right], \\ K_{\sigma\sigma\sigma'} &= \frac{1}{2!}K^{\text{th}}_{\sigma\sigma\sigma'}\left[1+\frac{2}{n_\sigma^2}\frac{\partial\mathcal{E}_{\text{LHY}}}{\partial g_{\sigma\sigma}}+\frac{2}{n_\sigma n_{\sigma'}}\frac{\partial\mathcal{E}_{\text{LHY}}}{\partial g_{\sigma\sigma'}}\right], \end{aligned}$$

where σ, σ' denote the spin states, $g_{\sigma\sigma'} = 4\pi\hbar^2 a_{\sigma\sigma'}/m$, and K_3^{th} are the thermal rates determined in section 6.6.2. The numerical pre-factors result from the indistinguishability of bosonic atoms [175], and the terms involving $\mathcal{E}_{\text{LHY}}$ correspond to the beyond mean-field corrections to the three-body correlation functions of the mixture. In the regime explored in the experiment, they remain $< 10\%$. Since this is well below the uncertainties of the thermal rates, we neglect them as in ref. [139]. This calculation was performed by D. Petrov and L. Santos (private communication).

Describing the decay of the self-bound states requires taking into account simultaneously two effects: (i) real loss of $|\downarrow\rangle$ atoms, since $K_{\downarrow\downarrow\downarrow}$ is much larger than the three other rates; (ii) expulsion (and subsequent expansion along the waveguide) of $|\uparrow\rangle$ atoms, in order to maintain the optimal spin composition of the self-bound state. Modeling accurately

the dynamics of these combined loss, expulsion and expansion processes goes beyond the scope of this work. We instead simplify the problem considerably by assuming that $|\downarrow\rangle$ losses are instantaneously accompanied by the disappearance of $|\uparrow\rangle$ atoms required to maintain $N_\uparrow/N_\downarrow$ fixed in the self-bound state. The decay of the self-bound atom number is then given by the rate equation

$$\frac{\dot{N}}{N} = -K_3^{\text{eff}}\langle n^2\rangle,$$

where $\langle n^2\rangle = \frac{1}{N}\int \mathrm{d}\mathbf{r}\, n^3$ and the effective three-body loss coefficient is $K_3^{\text{eff}} = K_{\downarrow\downarrow\downarrow}\Big/\left(1+\sqrt{\frac{a_{\downarrow\downarrow}}{a_{\uparrow\uparrow}}}\right)^2$. For more details about the model are included in the Appendix C.1.

To extract $\dot{N}/N$ from the decay curves, we fit them with the empirical function

$$N(t) = N_\infty + pN_0\mathrm{e}^{-(t-T_0)/T_1} + (1-p)N_0\mathrm{e}^{-(t-T_0)/T_2},$$

where N_0, N_∞, T_0, T_1, T_2 and p are free parameters.

We finally determine the peak density of the system from

$$n_0 = 3^{3/4}\sqrt{\langle n^2\rangle} = 3^{3/4}\left(1+\sqrt{\frac{a_{\downarrow\downarrow}}{a_{\uparrow\uparrow}}}\right)\sqrt{\frac{1}{K_{\downarrow\downarrow\downarrow}}\left|\frac{\dot{N}}{N}\right|}.$$

Here, we have assumed a Gaussian density profile to relate the peak and average densities to facilitate the comparison to the theoretical model.

We have verified that the results obtained using a different experimental fitting function are well below the uncertainties introduced by the $K_{\downarrow\downarrow\downarrow}$ systematic error. In any case, we expect our determination of the density to be dominated by the simplifications of the decay model.

7.4.5 *Crossing the bi-stability region*

In between the soliton and droplet solution we find a bi-stability region (gray area in Fig. 7.1) where both solutions coexist and are stable. In a last series of experiments, we study in detail this region. First, we compute for comparison the boundaries of the bi-stability region using the full numerical simulation and the variational Gaussian ansatz. In both methods we perform two separate N sweeps in order to find the ground state: increasing N starting from the soliton regime yields the soliton solution, whereas decreasing N starting from the droplet regime yields the droplet solution. To determine the boundaries of the bi-stable region we then compute $\left(n_0^D - n_0^S\right) / \left(n_0^D + n_0^S\right)$. This is shown in Fig. 7.10). Here the super-indexes depict the either the soliton (S) or droplet (D) solution.

In the deeply bound regime solitons and droplets are distinct solutions. They co-exist only in the bi-stable region. The top black line (III) in Fig.7.10 represents the upper boundary of the bistable region. This corresponds to the collapse of solitons into droplets when the system no longer behaves as one-dimensional. The lower line one (I) indicates the dissociation of droplets into solitons, here the kinetic energy becomes dominant. The distinction between solitons and droplets disappears when the free-space droplet size becomes comparable to the harmonic oscillator length a_{ho}, which determines the radial soliton size. Both become then smoothly connected in a crossover. Thus, the position of the critical point separating the transition and crossover regimes is determined by the confinement of the optical waveguide.

Experimentally the bi-stability is explored by preparing self-bound states in the soliton regime, and then the magnetic field is swept onto the bi-stability region (see left inset of Fig. 7.9). We prepare the system in the crossover region at $B \sim 56.3$ G and hold it in the crossed optical dipole trap for a variable time (1 to 120 ms). Owing to three-body recombination, this results in atom numbers $N = 3000$ to 7000. We then remove the vertical trapping beam, decrease B to its final value

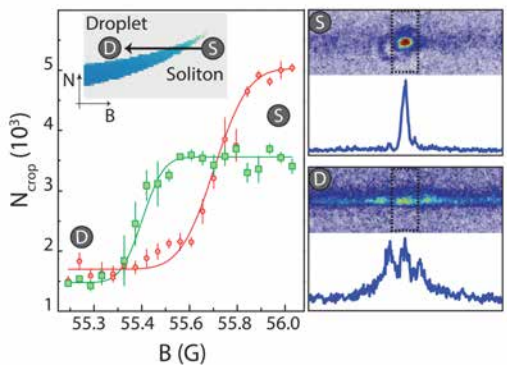

Figure 7.9: Soliton-to-droplet transition. Left panel: Atom number in the self-bound region N_{crop} as a function of magnetic field B when approaching the bi-stable region from the soliton regime, see inset. The green and red points represent two different initial atom numer. Top right panel: initial soliton image (S) and corresponding doubly-integrated density profile. Bottom right panel: fragmentation observed when entering the droplet regime (D).

at a rate of 93.8 G/s[3], and take an *in situ* image 3.5 ms after the end of the ramp.

As explained before, in the boundaries of the bi-stable region the density of the system becomes discontinuous. This point is where only the soliton (droplet) solution exists. Experimentally, we observe that the self-bound state cannot adjust to this abrupt change and fragments (see Fig. 7.9 (right panel)). The shape of the final distribution after fragmentation varies from shot-to-shot. To locate the fragmentation point, we record the atom number in the initially self-bound region and observe an abrupt drop at a critical magnetic field. In the left panel of Fig. 7.9, we show how the position of fragmentation depends on the initial atom number. The critical magnetic field for fragmentation B_c

3 Due to the discontinuity in density at the transition point, the fragmentation of the system is independent of the magnetic field ramp rate. This value is chosen such that the magnetic ramp is faster than the three-body losses timescale. Therefore the atom number during the ramp remains constant.

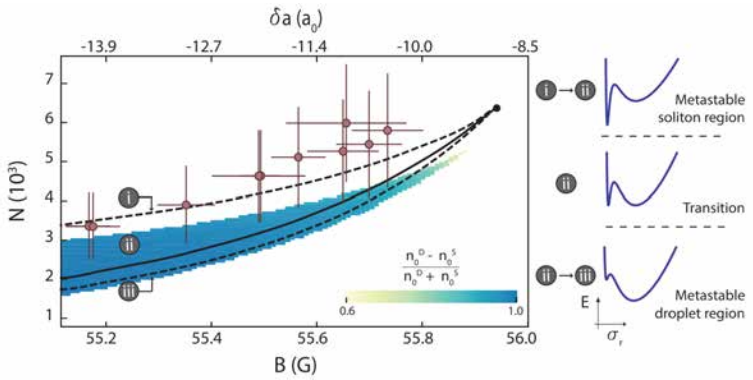

Figure 7.10: Soliton-to-droplet transition. To determine the boundaries of the bi-stable region we compute $\left(n_0^D - n_0^S\right) / \left(n_0^D + n_0^S\right)$. The experimental points represent the measured fragmentation point vs. N and B. Error bars: systematic error in N and magnetic field width of the fragmentation curve. Colored area: bi-stable region computed numerically from the eGPE. Lines: variational model, indicating the boundaries of the bi-stable region (dashed) and the transition line where solitons and droplets have identical energies E (solid). Insets: sketch of E vs. σ_z for the metastable soliton and droplet regions and the transition line.

for different initial values of N_i is obtained by fitting curves analogous to those of Fig. 7.9 (left panel) with an error function

$$N_{\text{crop}} = \left(\frac{N_i - N_f}{2}\right) \text{erf}\left(-\frac{B - B_c}{\sqrt{2}\sigma}\right) + N_f, \tag{7.4}$$

where N_i, N_f, and B_c are free parameters. The horizontal error bars of the fragmentation points correspond to σ, and the vertical ones to the 25% systematic error on the atom number calibration. We summarize the position of the fragmentation point in the $N - B$ plane in Fig. 7.10.

We exploit the variational model to interpret our observations. According to it, although in the bi-stable region both solitons and droplets exist, their energies coincide only along a transition line (solid line). Above (below) it, solitons (droplets) become metastable and only disappear at the upper (lower) boundary (dashed lines). The three situations are depicted in the right panel of Fig. 7.10. Experimentally, we

prepare the mixture in a regime where only solitons exist. Therefore, when entering the bi-stable region, we expect it to follow preferentially the metastable soliton solution, with which it connects smoothly. At the upper boundary, the metastable soliton disappears, and only dense droplets are possible. Hence, the system is expected to fragment and form an excited state with equal total energy. Our experimental results support this hypothesis: within error bars, the fragmentation point agrees with the upper boundary of the bi-stable region predicted by the variational (solid line) and numerical eGPE (coloured area) calculations without any fitting parameters.

Note. The fragments observed experimentally do not correspond to the ground state of the system. Instead, immediately after the ramp we expect to form an excited state with the same total energy (see refs. [149, 150] for related theoretical studies in the dipolar case). Since the atom number in each of the fragments is typically below the atom number required to form a droplet we expect that, after some relaxation dynamics, the system will evolve into a soliton train. Thus, although the fragmentation point corresponds to the onset of a modulation instability in the system and allows to map out the boundary of the bi-stable region, the final state is the result of complex non-linear dynamics and is not directly related to the ground state droplet solution. We have therefore not studied it in detail. In dipolar droplets, similar behaviour is reported by crossing from a repulsive dipolar BEC to the quantum droplet regime. The fragmentation patterns are located in their case by using a principal component analysis (PCA) of the data sets [172].

7.4.6 *Conclusion*

In conclusion, we have shown that an attractive mixture of BECs confined in an optical waveguide always hosts self-bound states, which correspond to composite bright solitons, quantum liquid droplets, or interpolate smoothly between both limits depending on the values of

the atom number, interaction strength, and confinement. We have characterized their spin composition and density and mapped out the upper boundary of the bi-stable region separating solitons and droplets.

8

OUTLOOK

The main achievement of this thesis is the demonstration of a self-bound state in a Bose-Bose mixture with effective attractive interactions. This self-bound state can be understood as **quantum liquid droplet** and its existence is purely given by quantum fluctuations which are BMF effects.

Due to the novelty of this quantum liquid, some possible research directions can be summarized as follows:

- Characterization of the fundamental properties of quantum droplets.
- Quantum fluctuations and their tunability.
- Exotic systems composed of mixture droplets.

Characterization of the fundamental properties of quantum droplets

In this thesis, we have mainly focused on the self-bound properties of our droplet together with the quantum gas-to-liquid transition. In addition, we have compared this state with a bright soliton finding interesting connections between both states. However a precise characterization of the fundamental properties of these quantum droplets is still missing. Experimental measurements in several aspects such as the superfluid character or the possible role of finite temperature effects for example remain to be performed.

One fundamental open question in this system is the peculiar excitation spectrum predicted in the original theoretical proposal [3]. It is suggested that such liquid should have a regime where no excitations exist (see chapter 6). Therefore, it would be interesting to study

its *collective modes*. We could study both in- and out-of-phase excitations of the two components and map out with precise measurements the frequencies of the modes as a function of interaction strength. If this regime exists, the system should self-evaporate into a zero temperature object. There is no doubt this is an interesting prediction that needs to be verified experimentally.

In addition, by characterizing the frequency response of the system, we could give an extra constraint to beyond mean field theories that could explain the discrepancies between theory and experiment presented in chapter 6.

A different method to study the excitation spectrum of a Bose-Bose mixture is to employ Bragg spectroscopy. The stabilization of quantum droplets as explained in chapter 6 is a manifestation of the peculiar Bogoliubov spectrum (spin and density modes) of a Bose-Bose mixture. It would be then interesting to measure the energy spectrum at $\delta a > 0$ and see the progressive softening of the density branch as we approach the mean-field instability. At $\delta a < 0$, in the homogeneous regime where a flat-top density profile is expected, we should observe a single branch (absence of the spin mode) with a linear behaviour. This is valid for low energy excitations. The slope of the linear regime should give us information about the critical velocity up to which superfluid phenomena exists.

These measurements could help us gain a deeper understanding of the system at the microscopic level.

Quantum fluctuations and their tunability

The absence of collapse in an effective attractive Bose-Bose mixture is an unexpected result that comes in principle from quantum fluctuations. Therefore, this particular topic deserves further investigation.

A second possible route of research in the field of quantum liquid droplets is the demonstration of novel tools to control the quantum fluctuations in the system. Being able to modify their value would re-

sult in a modification of the beyond-mean-field stabilizing energy term and therefore a strong modification of the droplet properties. With this in mind, two different approaches could play an important role: droplets in low dimensions or coherent coupling of the two components.

Liquids in lower dimensions. In this thesis, we have explored the properties of this quantum liquid in the 3D-regime. However low dimensional systems are interesting due to the well-known enhancement of quantum fluctuations. For instance, it has been already predicted that a Bose-Bose mixture in two-dimensions holds as well a droplet solution without the restriction of the critical atom number N_c [176]. As soon as attractive inter- and repulsive intra-species interactions are available, the self-bound state should form. This will lead to more robust droplet formation and to longer lifetimes as compared to the 3D regime, because atom loss due to e.g. three-body decay is not as important. In particular, it should allow the realization of droplets reaching the bulk liquid limit, where surface effects can be neglected. This results will mark the transition from a quantum droplet with finite size and mainly formed of surface to a quantum drop with a significant bulk region. This last configuration should allow us to investigate the exotic liquid properties of our system, including its compressibility, equation of state, excitation spectrum, superfluid character, vortices, etc.

We could also explore the physics in one-dimensional systems. Contrary to the 3D and 2D case, in this regime, the liquid regime appears when the beyond mean-field term is attractive while the mean-field interactions are repulsive. In this case analytical results are available in the weakly interacting regime. Interestingly, in one dimension the parameter characterizing the interaction strength of the system is proportional to the inverse of the particle density. By making the system more dilute, this should allow us to investigate the strongly interacting regime, where higher-order beyond mean-field terms become rel-

evant. Thus, one-dimensional systems offer the possibility to explore systematically the evolution of the system between the weakly and the strongly interacting limits.

Finally, playing with dimensionality also allows us to study interesting scenarios such as dimensional crossovers (intermediate regimes between two dimensions) [168, 169], and its interplay by crossing the dimensionality. We could explore the situation in a regime of parameters where droplets exist in 2D but not in 3D. By starting with a 3D system we could go to a 2D system by compressing the gas. In the process, a liquid will be formed. In this sense, this could be seen as a quantum "dimensional liquefaction."

Coherently coupled droplets. In our system we need two different internal states to form an incoherent mixture that gives rise to our quantum droplet . However, it has been predicted that droplets should also exist when the two states are coherently coupled [177]. This could be achieved either by using RF or Raman coupling. In this situation the scattering properties of the “dressed” atoms can be controlled depending of the parameters of the coupling field. This coupling would modify both the mean-field and beyond-mean field energy terms.

In particular it is predicted that large effective three-body interactions (elastic and repulsive) could be induced. These have never been demonstrated so far in the quantum gases context, and their demonstration could open the possibility to explore novel exotic many-body phases [178–180].

Exotic systems composed of mixture droplets

Up to this point, we have discussed the possible research directions using our current experimental setup. However, we could explore as well the realization of novel exotic quantum systems using our quantum droplets.

Impurities and quantum droplets. The first idea could be to trap impurities inside the droplet. Here we could study the polaron problem with a quantum bath that is self-bound and with the presence of surface tension [181]. This is something that is not accesible in experiments with impurities in a Bose-Einstein condensate. In this context, we could also perform similar experiments with a Rydberg atom inside the droplet and study analogous situations as molecules trapped inside helium nano-droplets and the formation of the so-called angulon quasiparticles [182]. This could extend our knowledge of the properties of molecules immersed in a quantum bath.

Also, a droplet with impurities could serve as a bath to sympathetically cool the atoms to zero temperatures. This is true provided first that the droplet can self-evaporate as mentioned at the beginning of this chapter.

Bose-Fermi droplets. In quasi-1D geometries an attractive Bose-Fermi mixture has been predicted to form a bright soliton [183]. Moreover, in a recent proposal it has been shown that it could also hold a self-bound liquid droplet stabilized by quantum fluctuations [184, 185]. These predictions have not been observed experimentally and therefore we could follow this research line.

In our potassium experiment we could work arbitrarily with the three different isotopes of potassium; therefore it would be possible, with minor changes in the experimental setup, to go from Bose-Bose to Bose-Fermi mixtures. We could study in our system the validity of these theoretical proposals and the properties of the system.

Droplets as high dimensional solitons

In chapter 7 we have presented the connection between bright solitons and droplets, regarding this topic we could study in the future the metastability and hysteresis when crossing the soliton-to-droplet transition from different directions.

Another exciting possibility is to perform collisions between two self-bound states, which are expected to display very different behavior in the soliton and droplet limits [140, 186, 187]. In our system there is no critical number where the soliton collapses, therefore during the collision of two solitons they could either merge or pass one on top of the other without this constrain.

Finally, spin imbalanced systems offer the possibility to explore finite temperature effects [188] in a well-controlled setting, exploiting the excess component as a thermal bath.

And more...

The novelty of this system opens new frontiers on the understanding of quantum liquids at low temperatures and low densities. This is just the beginning of exciting experiments. In the upcoming years we hope we could adventure in more complicated and sophisticated problems in which we could even explore **the universe in a composite quantum droplet** [147].

Part I

APPENDIX

APPENDIX CHAPTER 2

A.1 COATING FOR 2DMOT AND SCIENCE CHAMBER WINDOWS

The different coatings are custom-made from LaserOptik. The coating is placed on the viewports using an electron-beam physical vapor deposition technique.

2D MOT rectangular windows

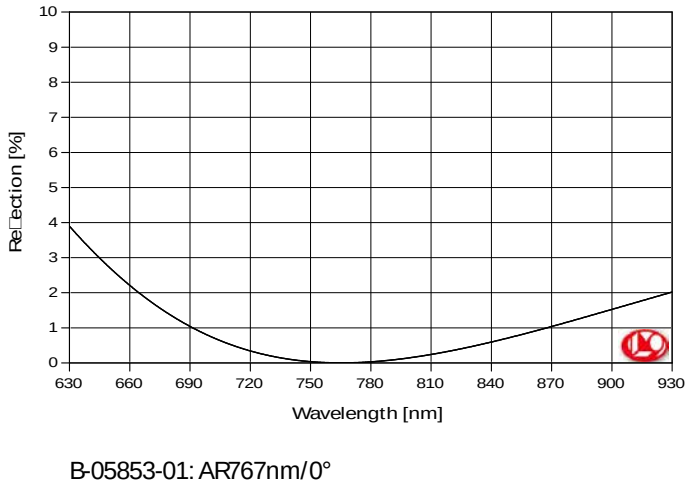

Figure A.1: Coating of the 2DMOT rectangular windows. AR coated from both sides at 767 nm/0°.

Science chamber viewports

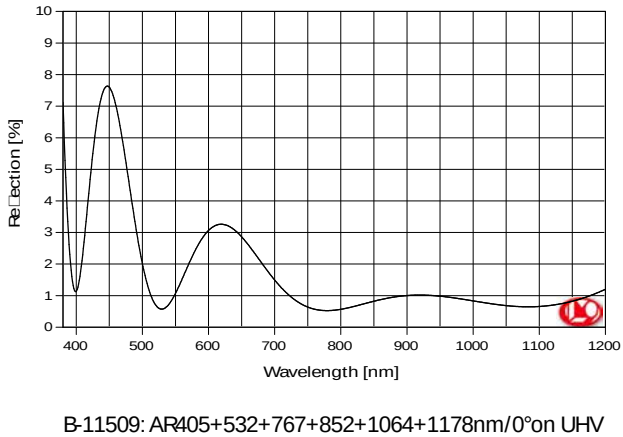

Figure A.2: Anti-reflection (AR) coating for several wavelengths used for the lateral viewports of the science chamber.

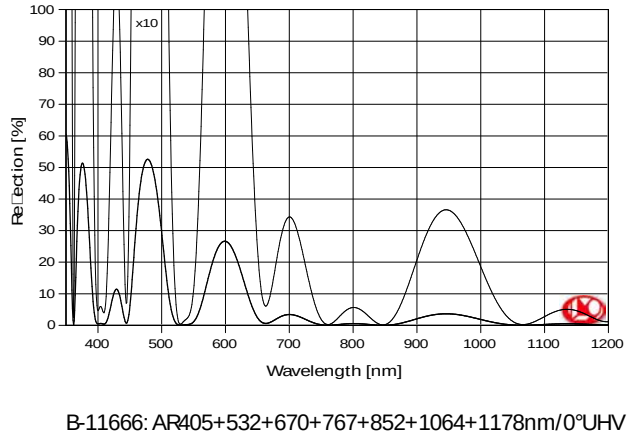

Figure A.3: Anti-reflection (AR) coating for several wavelengths used for the re-entrant viewports of the science chamber.

B

APPENDIX CHAPTER 3

The place where we have performed all the experiments presented in this thesis is located in the LAB002 at ICFO – The Institute of Photonic Sciences in Barcelona, Spain. This is called at ICFO the the quantum gas experiment (QGE) lab.

I started my Ph.D. officially in January 2014; we received our lab in February 2014. In Fig. B.1 we show our empty lab. In Fig. B.2 we show the current status.

B.1 THE QGE LAB

B.1.1 *The optical tables*

In the QGE potassium experiment we have two independent optical tables (see Fig. B.1). One is used for the laser system required to perform laser cooling and imaging of the three different potassium isotopes. The second one is where the experiment takes place. Here we have mounted the UHV system and also the laser system for the different optical dipole traps presented in section 3.3.5.

The optical tables are caged with anodized aluminium Alucobond panels that provide laser safety while improving the temperature stability of its environment (see Fig. B.2). In addition, each optical table is climatized independently from the room with stability of $\pm 0.1°C$. The excellent temperature stabilization of the optical tables makes that the laser system shown in Fig. B.2 only needs to be realigned sporadically.

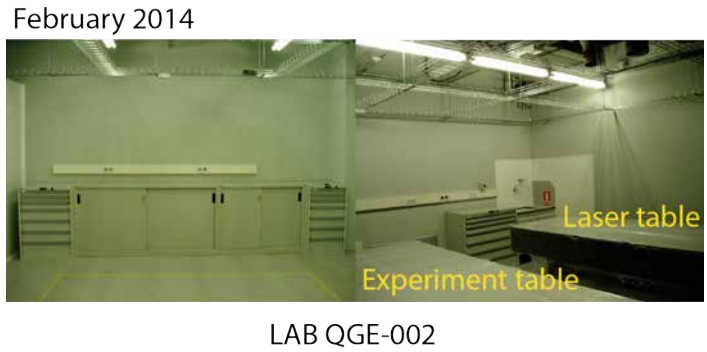

Figure B.1: QGE lab in 2014

B.1.2 *RF Isolation*

During the magnetic evaporation of ^{41}K and also some of the RF pulses needed to control the internal state of our BEC, we have observed that the RF couples to several of our electronic devices and produce unwanted noise in neighbouring laboratories. We have therefore isolated the walls of our lab with an electromagnetic field shielding fabric[1]. We observe an RF isolation of more than 20 dBm.

In addition, the power supplies used for the Feshbach coils and the PID control are located in a different room to reduce the RF noise and improve the current stabilization.

B.2 THE LATERAL BREADBOARDS

Around the vacuum system, we have placed four optical breadboards. One for the 2D MOT optics and three for the optics required around the science chamber (see Fig.B.3).

The lateral breadboards are custom-made aluminium plates[2] that lay on top of four stainless steel balls (see bottom panel Fig. B.3). The

1 CobalTex - Less EMF
2 Standa

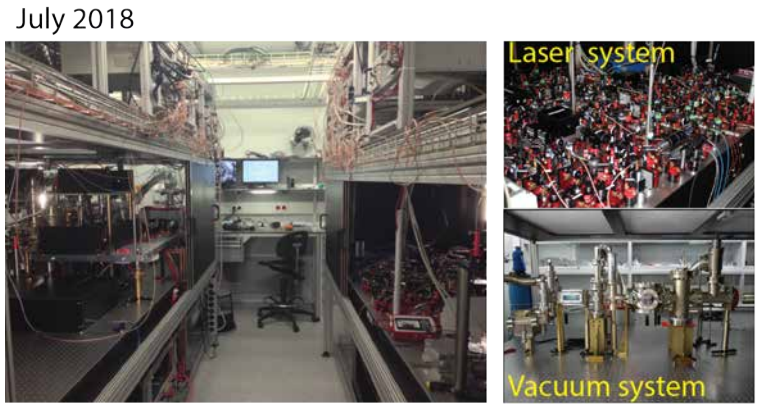

Figure B.2: QGE lab in 2018.

stainless steel balls[3] are in contact with four brass inserts that define without mechanical constrains the position of each lateral breadboard. In our case we use a groove, a cone and two flat surfaces. Using this mechanism we in principle improve the stability of the breadboard. Up to date, we have not been limited in our experiment by vibrations or displacement of the lateral breadboards.

The top breadboard is where the Andor camera is placed together with the imaging optics. This breadboard is concentric to the "$Z-$axis" axis of the Feshbach coils, therefore it is made of epoxy resin reinforced fiberglass[4] in order to avoid eddy currents during the manipulation of magnetic fields.

3 304 stainless steel balls (7154155964) - Alwayse
4 EP GC 201 - Hippe

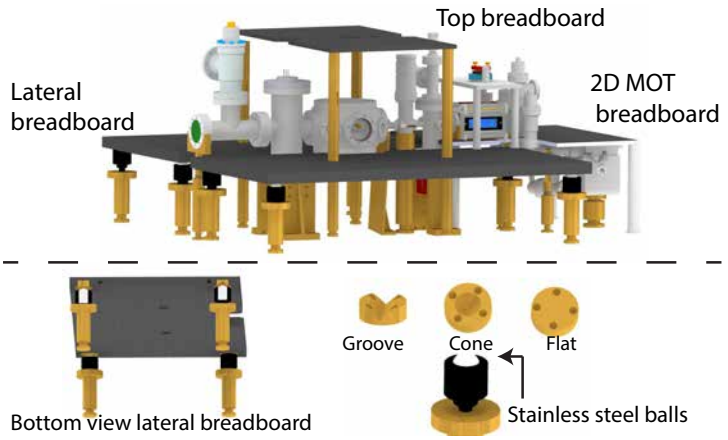

Figure B.3: The lateral breadboards lay on top of for stainless steel balls and four insets that define the final position. In principle using this configuration the breadboards are free of mechanical contrains, resulting on a higher stability.

C

APPENDIX CHAPTER 6

C.1 THREE-BODY DECAY MODEL

We extract the density of the system in chapter 7 by assuming that there are only losses on the state $|\downarrow\rangle$. We assume that $|\uparrow\rangle$ is instantaneously lost in order to conserve the optimal ratio of the self-bound state.

We start with the condition presented in Eq. 2.53 where we assume identical spatial modes for the two components. Therefore the density ratio is locked to the condition

$$n_\downarrow(r)/n_\uparrow(r) = \sqrt{a_{\uparrow\downarrow}/a_{\downarrow\uparrow}} = \alpha_r. \tag{C.1}$$

Assuming that the losses in $|\downarrow\rangle$ state are only due to three body collisions with atoms in $|\downarrow\rangle$ we have:

$$\dot{n}_\downarrow(r,t) = -K_{\downarrow\downarrow\downarrow} n_\downarrow^3(r,t), \tag{C.2}$$

where $\dot{n}_\downarrow(r) = \frac{\dot{n}_\uparrow(r)}{\alpha_r}$ extracted from the time derivative of Eq.C.1.

The total variation in density n in the system is thus given by

$$\dot{n} = \dot{n}_\downarrow + \dot{n}_\uparrow = -\left(1 + \frac{1}{\alpha_r}\right) K_{\downarrow\downarrow\downarrow} n_\downarrow^3(r,t). \tag{C.3}$$

We can express then the density distribution in terms of the average density as

$$\left\langle n_\downarrow^2 \right\rangle = \frac{1}{N_\downarrow} \int n_\downarrow^3(r)\, d^3r. \tag{C.4}$$

By inserting Eq. C.4 into Eq. C.3 and rewriting the equations in terms of atom number we obtain

$$\frac{\dot{N}}{N_\downarrow} = -\left(1+\frac{1}{\alpha_r}\right) K_{\downarrow\downarrow\downarrow} \left\langle n_\downarrow^2 \right\rangle \tag{C.5}$$

which in terms of the total atom number reads

$$\frac{\dot{N}}{N} = K_{\downarrow\downarrow\downarrow} \left\langle n_\downarrow^2 \right\rangle . \tag{C.6}$$

We now express $\left\langle n_\downarrow^2 \right\rangle$ as a function of $\langle n^2 \rangle$. This is convenient because in our experiment we do not perform spin resolved *in situ* imaging but instead we measure the total atom number.

$$\begin{aligned} \left\langle n_\downarrow^2 \right\rangle = \frac{1}{N_\downarrow} \int n^3(r)_\downarrow d^3r &= \frac{1+\frac{1}{\alpha_r}}{N} \int \left(\frac{n}{1+\frac{1}{\alpha_r}}\right)^3 d^3r \\ &= \frac{1}{\left(1+\frac{1}{\alpha_r}\right)^2} \frac{1}{N} \int d^3r\, n^3(r) \\ \left\langle n_\downarrow^2 \right\rangle &= \frac{1}{\left(1+\frac{1}{\alpha_r}\right)^2} \langle n^2 \rangle . \end{aligned} \tag{C.7}$$

In conclusion we obtain

$$\frac{\dot{N}}{N} = -K_{\downarrow\downarrow\downarrow} \frac{1}{\left(1+\frac{1}{\alpha_r}\right)^2} \langle n^2 \rangle \tag{C.8}$$

which is presented in the chapter 7 in Eq. 7.4.

BIBLIOGRAPHY

1. Petrov, D. S. Liquid beyond the van der Waals paradigm. *Nature Physics* **14,** 211–212 (2018) (cit. on pp. 1–3).
2. Rowlinson, J. S. Legacy of van der Waals. *Nature* **244,** 414 (1973) (cit. on p. 1).
3. Petrov, D. S. Quantum Mechanical Stabilization of a Collapsing Bose-Bose Mixture. *Phys. Rev. Lett.* **115,** 155302 (2015) (cit. on pp. 5, 29, 30, 37, 39, 118, 120–123, 125, 129, 135, 152, 158, 171, 183).
4. C. J. Pethick, H. S. *Bose-Einstein condensation in Dilute Gases* (Cambridge University Press, 2002) (cit. on pp. 9, 10, 17, 18, 20–22, 24, 29, 43, 46, 164).
5. Dalibard, J. *Collisional dynamics of ultra-cold atomic gases, in Bose-Einstein Condensation in Atomic Gases* (IOS Press Amsterdam, 1999) (cit. on pp. 10, 16).
6. Weiner, J., Bagnato, V. S., Zilio, S. & Julienne, P. S. Experiments and theory in cold and ultracold collisions. *Rev. Mod. Phys.* **71,** 1–85 (1999) (cit. on p. 10).
7. Duine, R. & Stoof, H. Atom–molecule coherence in Bose gases. *Physics Reports* **396,** 115 –195 (2004) (cit. on p. 10).
8. Chin, C., Grimm, R., Julienne, P. & Tiesinga, E. Feshbach resonances in ultracold gases. *Rev. Mod. Phys.* **82,** 1225–1286 (2010) (cit. on p. 10).
9. Tiecke, T. *Feshbach resonances in ultracold mixtures of the fermionic quantum gases ^{6}Li and ^{40}K.* PhD thesis (University of Amsterdam, 2009) (cit. on pp. 11, 44).

10. DeMarco, B. & Jin, D. S. Onset of Fermi Degeneracy in a Trapped Atomic Gas. *Science* **285,** 1703–1706 (1999) (cit. on p. 12).
11. Schreck, F. *et al.* Sympathetic cooling of bosonic and fermionic lithium gases towards quantum degeneracy. *Phys. Rev. A* **64,** 011402 (2001) (cit. on p. 12).
12. Feshbach, H. Unified theory of nuclear reactions. *Annals of Physics* **5,** 357 –390 (1958) (cit. on p. 14).
13. Fano, U. Effects of Configuration Interaction on Intensities and Phase Shifts. *Phys. Rev.* **124,** 1866–1878 (1961) (cit. on p. 14).
14. Chin, C., Grimm, R., Julienne, P. & Tiesinga, E. Feshbach resonances in ultracold gases. *Rev. Mod. Phys.* **82,** 1225–1286 (2010) (cit. on p. 15).
15. Gross, N., Shotan, Z., Kokkelmans, S. & Khaykovich, L. Nuclear-Spin-Independent Short-Range Three-Body Physics in Ultracold Atoms. *Phys. Rev. Lett.* **105,** 103203 (2010) (cit. on p. 16).
16. Dyke, P., Pollack, S. E. & Hulet, R. G. Finite-range corrections near a Feshbach resonance and their role in the Efimov effect. *Phys. Rev. A* **88,** 023625 (2013) (cit. on p. 16).
17. Zwerger, W. *The BCS-BEC Crossover and the Unitary Fermi Gas* 1st ed. (Springer, Varenna, Italy, 2012) (cit. on pp. 16, 30, 44).
18. Moses, S., Covey, J. P., Miecnikowski, M. T., Jin, D. S. & Ye, J. New frontiers for quantum gases of polar molecules. *Nature Physics* **13,** 13 EP – (2016) (cit. on p. 16).
19. Bogoliubov, N. N. On the theory of superfluidity. *J. Phys. (USSR)* **11** (1947) (cit. on p. 18).
20. Cohen-Tannoudji, C. & Guery-Odelin, D. *Advances in Atomic Physics: An Overview* 1st ed. (World Scientific, 2011) (cit. on p. 22).
21. Carr, L. D. & Castin, Y. Dynamics of a matter-wave bright soliton in an expulsive potential. *Phys. Rev. A* **66,** 063602 (2002) (cit. on pp. 23, 136, 158, 164).

22. Roberts, J. L., Claussen, N. R., Cornish, S. L., Donley, E. A., Cornell, E. A. & Wieman, C. E. Controlled Collapse of a Bose-Einstein Condensate. *Phys. Rev. Lett.* **86,** 4211–4214 (2001) (cit. on pp. 23, 25).

23. Donley, E. A., Claussen, N. R., Cornish, S. L., Roberts, J. L., Cornell, E. A. & Wieman, C. E. Dynamics of collapsing and exploding Bose–Einstein condensates. *Nature* **412,** 295–299 (2001) (cit. on pp. 23, 25).

24. Zakharov, V. F. & A. B, S. Exact Theory of Two-dimensional Self-focusing and One-dimensional Self-modulation of Wave in Nonlinear Media. *JETP Lett.* **34,** 62 (1972) (cit. on p. 23).

25. Pérez-García, V. M., Michinel, H. & Herrero, H. Bose-Einstein solitons in highly asymmetric traps. *Phys. Rev. A* **57,** 3837–3842 (1998) (cit. on pp. 23, 158).

26. Strecker, K. E., Partridge, G. B., Truscott, A. G. & Hulet, R. G. Formation and propagation of matter-wave soliton trains. *Nature* **417,** 150 EP – (2002) (cit. on pp. 24, 158).

27. Khaykovich, L. *et al.* Formation of a Matter-Wave Bright Soliton. *Science* **296,** 1290–1293 (2002) (cit. on pp. 24, 158).

28. Medley, P., Minar, M. A., Cizek, N. C., Berryrieser, D. & Kasevich, M. A. Evaporative Production of Bright Atomic Solitons. *Phys. Rev. Lett.* **112,** 060401 (2014) (cit. on pp. 24, 158).

29. Cornish, S. L., Thompson, S. T. & Wieman, C. E. Formation of Bright Matter-Wave Solitons during the Collapse of Attractive Bose-Einstein Condensates. *Phys. Rev. Lett.* **96,** 170401 (2006) (cit. on pp. 24, 158).

30. Marchant, A. L., Billam, T. P., Wiles, T. P., Yu, M. M. H., Gardiner, S. A. & Cornish, S. L. Controlled formation and reflection of a bright solitary matter-wave. *Nature Communications* **4.** Article, 1865 EP – (2013) (cit. on pp. 24, 158).

31. McDonald, G. D. *et al.* Bright Solitonic Matter-Wave Interferometer. *Phys. Rev. Lett.* **113,** 013002 (2014) (cit. on pp. 24, 158).

32. Lepoutre, S. *et al.* Production of strongly bound ^{39}K bright solitons. *Phys. Rev. A* **94,** 053626 (2016) (cit. on pp. 24, 148, 158, 170).

33. Salasnich, L. Bright solitons in ultracold atoms. *Optical and Quantum Electronics* **49,** 409 (2017) (cit. on p. 24).

34. Sackett, C. A., Stoof, H. T. C. & Hulet, R. G. Growth and Collapse of a Bose-Einstein Condensate with Attractive Interactions (1998) (cit. on p. 25).

35. Gerton, J. M., Strekalov, D., Prodan, I. & Hulet, R. G. Direct observation of growth and collapse of a Bose-Einstein condensate with attractive interactions. *Nature* **408,** 692 EP – (2000) (cit. on p. 25).

36. Eigen, C., Gaunt, A. L., Suleymanzade, A., Navon, N., Hadzibabic, Z. & Smith, R. P. Observation of Weak Collapse in a Bose-Einstein Condensate. *Phys. Rev. X* **6,** 041058 (2016) (cit. on p. 25).

37. Dalfovo, F., Giorgini, S., Pitaevskii, L. P. & Stringari, S. Theory of Bose-Einstein condensation in trapped gases. *Rev. Mod. Phys.* **71,** 463–512 (1999) (cit. on p. 25).

38. Chevy, F & Salomon, C. Strongly correlated Bose gases. *Journal of Physics B: Atomic, Molecular and Optical Physics* **49,** 192001 (2016) (cit. on pp. 28, 30, 31, 44).

39. Pérez-García, V. M., Michinel, H. & Herrero, H. Bose-Einstein solitons in highly asymmetric traps. *Physical Review A* **57,** 3837–3842 (1998) (cit. on p. 29).

40. Lee, T. D., Huang, K. & Yang, C. N. Eigenvalues and Eigenfunctions of a Bose System of Hard Spheres and Its Low-Temperature Properties. *Phys. Rev.* **106,** 1135–1145 (1957) (cit. on p. 30).

41. Lee, T. D. & Yang, C. N. Many-Body Problem in Quantum Mechanics and Quantum Statistical Mechanics. *Phys. Rev.* **105,** 1119–1120 (1957) (cit. on p. 30).

42. Petrov, D. S., Salomon, C. & Shlyapnikov, G. V. Weakly Bound Dimers of Fermionic Atoms. *Phys. Rev. Lett.* **93,** 090404 (2004) (cit. on p. 30).

43. Leyronas, X. & Combescot, R. Superfluid Equation of State of Dilute Composite Bosons. *Phys. Rev. Lett.* **99,** 170402 (2007) (cit. on p. 30).

44. Navon, N. *et al.* Dynamics and Thermodynamics of the Low-Temperature Strongly Interacting Bose Gas. *Phys. Rev. Lett.* **107,** 135301 (2011) (cit. on p. 31).

45. Wild, R. J., Makotyn, P., Pino, J. M., Cornell, E. A. & Jin, D. S. Measurements of Tan's Contact in an Atomic Bose-Einstein Condensate. *Phys. Rev. Lett.* **108,** 145305 (2012) (cit. on p. 31).

46. Lopes, R., Eigen, C., Navon, N., Clément, D., Smith, R. P. & Hadzibabic, Z. Quantum Depletion of a Homogeneous Bose-Einstein Condensate. *Phys. Rev. Lett.* **119,** 190404 (2017) (cit. on p. 31).

47. Lopes, R. *et al.* Quasiparticle Energy in a Strongly Interacting Homogeneous Bose-Einstein Condensate. *Phys. Rev. Lett.* **118,** 210401 (2017) (cit. on p. 31).

48. *Quantum Matter at Ultralow Temperatures. Proceedings of the international school of physics "Enrico Fermi"* 1st ed. (IOS, Varenna, Italy, 2015) (cit. on pp. 31, 35).

49. Ho, T.-L. & Shenoy, V. B. Binary Mixtures of Bose Condensates of Alkali Atoms. *Phys. Rev. Lett.* **77,** 3276–3279 (1996) (cit. on p. 33).

50. Hall, D. S., Matthews, M. R., Ensher, J. R., Wieman, C. E. & Cornell, E. A. Dynamics of Component Separation in a Binary Mixture of Bose-Einstein Condensates. *Phys. Rev. Lett.* **81,** 1539–1542 (1998) (cit. on pp. 33, 137, 169).

51. Timmermans, E. Phase Separation of Bose-Einstein Condensates. *Phys. Rev. Lett.* **81,** 5718–5721 (1998) (cit. on p. 33).

52. Ao, P. & Chui, S. T. Binary Bose-Einstein condensate mixtures in weakly and strongly segregated phases. *Phys. Rev. A* **58,** 4836–4840 (1998) (cit. on p. 33).

53. Papp, S. B., Pino, J. M. & Wieman, C. E. Tunable Miscibility in a Dual-Species Bose-Einstein Condensate. *Phys. Rev. Lett.* **101,** 040402 (2008) (cit. on p. 33).

54. McCarron, D. J., Cho, H. W., Jenkin, D. L., Köppinger, M. P. & Cornish, S. L. Dual-species Bose-Einstein condensate of ^{87}Rb and ^{133}Cs. *Phys. Rev. A* **84,** 011603 (2011) (cit. on p. 33).

55. Wacker, L. *et al.* Tunable dual-species Bose-Einstein condensates of ^{39}K and ^{87}Rb. *Phys. Rev. A* **92,** 053602 (2015) (cit. on pp. 33, 102, 133).

56. Wang, F., Li, X., Xiong, D. & Wang, D. A double species 23 Na and 87 Rb Bose–Einstein condensate with tunable miscibility via an interspecies Feshbach resonance. *Journal of Physics B: Atomic, Molecular and Optical Physics* **49,** 015302 (2016) (cit. on p. 33).

57. Modugno, G., Roati, G., Riboli, F., Ferlaino, F., Brecha, R. J. & Inguscio, M. Collapse of a Degenerate Fermi Gas. *Science* **297,** 2240–2243 (2002) (cit. on p. 33).

58. Modugno, M., Ferlaino, F., Riboli, F., Roati, G., Modugno, G. & Inguscio, M. Mean-field analysis of the stability of a K-Rb Fermi-Bose mixture. *Phys. Rev. A* **68,** 043626 (2003) (cit. on p. 33).

59. Adhikari, S. K. Mean-field description of a dynamical collapse of a fermionic condensate in a trapped boson-fermion mixture. *Phys. Rev. A* **70,** 043617 (2004) (cit. on p. 33).

60. Chui, S. T., Ryzhov, V. N. & Tareyeva, E. E. Stability of the Bose system in Bose-Fermi mixture with attraction between bosons and fermions. *Journal of Experimental and Theoretical Physics Letters* **80,** 274–279 (2004) (cit. on p. 33).

61. Ospelkaus, S., Ospelkaus, C., Humbert, L., Sengstock, K. & Bongs, K. Tuning of Heteronuclear Interactions in a Degenerate Fermi-Bose Mixture. *Phys. Rev. Lett.* **97,** 120403 (2006) (cit. on p. 33).

62. Lee, K. L., Jørgensen, N. B., Liu, I.-K., Wacker, L., Arlt, J. J. & Proukakis, N. P. Phase separation and dynamics of two-component Bose-Einstein condensates. *Phys. Rev. A* **94,** 013602 (2016) (cit. on p. 34).

63. Lee, K. L. *et al.* Time-of-flight expansion of binary Bose–Einstein condensates at finite temperature. *New Journal of Physics* **20,** 053004 (2018) (cit. on p. 34).

64. Abad, M. & Recati, A. A study of coherently coupled two-component Bose-Einstein condensates. *The European Physical Journal D* **67,** 148 (2013) (cit. on p. 35).

65. Goldstein, E. V. & Meystre, P. Quasiparticle instabilities in multicomponent atomic condensates. *Phys. Rev. A* **55,** 2935–2940 (1997) (cit. on p. 36).

66. Cabrera, C. R. *et al.* Quantum liquid droplets in a mixture of Bose-Einstein condensates. *Science* **359,** 301–304 (2018) (cit. on pp. 39, 117, 118, 120, 158).

67. Semeghini, G. *et al.* Self-Bound Quantum Droplets of Atomic Mixtures in Free Space. *Phys. Rev. Lett.* **120,** 235301 (2018) (cit. on pp. 39, 118, 120, 154).

68. Larsen, D. M. Binary mixtures of dilute bose gases with repulsive interactions at low temperature. *Annals of Physics* **24,** 89–101 (1963) (cit. on p. 39).

69. Metcalf, H. J. & van der Straten, P. *Laser Cooling and Trapping* (Springer, 1999) (cit. on pp. 43, 88).

70. Ketterle, W., Durfee, D. & Stamper-Kurn, D. in *Volume 140: Bose-Einstein Condensation in Atomic Gases. Proceedings of the International School of Physics Enrico Fermi* 67–176 (IOS Press Amsterdam, 1998) (cit. on p. 43).

71. Inguscio, M. & Fallani, L. *Atomic Physics: Precise Measurements and Ultracold Matter* 1st ed. (Oxford, 2013) (cit. on p. 43).

72. Modugno, G., Ferrari, G., Roati, G., Brecha, R. J., Simoni, A. & Inguscio, M. Bose-Einstein Condensation of Potassium Atoms by Sympathetic Cooling. *Science* **294,** 1320–1322 (2001) (cit. on pp. 44, 48, 102).

73. Roati, G., Riboli, F., Modugno, G. & Inguscio, M. Fermi-Bose Quantum Degenerate ^{40}K−^{87}Rb Mixture with Attractive Interaction. *Phys. Rev. Lett.* **89,** 150403 (2002) (cit. on p. 44).

74. Roati, G. *et al.* ^{39}K Bose-Einstein Condensate with Tunable Interactions. *Phys. Rev. Lett.* **99,** 010403 (2007) (cit. on p. 44).

75. Loftus, T., Regal, C. A., Ticknor, C., Bohn, J. L. & Jin, D. S. Resonant Control of Elastic Collisions in an Optically Trapped Fermi Gas of Atoms. *Phys. Rev. Lett.* **88,** 173201 (2002) (cit. on pp. 44, 62, 102).

76. Regal, C. A., Ticknor, C., Bohn, J. L. & Jin, D. S. Tuning *p*-Wave Interactions in an Ultracold Fermi Gas of Atoms. *Phys. Rev. Lett.* **90,** 053201 (2003) (cit. on pp. 44, 62).

77. D'Errico, C. *et al.* Feshbach resonances in ultracold 39 K. *New Journal of Physics* **9,** 223 (2007) (cit. on pp. 44, 62, 153, 161).

78. Kishimoto, T., Kobayashi, J., Noda, K., Aikawa, K., Ueda, M. & Inouye, S. Direct evaporative cooling of ^{41}K into a Bose-Einstein condensate. *Phys. Rev. A* **79,** 031602 (2009) (cit. on pp. 44, 48, 102).

79. Wu, C.-H., Santiago, I., Park, J. W., Ahmadi, P. & Zwierlein, M. W. Strongly interacting isotopic Bose-Fermi mixture immersed in a Fermi sea. *Phys. Rev. A* **84,** 011601 (2011) (cit. on pp. 44, 48, 62, 94).

80. Bloch, I., Dalibard, J. & Zwerger, W. Many-body physics with ultracold gases. *Rev. Mod. Phys.* **80,** 885–964 (2008) (cit. on p. 44).

81. Esslinger, T. Fermi-Hubbard Physics with Atoms in an Optical Lattice. *Annual Review of Condensed Matter Physics* **1,** 129–152 (2010) (cit. on p. 44).

82. Chevy, F. & Mora, C. Ultra-cold polarized Fermi gases. *Reports on Progress in Physics* **73,** 112401 (2010) (cit. on p. 44).

83. Chevy, F. Bose Polarons that Strongly Interact. *Physics* **9,** 86 (2016) (cit. on p. 44).

84. Côté, R., Dalgarno, A., Wang, H. & Stwalley, W. C. Potassium scattering lengths and prospects for Bose-Einstein condensation and sympathetic cooling. *Phys. Rev. A* **57,** R4118–R4121 (1998) (cit. on p. 46).

85. Chen, H.-Z. *et al.* Production of large ^{41}K Bose-Einstein condensates using D_1 gray molasses. *Phys. Rev. A* **94,** 033408 (2016) (cit. on pp. 48, 60, 88, 102).

86. Uehlinger, T. *A 2D Magneto-Optical Trap as a High-Flux Source of Cold Potassium Atoms.* MA thesis (ETH, 2008) (cit. on pp. 53, 54).

87. Landini, M. *A tunable Bose-Einstein condensate for quantum interferometry.* PhD thesis (University of Trento, 2011) (cit. on pp. 54, 85).

88. Campbell, R. L. D., Smith, R. P., Tammuz, N., Beattie, S., Moulder, S. & Hadzibabic, Z. Efficient production of large ^{39}K Bose-Einstein condensates. *Phys. Rev. A* **82,** 063611 (2010) (cit. on pp. 54, 85, 102).

89. Schünemann, U., Engler, H., Grimm, R., Weidemüller, M. & M. Zielonkowski. Simple scheme for tunable frequency offset locking of two lasers. *Review of Scientific Instruments* **70,** 242–243 (1999) (cit. on p. 58).

90. Salomon, G., Fouché, L., Wang, P., Aspect, A., Bouyer, P. & Bourdel, T. Gray-molasses cooling of ^{39}K to a high phase-space density. *EPL (Europhysics Letters)* **104,** 63002 (2013) (cit. on pp. 60, 86, 88, 89, 102).

91. Fernandes, D. R., Sievers, F., Kretzschmar, N., Wu, S., Salomon, C. & Chevy, F. Sub-Doppler laser cooling of fermionic ^{40}K atoms in three-dimensional gray optical molasses. *EPL (Europhysics Letters)* **100,** 63001 (2012) (cit. on pp. 60, 88).

92. Sievers, F. *et al.* Simultaneous sub-Doppler laser cooling of fermionic ^{6}Li and ^{40}K on the D_1 line: Theory and experiment. *Phys. Rev. A* **91,** 023426 (2015) (cit. on p. 60).

93. Ludewig, A. *Feshbach Resonances in ^{40}K.* PhD thesis (University of Amsterdam, 2012) (cit. on p. 62).

94. Krauser, J. S. *et al.* Investigation of Feshbach resonances in ultracold ^{40}K spin mixtures. *Phys. Rev. A* **95,** 042701 (2017) (cit. on p. 62).

95. Sabulsky, D. O., Parker, C. V., Gemelke, N. D. & Chin, C. Efficient continuous-duty Bitter-type electromagnets for cold atom experiments. *Review of Scientific Instruments* **84,** 104706 (2013) (cit. on p. 62).

96. DeMarco, B. *Quantum Behavior of an Atomic Fermi Gas.* PhD thesis (University of Colorado (JILA), 2001) (cit. on p. 69).

97. Putra, A. *Magnetized plane wave and stripe-ordered phases in spin-orbit-coupled bose gases.* PhD thesis (NIST and Department of Physics at the University of Maryland, 2018) (cit. on p. 71).

98. Thomas, P. *Optical dipole potentials for multi-component Bose-Einstein condensates.* MA thesis (ICFO/Universität Hamburg-Institut für Laser-Physik, 2017) (cit. on pp. 73, 74, 139).

99. Hueck, K., Luick, N., Sobirey, L., Siegl, J., Lompe, T. & Moritz, H. Two-Dimensional Homogeneous Fermi Gases. *Phys. Rev. Lett.* **120,** 060402 (2018) (cit. on p. 74).

100. Bradley, C. C., Sackett, C. A. & Hulet, R. G. Bose-Einstein Condensation of Lithium: Observation of Limited Condensate Number. *Phys. Rev. Lett.* **78,** 985–989 (1997) (cit. on pp. 75, 173).

101. Gajdacz, M., Pedersen, P. L., Mørch, T., Hilliard, A. J., Arlt, J. & Sherson, J. F. Non-destructive Faraday imaging of dynamically controlled ultracold atoms. *Review of Scientific Instruments* **84,** 083105 (2013) (cit. on p. 75).

102. Saemisch, L. *Development of an imaging system for a quantum gas experiment.* Intership report. 2015 (cit. on p. 75).

103. Sanz, J. *Development of a fluorescence imaging system for a quantum gas experiment.* MA thesis (ICFO, 2015) (cit. on p. 75).

104. Kapitza, P. L. & Dirac, P. A. M. The reflection of electrons from standing light waves. *Mathematical Proceedings of the Cambridge Philosophical Society* **29,** 297–300 (1933) (cit. on p. 76).

105. Ridinger, A. *Towards quantum degenerate Fermi mixtures: Photoassociation of weakly bound $^6Li^{40}K$ molecules.* PhD thesis (Ecole Normale Supérieure de Paris - ENS Paris, 2011) (cit. on pp. 81, 83).

106. Dieckmann, K., Spreeuw, R. J. C., Weidemüller, M. & Walraven, J. T. M. Two-dimensional magneto-optical trap as a source of slow atoms. *Phys. Rev. A* **58,** 3891–3895 (1998) (cit. on p. 83).

107. Park, S. J., Noh, J. & Mun, J. Cold atomic beam from a two-dimensional magneto-optical trap with two-color pushing laser beams. *Optics Communications* **285,** 3950 –3954 (2012) (cit. on p. 83).

108. Cheiney, P. *Matter wave scattering on complex potentials.* PhD thesis (University of Toulouse, 2013) (cit. on p. 83).

109. Cabrera, C. *An isotopic Bose-Fermi mixture experiment for the study of the Bose polaron problem.* Thesis Proposal. 2015 (cit. on p. 85).

110. Landini, M. *et al.* Sub-Doppler laser cooling of potassium atoms. *Phys. Rev. A* **84,** 043432 (2011) (cit. on p. 87).

111. Tarnowski, M. *Implementation and characterization of a gray molasses and of tunable hexagonal optical lattices for ^{40}K.* MA thesis (Universität Hamburg-Institut für Laser-Physik, 2015) (cit. on p. 89).

112. Lin, Y.-J., Perry, A. R., Compton, R. L., Spielman, I. B. & Porto, J. V. Rapid production of ^{87}Rb Bose-Einstein condensates in a combined magnetic and optical potential. *Phys. Rev. A* **79,** 063631 (2009) (cit. on p. 94).

113. Y., X.-C. *et al.* Strongly Interacting Bose Gases near a d-wave Shape Resonance. *arXiv:1711.06622* (2017) (cit. on p. 99).

114. Smith, R. P., Campbell, R. L. D., Tammuz, N. & Hadzibabic, Z. Effects of Interactions on the Critical Temperature of a Trapped Bose Gas. *Phys. Rev. Lett.* **106,** 250403 (2011) (cit. on p. 101).

115. Landini, M. *et al.* Direct evaporative cooling of ^{39}K atoms to Bose-Einstein condensation. *Phys. Rev. A* **86,** 033421 (2012) (cit. on p. 102).

116. Roati, G. *et al.* ^{39}K Bose-Einstein Condensate with Tunable Interactions. *Phys. Rev. Lett.* **99,** 010403 (2007) (cit. on p. 102).

117. Delannoy, G., Murdoch, S. G., Boyer, V., Josse, V., Bouyer, P. & Aspect, A. Understanding the production of dual Bose-Einstein condensation with sympathetic cooling. *Phys. Rev. A* **63,** 051602 (2001) (cit. on p. 105).

118. Wille, E. *et al.* Exploring an Ultracold Fermi-Fermi Mixture: Interspecies Feshbach Resonances and Scattering Properties of ^{6}Li and ^{40}K. *Phys. Rev. Lett.* **100,** 053201 (2008) (cit. on pp. 107, 110, 111).

119. Tiecke, T. G., Goosen, M. R., Walraven, J. T. M. & Kokkelmans, S. J.J.M. F. Asymptotic-bound-state model for Feshbach resonances. *Phys. Rev. A* **82,** 042712 (2010) (cit. on pp. 107, 110, 111).

120. Falke, S., Knöckel, H., Friebe, J., Riedmann, M., Tiemann, E. & Lisdat, C. Potassium ground-state scattering parameters and Born-Oppenheimer potentials from molecular spectroscopy. *Phys. Rev. A* **78,** 012503 (2008) (cit. on pp. 107, 109, 112, 113, 116, 153).

121. Stoof, H. T. C., Koelman, J. M.V. A. & Verhaar, B. J. Spin-exchange and dipole relaxation rates in atomic hydrogen: Rigorous and simplified calculations. *Phys. Rev. B* **38,** 4688–4697 (1988) (cit. on p. 110).

122. Wille, E. *Preparation of an optically trapped Fermi-Fermi mixture of ^{6}Li and ^{40}K atoms and characterization of the interspecies interactions by Feshbach spectroscopy.* PhD thesis (Institut fur Quantenoptik und Quanteninformation Institut fur Experimentalphysik, Innsbruck, 2009) (cit. on p. 111).

123. Tomza, M., González-Férez, R., Koch, C. P. & Moszynski, R. Controlling Magnetic Feshbach Resonances in Polar Open-Shell Molecules with Nonresonant Light. *Phys. Rev. Lett.* **112,** 113201 (2014) (cit. on p. 112).

124. Tomza, M., Koch, C. P. & Moszynski, R. Cold interactions between an Yb^{+} ion and a Li atom: Prospects for sympathetic cooling, radiative association, and Feshbach resonances. *Phys. Rev. A* **91,** 042706 (2015) (cit. on p. 112).

125. Lange, A. D. *et al.* Determination of atomic scattering lengths from measurements of molecular binding energies near Feshbach resonances. *Phys. Rev. A* **79,** 013622 (2009) (cit. on p. 112).

126. Kishimoto, T., Kobayashi, J., Noda, K., Aikawa, K., Ueda, M. & Inouye, S. Direct evaporative cooling of ^{41}K into a Bose-Einstein condensate. *Phys. Rev. A* **79,** 031602 (2009) (cit. on p. 113).

127. D'Errico, C. *et al.* Feshbach resonances in ultracold ^{39}K. *New Journal of Physics* **9,** 223 (2007) (cit. on p. 113).

128. Jørgensen, N. B. *et al.* Observation of Attractive and Repulsive Polarons in a Bose-Einstein Condensate. *Phys. Rev. Lett.* **117,** 055302 (2016) (cit. on p. 113).

129. Thompson, S. T., Hodby, E. & Wieman, C. E. Ultracold Molecule Production via a Resonant Oscillating Magnetic Field. *Phys. Rev. Lett.* **95,** 190404 (2005) (cit. on p. 114).

130. Hanna, T. M., Köhler, T. & Burnett, K. Association of molecules using a resonantly modulated magnetic field. *Phys. Rev. A* **75,** 013606 (2007) (cit. on p. 114).

131. Regal, C. A., Ticknor, C., Bohn, J. L. & Jin, D. S. Creation of ultracold molecules from a Fermi gas of atoms. *Nature* **424,** 47 EP – (2003) (cit. on p. 114).

132. Weber, C. *Controlled few-body interactions in ultracold bosonic mixtures.* PhD thesis (University of Bonn, 2009) (cit. on p. 114).

133. Gammal, A., Frederico, T., Tomio, L. & Chomaz, P. Atomic Bose-Einstein condensation with three-body interactions and collective excitations. *Journal of Physics B Atomic Molecular and Optical Physics* **33,** 4053 (2000) (cit. on p. 120).

134. Bulgac, A. Dilute Quantum Droplets. *Phys. Rev. Lett.* **89,** 050402 (2002) (cit. on pp. 120, 154).

135. Saito, H., Hulet, R. G. & Ueda, M. Stabilization of a Bose-Einstein droplet by hyperfine Rabi oscillations. *Phys. Rev. A* **76,** 053619 (2007) (cit. on p. 120).

136. Cheiney, P., Cabrera, C. R., Sanz, J., Naylor, B., Tanzi, L. & Tarruell, L. Bright Soliton to Quantum Droplet Transition in a Mixture of Bose-Einstein Condensates. *Phys. Rev. Lett.* **120,** 135301 (2018) (cit. on pp. 120, 157).

137. Kadau, H. *et al.* Observing the Rosensweig instability of a quantum ferrofluid. *Nature* **530,** 194 EP – (2016) (cit. on pp. 120, 132, 133, 167, 171).

138. Ferrier-Barbut, I., Kadau, H., Schmitt, M., Wenzel, M. & Pfau, T. Observation of Quantum Droplets in a Strongly Dipolar Bose Gas (cit. on pp. 120, 132, 133).

139. Chomaz, L. *et al.* Quantum-Fluctuation-Driven Crossover from a Dilute Bose-Einstein Condensate to a Macrodroplet in a Dipolar Quantum Fluid. *Physical Review X* **6,** 041039 (2016) (cit. on pp. 120, 132, 153, 158, 165, 172, 175).

140. Ferrier-Barbut, I., Schmitt, M., Wenzel, M., Kadau, H. & Pfau, T. Liquid quantum droplets of ultracold magnetic atoms. *Journal of Physics B: Atomic, Molecular and Optical Physics* **49,** 214004 (2016) (cit. on pp. 120, 133, 188).

141. Schmitt, M., Wenzel, M., Böttcher, F., Ferrier-Barbut, I. & Pfau, T. Self-bound droplets of a dilute magnetic quantum liquid. *Nature* **539,** 259–262 (2016) (cit. on pp. 120, 129, 130, 132, 133, 153, 158, 165).

142. Wenzel, M., Böttcher, F., Langen, T., Ferrier-Barbut, I. & Pfau, T. Striped states in a many-body system of tilted dipoles. *Phys. Rev. A* **96,** 053630 (2017) (cit. on p. 120).

143. Wächtler, F. & Santos, L. Ground-state properties and elementary excitations of quantum droplets in dipolar Bose-Einstein condensates. *Phys. Rev. A* **94,** 043618 (2016) (cit. on pp. 120, 158).

144. Baillie, D., Wilson, R. M., Bisset, R. N. & Blakie, P. B. Self-bound dipolar droplet: A localized matter wave in free space. *Phys. Rev. A* **94,** 021602 (2016) (cit. on pp. 120, 153).

145. Ferrier-Barbut, I. & Pfau, T. Quantum liquids get thin. *Science* **359,** 274–275 (2018) (cit. on p. 121).

146. Cikojević, V., Dželalija, K., Stipanović, P., Markić, L. V. & Boronat, J. Ultradilute quantum liquid drops. *Phys. Rev. B* **97,** 140502 (2018) (cit. on pp. 122, 154).

147. Volovik, G. E. *The Universe in a Helium Droplet* (Oxford Science Publications, 2009) (cit. on pp. 123, 188).

148. Singh, K. G. & Rokhsar, D. S. Collective Excitations of a Confined Bose Condensate. *Phys. Rev. Lett.* **77,** 1667–1670 (1996) (cit. on p. 124).

149. Bisset, R. N., Wilson, R. M., Baillie, D & Blakie, P. B. Ground-state phase diagram of a dipolar condensate with quantum fluctuations (cit. on pp. 129, 158, 165, 167, 180).

150. Wächtler, F. & Santos, L. Quantum filaments in dipolar Bose-Einstein condensates. *Phys. Rev. A* **93,** 061603 (2016) (cit. on pp. 129, 180).

151. Kadau, H. *Rosensweig Instability and Droplets in a Quantum Ferrofluid of Dysprosium Atoms.* PhD thesis (University of Stuttgart, 2016) (cit. on p. 132).

152. Baillie, D., Wilson, R. M. & Blakie, P. B. Collective Excitations of Self-Bound Droplets of a Dipolar Quantum Fluid. *Phys. Rev. Lett.* **119,** 255302 (2017) (cit. on p. 132).

153. Ferrier-Barbut, I. *et al.* Scissors Mode of Dipolar Quantum Droplets of Dysprosium Atoms. *Phys. Rev. Lett.* **120,** 160402 (2018) (cit. on p. 133).

154. Schulze, T. A. *et al.* Feshbach spectroscopy and dual-species Bose-Einstein condensation of ^{23}Na$-^{39}$K mixtures. *Phys. Rev. A* **97,** 023623 (2018) (cit. on p. 133).

155. Thalhammer, G *et al.* Collisional and molecular spectroscopy in an ultracold Bose–Bose mixture. *New Journal of Physics* **11,** 055044 (2009) (cit. on p. 133).

156. Barontini, G. *et al.* Observation of Heteronuclear Atomic Efimov Resonances. *Phys. Rev. Lett.* **103,** 043201 (2009) (cit. on p. 133).

157. Wächtler, F. & Santos, L. Ground-state properties and elementary excitations of quantum droplets in dipolar Bose-Einstein condensates. *Phys. Rev. A* **94,** 043618 (2016) (cit. on p. 135).

158. Schmitt, M. *A Self-bound Dilute Quantum Liquid of Dysprosium Atoms.* PhD thesis (University of Stuttgart, 2017) (cit. on p. 135).

159. Strecker, K. E., Partridge, G. B., Truscott, A. G. & Hulet, R. G. Bright matter wave solitons in Bose–Einstein condensates. *New Journal of Physics* **5,** 73 (2003) (cit. on p. 135).

160. Salasnich, L. Dynamics of a Bose-Einstein-condensate bright soliton in an expulsive potential. *Phys. Rev. A* **70,** 053617 (2004) (cit. on p. 136).

161. Ville, J. L. *et al.* Loading and compression of a single two-dimensional Bose gas in an optical accordion. *Phys. Rev. A* **95,** 013632 (2017) (cit. on p. 139).

162. Bradley, C. C., Sackett, C. A. & Hulet, R. G. Analysis of in situ images of Bose-Einstein condensates of lithium. *Phys. Rev. A* **55,** 3951–3953 (1997) (cit. on p. 140).

163. Weber, T., Herbig, J., Mark, M., Nägerl, H.-C. & Grimm, R. Three-Body Recombination at Large Scattering Lengths in an Ultracold Atomic Gas. *Phys. Rev. Lett.* **91,** 123201 (2003) (cit. on p. 147).

164. Zaccanti, M *et al.* Observation of an Efimov spectrum in an atomic system. *Nature Physics* **5** (2009) (cit. on p. 148).

165. Ferlaino, F. & Grimm, R. Forty years of Efimov physics: How a bizarre prediction turned into a hot topic. *Physics* **3** (2010) (cit. on p. 148).

166. Braaten, E. & H.-W.Hammer. Efimov Physics in Cold Atoms. *Annals of Physics* **322,** 120 –163 (2007) (cit. on p. 148).

167. Roy, S. *et al.* Test of the Universality of the Three-Body Efimov Parameter at Narrow Feshbach Resonances. *Phys. Rev. Lett.* **111,** 053202 (2013) (cit. on pp. 153, 161, 168).

168. Ziń, P., Pylak, M., Wasak, T., Gajda, M. & Idziaszek, Z. Quantum Bose-Bose droplets at a dimensional crossover. *arXiv:1805.11186* (2018) (cit. on pp. 154, 186).

169. Ilg, T., Kumlin, J., Santos, L., Petrov, D. & Büchler, H. Dimensional crossover for the beyond-mean-field correction in Bose gases. *arXiv:1806.01784* (2018) (cit. on pp. 154, 186).

170. Salasnich, L., Parola, A. & Reatto, L. Condensate bright solitons under transverse confinement. *Phys. Rev. A* **66,** 043603 (2002) (cit. on p. 158).

171. Antoine, X. & Duboscq, R. GPELab, a Matlab Toolbox to solve Gross-Pitaevskii Equations I: computation of stationary solutions. **185,** 2969–2991 (Nov. 2014) (cit. on p. 161).

172. Ferrier-Barbut, I., Wenzel, M., Schmitt, M., Böttcher, F. & Pfau, T. Onset of a modulational instability in trapped dipolar Bose-Einstein condensates. *Phys. Rev. A* **97,** 011604 (2018) (cit. on pp. 165, 180).

173. Petrov, D. S. & Astrakharchik, G. E. Ultradilute Low-Dimensional Liquids. *Phys. Rev. Lett.* **117,** 100401 (2016) (cit. on p. 171).

174. Burt, E. A., Ghrist, R. W., Myatt, C. J., Holland, M. J., Cornell, E. A. & Wieman, C. E. Coherence, Correlations, and Collisions: What One Learns about Bose-Einstein Condensates from Their Decay. *Phys. Rev. Lett.* **79,** 337–340 (1997) (cit. on p. 175).

175. Y. Kagan, B. V. S. & Shlyapnikov, G. V. Effect of Bose condensation on inelastic processes in gases. *JETP Lett.* **42,** 209 (1985) (cit. on p. 175).

176. Petrov, D. S. & Astrakharchik, G. E. Ultradilute Low-Dimensional Liquids. *Phys. Rev. Lett.* **117,** 100401 (2016) (cit. on p. 185).

177. Cappellaro, A., Macrì, T., Bertacco, G. F. & Salasnich, L. Equation of state and self-bound droplet in Rabi-coupled Bose mixtures. *Scientific Reports* **7,** 13358 (2017) (cit. on p. 186).

178. Balents, L., Fisher, M. P. A. & Girvin, S. M. Fractionalization in an easy-axis Kagome antiferromagnet. *Phys. Rev. B* **65,** 224412 (2002) (cit. on p. 186).

179. Tolra, B. L., O'Hara, K. M., Huckans, J. H., Phillips, W. D., Rolston, S. L. & Porto, J. V. Observation of Reduced Three-Body Recombination in a Correlated 1D Degenerate Bose Gas. *Phys. Rev. Lett.* **92,** 190401 (2004) (cit. on p. 186).

180. Büchler, H. P., Micheli, A. & Zoller, P. Three-body interactions with cold polar molecules. *Nature Physics* **3.** Article, 726 (2007) (cit. on p. 186).

181. Wenzel, M., Pfau, T. & Ferrier-Barbut., I. A fermionic impurity in a dipolar quantum droplet. *arXiv:1807.00631* (2018) (cit. on p. 187).

182. Lemeshko, M. Quasiparticle Approach to Molecules Interacting with Quantum Solvents. *Phys. Rev. Lett.* **118,** 095301 (2017) (cit. on p. 187).

183. Karpiuk, T., Brewczyk, M., Ospelkaus-Schwarzer, S., Bongs, K., Gajda, M. Soliton Trains in Bose-Fermi Mixtures. *Phys. Rev. Lett.* **93,** 100401 (2004) (cit. on p. 187).

184. Rakshit, D., Karpiuk, T., Brewczyk, M. & Gajda, M. Quantum Bose-Fermi droplets. *arXiv:1801.00346* (2017) (cit. on p. 187).

185. Rakshit, D., Karpiuk, T., Brewczyk, M., M., L. & Gajda, M. Self-bound Bose-Fermi liquids in lower dimensions. *arXiv:1808.04793* (2018) (cit. on p. 187).

186. Nguyen, J. H. V., Dyke, P., Luo, D., Malomed, B. A. & Hulet, R. G. Collisions of matter-wave solitons. *Nature Physics* **10,** 918 (2014) (cit. on p. 188).

187. Adhikari, S. K. Statics and dynamics of a self-bound matter-wave quantum ball. *Phys. Rev. A* **95,** 023606 (2017) (cit. on p. 188).

188. Boudjemâa, A. Quantum dilute droplets of dipolar bosons at finite temperature. *Annals of Physics* **381,** 68 –79 (2017) (cit. on p. 188).

DECLARATION

I declare that this thesis has been composed solely by myself and that it has not been submitted, in whole or in part, in any previous application for a degree. I confirm that appropriate credit has been given within this thesis where reference has been made to the work of others.

Barcelona, Spain, July 2018

Cesar Raymundo Cabrera Córdova